High Resolution Circulation of the Hawkesbury Shelf Region, SE Australia: Mean, Variability and Transport Pathways

by

Nina Ribbat

A thesis submitted for the degree of Doctor of Philosophy

at

The University of New South Wales
Australia

March 2020

PLEASE TYPE

THE UNIVERSITY OF NEW SOUTH WALES

Thesis/Dissertation Sheet

Surname or Family name: **Ribbat**

First name: **Nina** Other name/s:

Abbreviation for degree as given in the University calendar: **PhD**

School: **Mathematics and Statistics** Faculty: **Science**

Title: **High-Resolution Circulation of the Hawkesbury Shelf Region, SE Australia: Mean, Variability and Transport Pathways**

Abstract 350 words maximum: (PLEASE TYPE)

The exchange between the open ocean and coastal waters within continental shelf systems is driven by complex circulation processes making it hard to measure and observe. They are highly productive regions, sustaining marine ecosystems and are often nursery areas for many organisms, providing the basis for a variety of natural resources of high economic importance. Along southeastern Australia, the shelf circulation has been studied through in situ temperature and velocity observations, coarse resolution satellite data and modelling studies. However, due to the lack of high spatial resolution data over continued time periods, the circulation over the shelf as a system has not yet been explored.

The general aims of this thesis are to assess the mean and time varying circulation over the Hawkesbury Shelf (HS, 31.5-34.5ºS) to understand the influence of the EAC on the shelf circulation variability; and to identify water sources of an offshore artificial reef off Sydney. Towards these aims, a high-resolution version of the Regional Ocean Modelling System (ROMS) is configured to model the circulation on the HS for 2012 and 2013. Robust model validation against high-resolution observations shows that the model achieves a reliable representation of the circulation on the shelf. Mean along and across-shelf transports are quantified to identify major regions of ocean/shelf exchange and its spatial and temporal variability. Throughout the year, maximum shelf-water export is associated with the eastward separation of the EAC jet between 31 and 32.5ºS. Downstream of the EAC separation, transports become more variable and weaker in magnitude. While the EAC separation creates distinct circulation regimes outside the 200 m isobath, the inner shelf remains unaffected by the EAC variability as indicated by high correlations of along-shelf transports along the coast.

Finally, the model is used to understand the movement of water over the inner shelf, with particular focus on the source of water arriving at an offshore artificial reef (OAR) off Sydney. Using Lagrangian particle tracking, the source of water reaching the continental shelf is identified to discern regions that are more likely to be productive. Backward water parcel trajectories reveal that deep offshore waters come mainly from middle shelf regions between 33 and 33.5ºS and also from the south, downstream of the typical EAC separation latitudes. In contrast, waters found in inner shelf regions come from the north by poleward flowing inshore waters.

The results suggest that seasonal variability in source water location is low; however, the region where the source waters come from is narrow in summer and broader in autumn and winter. Results presented in this thesis aid in understanding the influence of mesoscale variability on the coastal circulation and transport of waters to the inner shelf.

FOR OFFICE USE ONLY Date of completion of requirements for Award:

ORIGINALITY STATEMENT

‘I hereby declare that this submission is my own work and to the best of my knowledge it contains no materials previously published or written by another person, or substantial proportions of material which have been accepted for the award of any other degree or diploma at UNSW or any other educational institution, except where due acknowledgement is made in the thesis. Any contribution made to the research by others, with whom I have worked at UNSW or elsewhere, is explicitly acknowledged in the thesis. I also declare that the intellectual content of this thesis is the product of my own work, except to the extent that assistance from others in the project’s design and conception or in style, presentation and linguistic expression is acknowledged.’

Signed . . . . . ……..

Date . . . . . .13/02/2020 . . . . . …….

COPYRIGHT STATEMENT

Signed …….....

Date……13/02/2020…….....

AUTHENTICITY STATEMENT

‘I certify that the Library deposit digital copy is a direct equivalent of the final officially approved version of my thesis.’

Signed …….....

Date……13/02/2020…….....

INCLUSION OF PUBLICATION STATEMENT

UNSW is supportive of candidates publishing their research results during their candidature as detailed in the UNSW Thesis Examination Procedure.

Publications can be used in their thesis in lieu of a Chapter if:

- The candidate contributed greater than 50% of the content in the publication and is the "primary author", ie. the candidate was responsible primarily for the planning, execution and preparation of the work for publication
- The candidate has approval to include the publication in their thesis in lieu of a Chapter from their supervisor and Postgraduate Coordinator.
- The publication is not subject to any obligations or contractual agreements with a third party that would constrain its inclusion in the thesis

Please indicate whether this thesis contains published material or not:

☒ This thesis contains no publications, either published or submitted for publication
(if this box is checked, you may delete all the material on page 2)

☒ Some of the work described in this thesis has been published and it has been documented in the relevant Chapters with acknowledgement
(if this box is checked, you may delete all the material on page 2)

☒ This thesis has publications (either published or submitted for publication) incorporated into it in lieu of a chapter and the details are presented below

CANDIDATE'S DECLARATION

I declare that:

- I have complied with the UNSW Thesis Examination Procedure
- where I have used a publication in lieu of a Chapter, the listed publication(s) below meet(s) the requirements to be included in the thesis.

Candidate's Name	**Signature**	**Date (dd/mm/yy)**
Nina Ribbat		**13/02/2020**

Abstract

The exchange between the open ocean and coastal waters within continental shelf systems is driven by complex circulation processes making it hard to measure and observe. They are highly productive regions, sustaining marine ecosystems and are often nursery areas for many organisms, providing the basis for a variety of natural resources of high economic importance. Along southeastern Australia, the shelf circulation has been studied through in situ temperature and velocity observations, coarse resolution satellite data and modelling studies. However, due to the lack of high spatial resolution data over continued time periods, the circulation over the shelf as a system has not yet been explored.

The general aims of this thesis are to assess the mean and time varying circulation over the Hawkesbury Shelf (HS, 31.5-34.5^{o}S) to understand the influence of the EAC on the shelf circulation variability; and to identify water sources of an offshore artificial reef off Sydney. Towards these aims, a high-resolution version of the Regional Ocean Modelling System (ROMS) is configured to model the circulation on the HS for 2012 and 2013. Robust model validation against high-resolution observations shows that the model achieves a reliable representation of the circulation on the shelf.

Mean along and across-shelf transports are quantified to identify major regions of ocean/shelf exchange and its spatial and temporal variability. Throughout the year, maximum shelf-water export is associated with the eastward separation of the EAC jet between 31 and 32.5^{o}S. Downstream of the EAC separation, transports become more variable and weaker in magnitude. While the EAC separation creates distinct circulation regimes outside the 200 m isobath, the inner shelf remains unaffected by the EAC variability as indicated by high correlations of along-shelf transports along the coast.

Finally, the model is used to understand the movement of water over the inner shelf, with particular focus on the source of water arriving at an offshore artificial reef

(OAR) off Sydney. Using Lagrangian particle tracking, the source of water reaching the continental shelf is identified to discern regions that are more likely to be productive. Backward water parcel trajectories reveal that deep offshore waters come mainly from middle shelf regions between 33 and 33.5^{o}S and also from the south, downstream of the typical EAC separation latitudes. In contrast, waters found in inner shelf regions come from the north by poleward flowing inshore waters.

The results suggest that seasonal variability in source water location is low; however, the region where the source waters come from is narrow in summer and broader in autumn and winter. Results presented in this thesis aid in understanding the influence of mesoscale variability on the coastal circulation and transport of waters to the inner shelf.

"Dedicated to my loving parents, Frank and Sonja Ribbat and my wonderful grandmother, Ruth. Thank you for your endless support and guidance through the challenges of school and life. I am the luckiest daughter."

Acknowledgements

First and foremost, I want to express my gratitude to my supervisors, Moninya Roughan, Iain Suthers and Brian Powell for giving me the opportunity to do research and providing invaluable guidance and support throughout this thesis. I learned a lot from their expertise and our meetings. I am extending my gratitude to Colette Kerry, for the help and assistance during the model development.

My heartfelt thanks go out to Paulina Cetina-Heredia, for all the knowledge she shared with me. Her contagious enthusiasm for science and eye for detail inspired me. Her advice on both research and life has been invaluable. It was a great privilege to have learned from her and becoming close friends along the way.

I am also deeply grateful to Shivanesh Rao, for the guidance, support and encouragement through the jungle of ocean modelling. I am appreciative of the time, patience and effort spent in teaching me. I enjoyed our many discussions and laughs.

Special thanks to Amandine Schaeffer for the continuous help and invaluable input on many topics throughout this thesis.

I also want to thank Matthew Archer, who always had an open door to discuss any research questions. In addition, I want to thank the whole oceanography team from the UNSW Coastal and Regional Oceanography Group for sharing this experience with me: Tim Austin (for your expertise and patience during the endless hours spent on the little Rampage. I was convinced I never got sea sick, until I met the Rampage), Julie Wood, Carlos Rocha, Eduardo Vitelli and Stuart Milburn.

Lastly, I would like to thank my close friends, Corinna Thamm, Aidan Broadbent, David Roberts, Brian Shimamura and Geralyn St. Joseph for their unconditional support and encouragement and for making my life an adventure.

I also thank the Australian Research Council Linkage Project LP120100592, and the NSW Department of Primary Industries (Fisheries) for the financial support.

Contents

List of Figures

List of Tables

Chapter 1

Introduction

1.1 Circulation on the Continental Shelf

Defined as gently sloping extensions of the continents ending approximately 200 m below present sea level, continental shelves are productive transition zones between the open ocean and the coast. Their shallow nature enables faster recycling of nutrients from the bottom rich layer to the euphotic zone enhancing primary productivity throughout the shelf areas. Furthermore, large abundances of marine life offer considerable economic resources including commercial and recreational fisheries as well as tourism. On the down side, their proximity to the coast makes them vulnerable to anthropogenic influences such as waste disposal, terrestrial runoff and shipping traffic.

The circulation on continental shelves results from interactions between the adjacent mesoscale circulation with regional processes including tides, freshwater discharge, coastal trapped waves and baroclinic / barotropic pressure gradients as well as atmospheric processes (Huyer, 1990). Due to their shallow nature, continental shelves are sensitive to seasonal heating and cooling, the establishment of density fronts, gravity currents, canyon upwelling and downwelling. Given that regional, mesoscale and atmospheric processes often occur at varying time and space scales, resulting dynamics on the shelf are often found to be highly complex.

Various physical and biogeochemical processes are responsible for the distribution and transport of nutrients on the shelf, with cross-shelf transport being one of the most important process impacting the biological productivity. By influencing the delivery and removal of nutrients, pollutants, heat and freshwater to and from the coastal ocean, cross-shelf transport plays a key role in the distribution of ocean properties on the shelf (Brink, 2016).

Cross-shelf exchanges with the open ocean are often the result of eddy encroachments onto the shelf or current intrusion, transporting deep water across the shelf break and into the euphotic zone, enhancing the primary productivity on the shelf (Carter and D'Aubrey, 1988; Oke and Middleton, 2000; Roughan and Middleton, 2002, 2004).

The level of interactions between the open ocean and the shelf however, varies considerably with topography and bottom bathymetry on the shelf. Steep bathymetric gradients can insulate coastal waters from the influence of offshore features such as currents and eddies, greatly altering flow patterns particularly in the nearshore regions (Tally, 2002). Hence, the width of the shelf is another important dimension that adds to the shelf's complexity. This is particularly true for regions adjacent to dynamic western boundary currents (WBC) such as the east coast of Australia, where, the continental shelf is relatively narrow, with an average width of ~20 km, compared to the Gulf Stream, where the shelf is ~ 70-130 km. As a consequence, the shelf width is narrow enough to allow the meandering of the currents along with its eddies to impact on the shelf's circulation (Roughan et al., 2004; Wood et al., 2016) more than the Gulf Stream can along the US eastern shelf.

Despite the high productivity and high economic value of shelf systems, it is to date not fully understood how they function, how they interact with the open ocean, and what mechanisms drive their biological productivity. Thus, the motivation of this thesis is to obtain a comprehensive picture of the time varying circulation on the continental shelf off southeast Australia using outputs from a high-resolution numerical model configured for this region. A reason for this limited knowledge of the circulation off southeast Australia is the paucity of field data and lack of resolution in previous modelling studies. And with the EAC being such a dominant natural feature of the Australian coastal environment, there are broad benefits in understanding its influence on the shelf and coastal region. For example, shipping, fisheries, recreational boating will greatly benefit from a deeper knowledge of the influence of the EAC on the coastal and shelf currents.

1.2 Study Area

The study area, stretches from 31.5^{o}S in the north to 34.5^{o}S in the south along the coast of southeast Australia, adjacent to the East Australian Current (EAC) and encompassing the EAC separation zone. This area includes the productive Hawkesbury

Bioregion from Stockton (32.5ºS) near Newcastle in the north to Shellharbour (34.35ºS) near Wollongong in the south (Fig. 1.1).

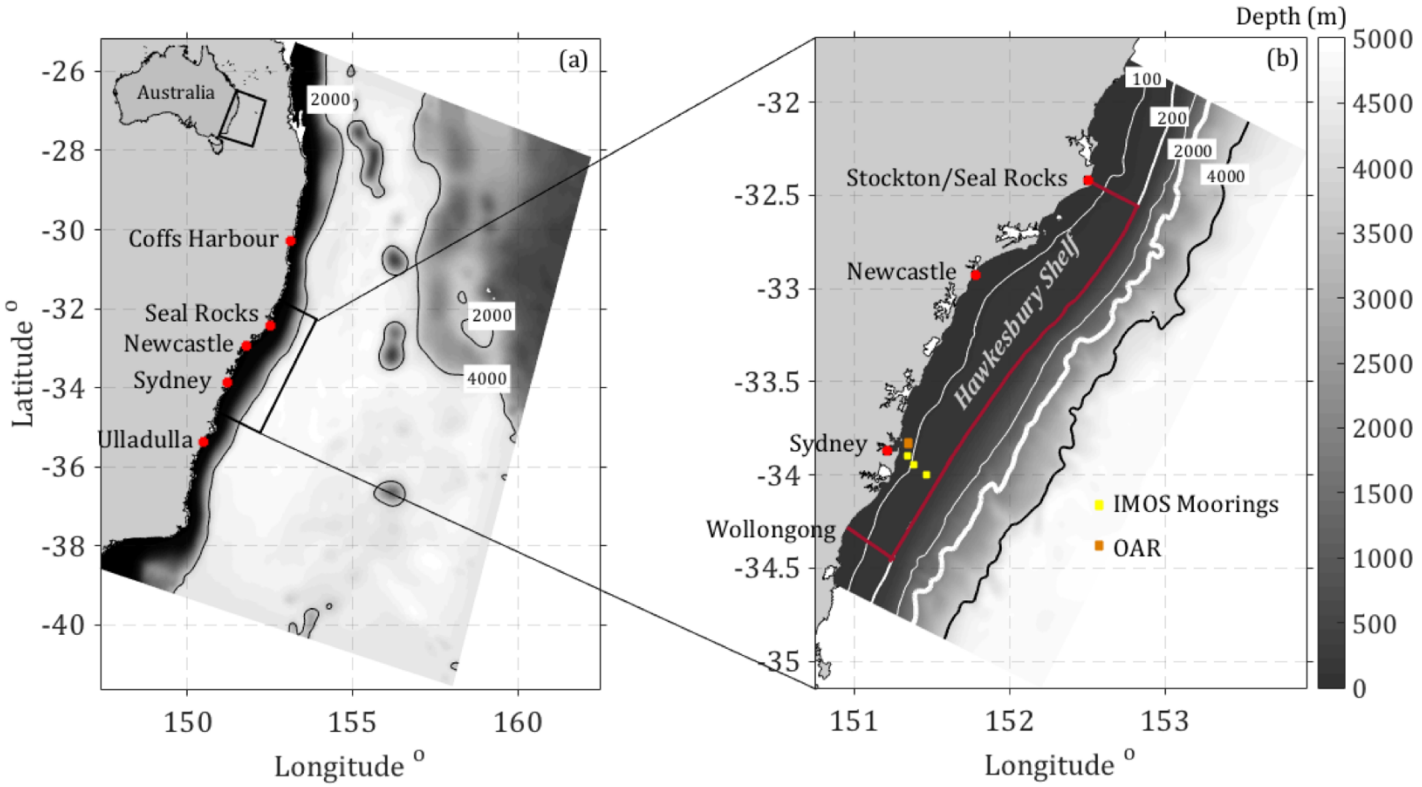

Fig. 1.1. Bathymetry (m) of the study region along the east coast of Australia (a) and a zoomed view of the SE continental shelf, including the Hawkesbury Shelf (b). Solid lines indicate the 100, 200, 2000 and 4000 m isobath. Yellow squares indicate the location of the IMOS moorings used for model validation in the following chapters. Orange square shows the location of Sydney's offshore, artificial reef (OAR).

1.2.1 Continental shelf of SE Australia

1.2.1.1 East Australian Current

The circulation along southeast Australia is largely shaped through interactions with the adjacent mesoscale circulation, dominated by the EAC, the WBC of the south-pacific subtropical gyre (Godfrey et al., 1980; Ridgway and Godfrey, 1997). The pathway of the EAC starts in the South Coral Sea (15°-24°S), continues along the coast of southeast Queensland and Northern NSW (22-35°S), followed by its separation from the coast to form the Tasman front (Fig. 1.2) (Ridgway and Dunn, 2003). The EAC has an overall weaker flow compared to other WBC, such as the Gulf Stream or Agulhas Current, however, its dynamic and eddying nature makes the EAC similar in magnitude (Wilkin and Zhang, 2007). When the EAC encroaches on the continental shelf (Schaeffer et al., 2013, 2014; Wood et al., 2016), it replenishes displaced water masses with warmer oligotrophic water (Roughan and Middleton, 2002, 2004). Nutrient rich coastal waters are then transported east into offshore waters, where the EAC possibly advects high nutrient concentrations downstream along the coast (Roughan and Middleton, 2002).

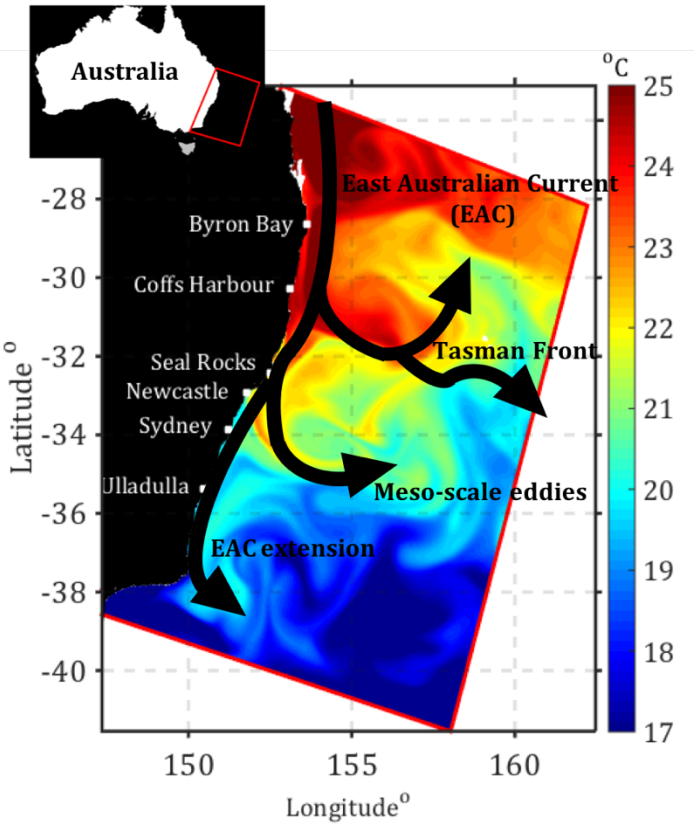

Fig. 1.2. The EAC current system on the east coast of Australia. Its main circulation features are presented as black arrows. The colour shading represents a sea surface temperature snapshot for the 9.1.2013.

1.2.1.2 East Australian Current Separation Zone

The region where the EAC ventures east into the Tasman Sea, typically between 30.7-32.4ºS is defined as the EAC's separation zone. Cetina-Heredia et al. (2014) found that even though 50% of the time the separation occurs within that range, it can extend as far north as 28ºS and south as 38ºS. Throughout this dynamic zone, the mesoscale variability is large, and the coherent current has transitioned into a series of cyclonic and anti-cyclonic eddies (Bowen et al., 2005; Mata et al., 2006; Suthers et al., 2011), shed approximately every 90-110 days (Gibbs et al., 2000; Mata et al., 2006). Consequently, the separation from the coast divides the southeast coast of Australia into 2 distinct dynamical regions (up and downstream) of the EAC separation zone.

Significant progress has been made in understanding the circulation upstream (off Coffs Harbour 30ºS) and downstream (off Sydney 34ºS) (Schaeffer et al., 2013; 2014 a,b). The deployment of the Integrated Marine Observation System (IMOS), infrastructure including moorings, radar and gliders and application of coarser modelling

efforts (Oke et al., 2009; Kerry et al., 2016) have shown that the predominantly shelf circulation and temperature fields are least variable upstream of the separation zone, where the EAC is most coherent and intrudes farthest onto the shelf. Downstream of the separation zone, the flow is more influenced by the EAC's separation.

Once the EAC has detached from the coast, the current loses strength and only 1/3 of the poleward transport continues along the coast (Ridgway and Godfrey, 1997) from ~22 Sv upstream of the separation to ~7 Sv downstream (Kerry et al., 2016). Additionally, the separation from the coast results in intense bottom stress on the shelf, creating upwelling favourable conditions by driving cold, nutrient rich water into the shallow euphotic zone (bottom Ekman transport) (Roughan and Middleton, 2002; Oke and Middleton, 2001; Schaeffer et al., 2014). In fact, the narrowing of the continental shelf (<20 km in width) in the separation zone can lead to intense current encroachments and strong bottom boundary stress across the shelf (Gibbs et al., 1998; Roughan et al., 2004). Thus, the EAC separation zone is a highly dynamic and biologically productive region.

1.3 Numerical Modeling of Continental Shelves

1.3.1 Background on Shelf Modelling

Numerical modelling has become a fundamental tool to not only understand the past environmental state of the ocean, but also to assess its future state and increase our ability to comprehend complex interactions between the open and coastal ocean. However, open and coastal ocean processes are very distinct and controlled by various spatial-temporal scales. Ranging from ocean circulation at the global scale up to several thousand kilometers, which is the width of gyres that extend across each ocean basin, down to about 100 km, which represents the width of strong ocean currents like the East Australian Current, and to dissipation and mixing at the centimeter scale (Talley, 2002). Thus, it is impossible to simulate this wide range of processes using one model due to computational and financial limitations (Sheng et al., 2005).

As a result, most ocean models operate rather on a process-oriented basis, resolving only specific spatio-temporal scales (Fringer et al., 2006). In recent years, techniques have been developed to configure model systems capable of resolving ocean

processes ranging from small to mesoscale (Sheng et al., 2005; Cailleau et al., 2008). The process of downscaling (or nesting) a finer-resolution, limited area model into a larger-scale model allows the investigation of smaller-scale circulation features, previously unresolved in mesoscale models (*e.g.* across-shelf variability, upwelling events and fronts). For this purpose, a nested grid model using the Regional Ocean Modelling System (ROMS) model was chosen to address the aims and objectives of this thesis.

Downscaling does not come without shortcomings (Mason et al., 2010; Auclair et al., 2006). Small-scale processes can occur throughout the nested domain, which are unable to propagate out of the domain if the model is only way-way nested and generate false flow or temperature patterns (Barth et al., 2008). One-way nesting means the parent grid can interact with the child grid through the open boundaries, but not vice versa. Moreover, most nested models rely on their parent grid to supply forcing along the open boundaries, which can lead to incoherencies in the lateral and vertical direction throughout the interpolation process (Auclair et al., 2000; Bricheno et al., 2013).

1.3.2 The Regional Ocean Modelling System (ROMS)

The Regional Ocean Modelling System (ROMS) is a free-surface, hydrostatic, primitive equation ocean model (Haidvogel et al., 2000). ROMS vertical coordinate is called the s-coordinate, which is terrain following (allowing a natural representation of the bottom boundary). S-coordinate systems are an attractive tool for coastal models since they provide vertical stretching, allowing the resolution near the surface and /or the bottom to be enhanced (Song and Haidvogel, 1994).

ROMS has been applied to a variety of situations that indicate its usefulness in the present study. For example, Chen and He (2015) undertook a modelling study to investigate the mean coastal circulation, its variability and exchange processes across the Middle Atlantic Bight and Gulf of Maine using a high-resolution version of ROMS. Initial and boundary conditions were provided by a larger-scale data assimilative ocean model. Good agreements with observations showcase the model's skill to adequately simulate the mean state, variability and cross-shelf dynamics on the shelf. Marta-Almeida et al. (2013), highlighted the benefit of nesting in increasing the overall model performance in capturing near coastal dynamics on the Texas-Louisiana continental shelf.

Along the coast of southeast Australia, process – oriented modelling studies have been undertaken to investigate the EAC separation (Marchessiello and Middleton, 2000), coastal upwelling (Oke et al., 2002; Roughan et al., 2003), eddy dynamics, eddy over washing (Macdonalds et al., 2013), and mesoscale circulation variability (Oke et al., 2003). The latest modelling effort was conducted by Kerry et al. (2016) using a data assimilating model to resolve the eddying circulation and variability along the southeast coast of Australia. Even though the listed implementations have indeed proved valuable for investigating specific and fundamental aspects of the local circulation, fundamental knowledge of a variety of important shelf process (*e.g.* cross-shelf exchanges with the open ocean), is to this date sparse.

1.4 Enhancing Productivity on the Shelf and in the Coastal Ocean: Purpose built Offshore Artificial Reefs (OARs)

Along with the growing populations living by the coast, comes an increase in anthropogenic influences. Understanding the oceanographic regimes influencing the coastal and shelf region is thus becoming increasingly important. The anthropogenic impacts are felt worldwide, for example, the environmental problems (overfishing, pollution by contaminants and oil) in the North and Baltic Sea regions put the local available fish stocks under immense pressure (Robinson and Brink, 2005). In an attempt to counteract this degrading trend, artificial reefs have been deployed around the world to protect marine habitats and enhance fishing abundance.

Historically, artificial reefs were created from scuttled ships, tires, concrete rock or other marine debris (Baine, 2001). For example, in Japan, the use of artificial reefs to enhance the local stock is a common practice that can be traced back to the 17th century (Weisburd, 1986).

In Australia however, artificial reefs are mainly constructed from materials including waste concrete pipes, tires and decommissioned vessels with approximately 40,000 un-ballasted tires deployed as artificial reefs (Branden et al., 1994). Recently there has been an emphasis on designing reefs as fish habitat as part of an integrated approach to fishery enhancement (Becker et al., 2017). They are deployed in both estuarine (Folpp

et al., 2013), and offshore marine environments (20-50 m) to mainly enhance recreational fishing opportunities (Becker et al., 2017).

Purpose built artificial reefs differ often to materials of opportunity by deliberately increasing the surface area covered by the reef and adding of spaces throughout the water column (Smith et al., 2016) to provide shelter for the attachment of primary and secondary producers (Seaman and Jensen, 2000), ultimately, enhancing marine systems. In 2011, the first specifically designed purpose built offshore artificial reef (OAR) was deployed off the coast of Sydney, NSW, Australia. Recent studies found that the Sydney OAR has a 6-fold greater biomass of fish than a natural reef (Smith et al., 2016). The reef provides enough habitat and refuge to safely support around 130 kg of Mado (a small schooling species of fish found on coastal reefs) that fuels fish production by feeding on zooplankton supply (Champion et al., 2015). This indicates the great potential of offshore artificial reefs to enhance local fish production.

The success of an artificial reef is largely dependent on the specific objectives of the particular reef program (*e.g*. fishery enhancement, conservation or habitat restoration). However, the general aim of artificial reefs is to create habitats that support and enhance productivity. The abundance of zooplankton, which represent the link between primary producers and higher trophic levels is a major link in the productivity of artificial reefs (Bianchi et al. 2003, Hwang et al,.2006; Tseng et al., 2008). Benthic invertebrates such as bivalves, crustaceans, tunicates and especially planktivorous fish, use reefs as a refuge and feed on the surrounding zooplankton (Alldredge and King, 2009; Champion et al., 2015), depleting water of plankton (Champion et al., 2015, Motro at al., 2005, Glynn, 1973). Given that artificial reefs are often deployed in the vicinity of natural reefs (Parsons et al., 2016), water reaching the artificial reef is at risk of already being depleted of zooplankton before arrival, which in turn could diminish its productivity.

Therefore, identifying potential sources of zooplankton is fundamental for the successful placement of artificial reefs. More than 12 offshore artificial reefs have been deployed offshore in Australian coastal waters, however, their deployment locations are usually determined by regulations, logistics and expected usage. Understanding spatial factors that influence reef production, such as the location of the water reaching these structures, will enhance their sustainability. To date, these reefs have been placed using deciding factors such as accessibility, fishing participation, number of anglers, logistics for construction and deployment, habitat limitations and conflict with commercial fishing and heritage values of the immediate area.

However, it is of great significance not only to consider the geographical distances between artificial reefs and natural peripheral habitats, but to take into account local currents and the predominant circulation patterns of the region, as these dynamics are responsible for the transport of zooplankton from its origin to the shelf (Siegel et al., 2003). Despite the proliferation of artificial reefs along coastal areas, few studies investigated their productivity in response to surrounding mesoscale circulation patterns. To fill this knowledge gab, circulation models with time and space continuous velocity fields can be used to study the distribution of zooplankton on the shelf in response to oceanographic settings.

1.5 Purpose and Objectives

This thesis concerns the study of the 3D circulation of the Hawkesbury Shelf Region (31.5-34.5°S) off southeast Australia, encompassing the dynamic EAC separation zone. A nested high-resolution hydrodynamic model is configured to investigate the mean, circulation and transport variability of the study region. The investigation of energy pathways reveals the dynamic nature of instabilities in the geostrophic upper ocean of the EAC separation zone and aid in understanding the model's capability in successfully downscaling mesoscale variability. Furthermore, knowledge of transport pathways will help to identify regions of open ocean / shelf interactions and their variability throughout the shelf. Finally, to reveal regions which will most likely be productive, the origin of waters reaching the Hawkesbury shelf is identified. Findings will greatly enhance the current knowledge of shelf dynamics throughout the study region.

The main objectives of this thesis are therefore as follows:

1. Configure a high-resolution nested hydrodynamic model for the Hawkesbury Shelf (31.5-34.5°S), southeast Australia for 2012-2013 and characterize the wavenumber spectra and dynamic instabilities in the EAC separation zone.

2. Understand the mean circulation, variability and volume transport on the Hawkesbury Shelf.

3. Identify the water transport pathways on the Hawkesbury Shelf and the source waters to an Offshore Artificial Reef.

1.6 Thesis Structure

The objectives of the thesis are addressed through the use of numerical modelling; configuring a high-resolution shelf model for the Hawkesbury Shelf and conducting simulation experiments over a two-year period (2012-2013). A summary of the purpose of each chapter and their specific aims is as follows:

Chapter 2 describes the configuration of the nested shelf model capable of simulating the high-resolution circulation on the Hawkesbury Shelf. The specific aims are:

1. Configure a high-resolution, nested hydrodynamic model to simulate the shelf circulation on the Hawkesbury Shelf for 2012 and 2013. Evaluate the model performance by comparison with observations from multiple sources (*i.e.* satellite derived and moored observations).

2. Characterize the energy transfer from the meso to the submesoscale in both models through wavenumber spectra of the upper ocean (upper 40 m).

3. Investigate the mesoscale variability on the shelf by determining the dominant type of dynamic instabilities of the mean surface flow in both models.

Chapter 3 characterizes the 3D circulation and spatiotemporal transport variability on the Hawkesbury Shelf; specifically, to investigate the cross-shelf exchange with the open ocean. The specific aims are:

1. Characterize the 3D circulation on the Hawkesbury Shelf for 2012-2013, its mean state and spatiotemporal variability.

2. Assess the transport variability in the along and cross-shelf direction to determine the major regions for water import and export on the shelf.

3. Determine the two-year mean and seasonal shelf transport budget.

Chapter 4 explores water transport pathways along the Hawkesbury Shelf to investigate regions most likely to receive offshore or inshore waters. Specifically, to identify source waters reaching an offshore artificial reef (OAR) located off the iconic Sydney Habour. A detailed physical oceanographic setting of the OAR is presented in this chapter. In addition, the oceanographic context for future OARs along the Hawkesbury Shelf is provided.

1. Determine how the major circulation patterns and seasonality affect water parcel trajectories on the shelf and at the Sydney OAR.

2. Determine the origin of water (depth and region) that flows over the shelf and the Sydney OAR.

3. Discuss the implications of the identified water sources on the potential productivity of new artificial reefs to be deployed within the Hawkesbury Bioregion.

Chapter 5 summarizes the main aims of the thesis and highlights the subsequent findings of this research.

Chapter 2

Configuration and Validation of the high-resolution Model for the Hawkesbury Shelf (31.5-34.5ºS)

2.1 Introduction

The shelf circulation off southeast Australia is exposed to high a mesoscale variability associated with its dynamic western boundary current, the East Australian Current (EAC). The frequent encroachment of eddies onto the shelf as the EAC separates from the coast (Gibbs et al., 2000; Mata et al., 2006; Cetina-Heredia et al., 2014) leads to complex oceanographic conditions.

To understand the impact of the EAC on the shelf circulation variability, before and after its separation from the coast, a number of field campaigns have been undertaken. Oceanic properties such as temperature and velocity data at locations up and downstream of the EAC separation have been measured in a series of process studies. These observations have led to an understanding of the circulation variability over and adjacent to the southeast Australian continental shelf (e.g Mata et al., 2000; Roughan and Middleton, 2002; Schaeffer et al., 2013; 2014; Wood et al., 2016, Sloyan et al., 2016). However, in view of the complex set of shelf processes, even these process studies using instrument mooring arrays were unable to adequately resolve the varying time and length scales governing the circulation variability on the shelf, particularly in the cross-shelf transport.

The analysis of complex shelf dynamics requires time and space continuous temperature and velocity fields and robust ocean models. Previous modelling studies in

this region, included the development of a simplistic, idealized model forced with climatological winds, which was unable to reproduce the EACs dynamic eddy field and variability (Godfrey, 1973). Further modelling attempts to advance knowledge with regards to specific EAC driven processes such as current and wind driven upwelling were undertaken by Gibbs et al. (1998) and Oke and Middleton (2000, 2001). A more recent study by Roughan et al. (2003) set out to investigate the fate of upwelled particle trajectories using the Princeton Ocean Model (POM); this model was configured for the East Coast of Australia with a variable grid spacing ~2.5-6 km in the cross-shelf direction and uses climatological forcing fields. Other process specific studies investigated the evolution, development, and over washing of eddies (Marchesiello and Middleton, 2000; Brassington et al., 2011; Mcdonald et al., 2012). The most recent development in investigating mesoscale variability is a reanalysis of the EAC region (Kerry et al., 2016). The model is configured to represent the mean state and variability of the mesoscale circulation and eddy variability. This eddy-resolving simulation is the first high-resolution ~2.5 km resolution reanalysis of the ocean-variability in this region.

Even though these studies improve our knowledge of the EAC's overall mean state, variability and eddy dynamics, their numerical simulations were mostly too coarse resolution to capture nearshore variability, mesoscale or process oriented or only hindcast a short time period only (*i.e.* ~ 20 days to 3 months at most). To communicate mesoscale features such as boundary current dynamics and planetary waves from coarser models to the shelf, the model resolution has to be downscaled. Downscaled models rely on their parent grid to supply forcing along the open boundaries, allowing the mesoscale circulation to propagate into the higher resolution grid. On continental shelves and in nearshore regions where variability can range on scales of meters to a few km, high resolution models are particularly important (Katavouta and Thompson, 2016). High spatial resolution is also an integral factor to represent the bathymetric features in regions with a steep continental slope, such as southeast Australia. In regions with a relatively flat and wide slope (New England Shelf, US) coarser models are often sufficient. Downscaled grids have previously been applied to model complex shelf regions adjacent to western boundary currents (*i.e.* the Gulf Stream, Agulhas and Kuroshio current) (Chen and He, 2015; Yang et al., 2011; Speich et al., 2006).

For a downscaled, high-resolution model to successfully simulate submesocale circulation features, the model has to be able to accurately depict mesoscale dynamics inherited from the parent grid first.

On the east coast of Australia, the mesoscale variability is dominated by mesoscale eddies, which are generated through instabilities in the flow field. Previous studies on the EAC have shown that the high eddy variability is dominated by barotropic instabilities (Mata et al., 2006). Therefore, by identifying the instabilities in the upper ocean in both the parent and nested model, the success of the nested model in reproducing the mesoscale variability can be determined. Flow instabilities in the ocean can be identified by examining the energy transfer between the major types of energy, including the mean kinetic energy (EKE), eddy kinetic energy (EKE), mean potential energy (MPE) and eddy potential energy (EPE), which ultimately determine the energy budget of the ocean (Kang and Curchitser, 2015). These transfer terms give insights into the dominant type of dynamic instabilities; hence, an estimation of the mesoscale variability in ocean models. Additionally, to test whether a nested model resolves circulation at smaller spatial scales compared to the parent model, a wavenumber analysis is commonly conducted to reveal the energies contained in the circulation at different scales. This is done to determine how the high-resolution model represents the sub mesoscale.

Nevertheless, further validation of the nested model is needed to establish its competence in reproducing the circulation and temperature on the shelf via comparisons with observations (*i.e.* satellite derived and moored observations). This will highlight the model skill in adequately simulating the nearshore or shelf variability, which is not captured in the parent model. Therefore, in this chapter, a high-resolution (750 m in space) shelf model is configured to represent the submesoscale continental shelf dynamics of the Hawkesbury Shelf. This provides the first high-resolution modelling effort encompassing the dynamic EAC separation zone.

2.2 Aims and Objectives

The overarching aim of this chapter is to describe the configuration and performance evaluation of the nested high-resolution model for the Hawkesbury Shelf. For the first time, high-resolution model results are presented for this region. This model will aid in understanding the impact of a western boundary current on the coastal and shelf circulation variability.

In this chapter, the specific aims are:

1. Configure a high-resolution, nested hydrodynamic model to simulate the circulation on the Hawkesbury Shelf for 2012 and 2013. Assess the model performance by comparison with observations from multiple sources (*i.e.* satellite derived and moored observations).

2. Characterize the energy transfer from the meso to the submesoscale in both models through wavenumber spectra of the upper ocean (upper 40 m).

3. Investigate the circulation variability on the shelf by determining the dominant type of dynamic instabilities of the mean surface flow in both models.

2.3. Model Configuration, grid setup and Implementation

2.3.1 Grid Setup and Model Domain

The modelling framework consists of a high-resolution limited area model (hereafter referred to as the Hawkesbury Shelf Model (HSM), Fig. 2.1, b), nested within a low-resolution, eddy resolving assimilation scheme of the EAC region configured over a two-year period, 2012-2013. The parent model, (hereafter referred to as the EAC model, Fig. 2.1, a) has a variable horizontal grid resolution with 2.5 - 6 km in the cross-shelf direction (increasing to 6 km outside the shelf break) and 5 km in the along-shelf direction. The vertical resolution consists of 30 sigma layers. Details of the EAC model development and validation can be found in Kerry et al. (2016). The HSM is nested inside the EAC model using the one-way method by Mason et al. (2009) and is configured over a two-year period (2012-2013).

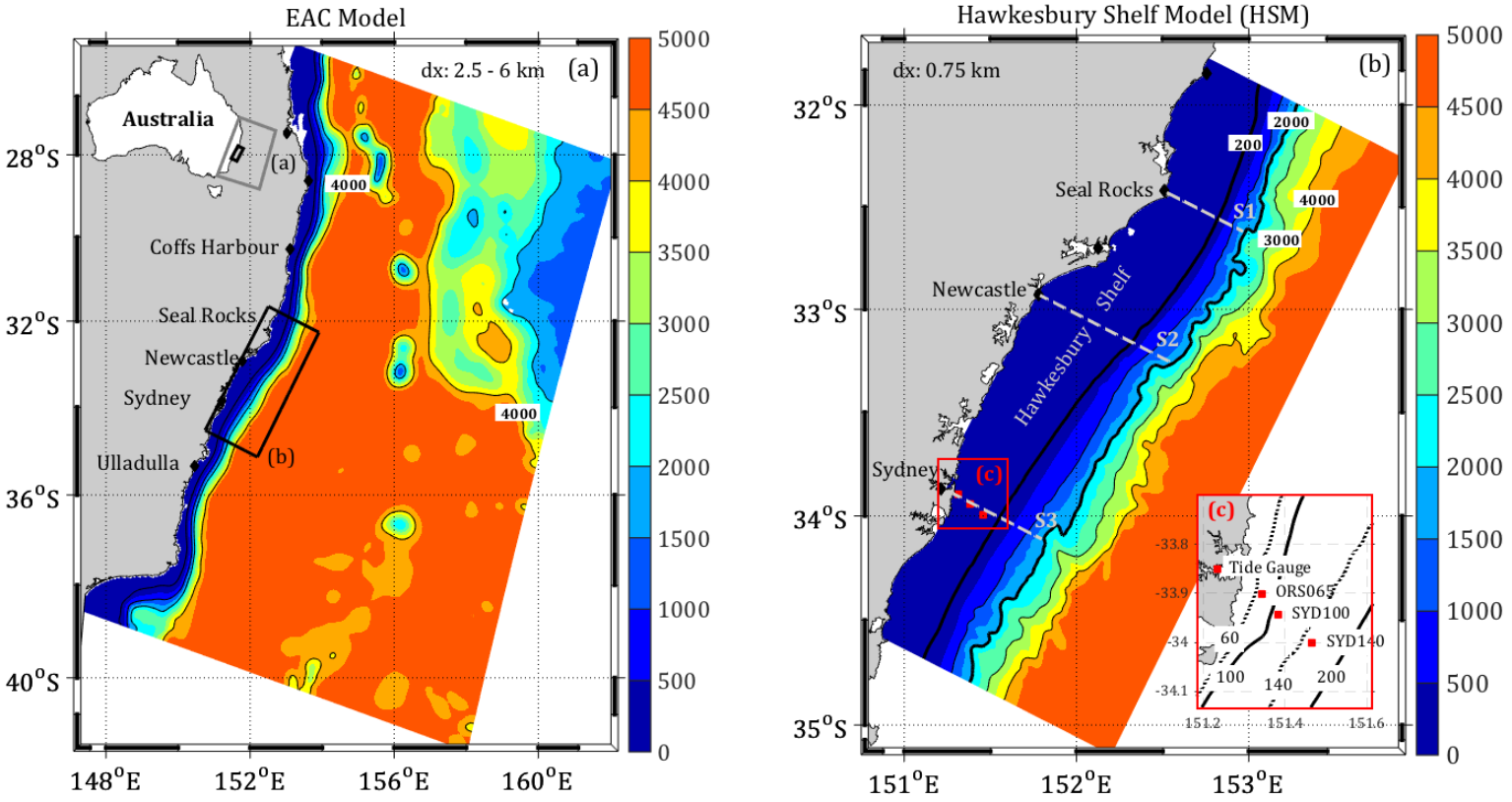

Fig. 2.1. Bathymetry (m) of (a) EAC model domain and (b) high-resolution Hawkesbury Shelf Model (HSM) domain. Across – sections that will be investigated throughout the thesis from 0-2000 m are shown at S1, S2 and S3. Mooring stations for ADCP current meters and temperature loggers are represented by red squares and are located within the red box (c). dx describes the horizontal cross-shelf resolution.

A 750 m high-resolution version of the Regional Ocean Modelling System (ROMS version 3.4) is configured for the Hawkesbury Shelf.

The current version of ROMS specifies the vertical grid in terms of separate transformation and stretching functions (Shchepetkin and MCWilliams, 2009), which are controlled by input parameters named Vtransform and Vstretching. For the transformation function the default Vtransform = 2 (see Shchepetkin and MCWilliams, 2009, equation 2.2) is used; for the stretching function the recently introduced Vstretching = 5 (Souza et al., 2015) is used. The latter uses a quadratic Legendre polynomial function, allowing a higher resolution near the surface and bottom. By using this scheme, the surface layer depth is kept relatively constant throughout the domain and ocean surface currents are more accurately resolved (Souza et al., 2015).

The regions throughout the water column, which need a higher or lower resolution, can be adjusted by accordingly fine tuning the stretching parameters $\theta_s \; and \; \theta_B$. These parameters determine the increase of resolution near the surface and bottom layers. Larger values of $\theta_s \; and \; \theta_B$ result in an increase of resolution in both the surface and bottom area but numerical stability needs to be maintained by keeping θ_s in a range between $0 \leq \theta_s \leq 10$ and θ_B between $0 \leq \theta_B \leq 5$. In this configuration, 30 vertical layers are stretched so that most of the resolution is focused within the upper water column, for depths less than 150 m (n=30) with $\theta_s = 6, \theta_B = 5$. (Fig. 2.2, Fig. 2.3). In addition, 30 vertical layers are implemented to assure consistency with the parent grid. This is of great significance to avoid mismatches along the boundaries while nesting. The choice of parameters was motivated to ensure (a) coverage of the mixed layer depth throughout the study region and (b) to resolve the bottom boundary layer (BBL).

This model configuration leads to a more realistic representation of the shelf and slope topography.

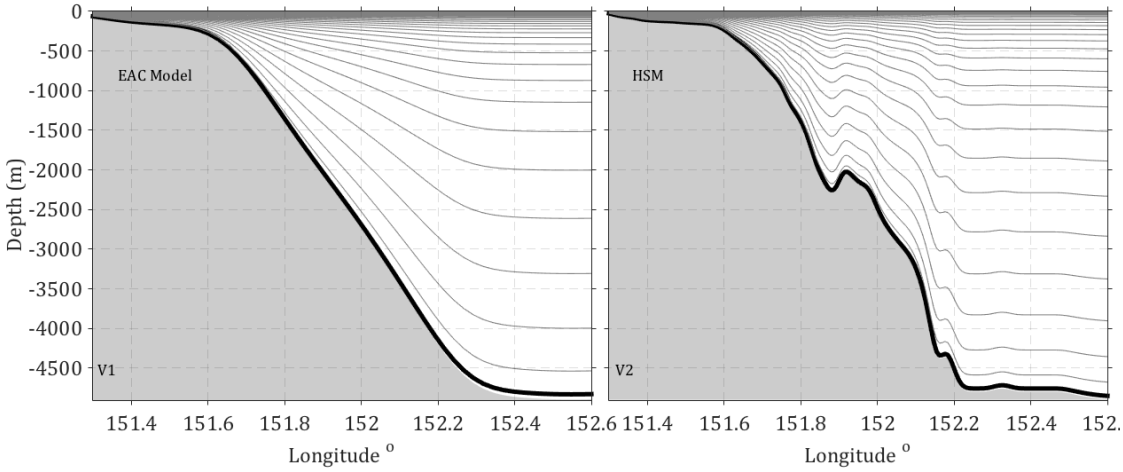

Fig. 2.2. Vertical distribution of sigma levels in the EAC model and Hawkesbury Shelf model (HSM, V2). Cross-sections are taken along grid cells at 33.82°S. V1, V2 stands for Vertical Cross-section. 1 and 2 denotes the EAC and Hawkesbury Shelf model.

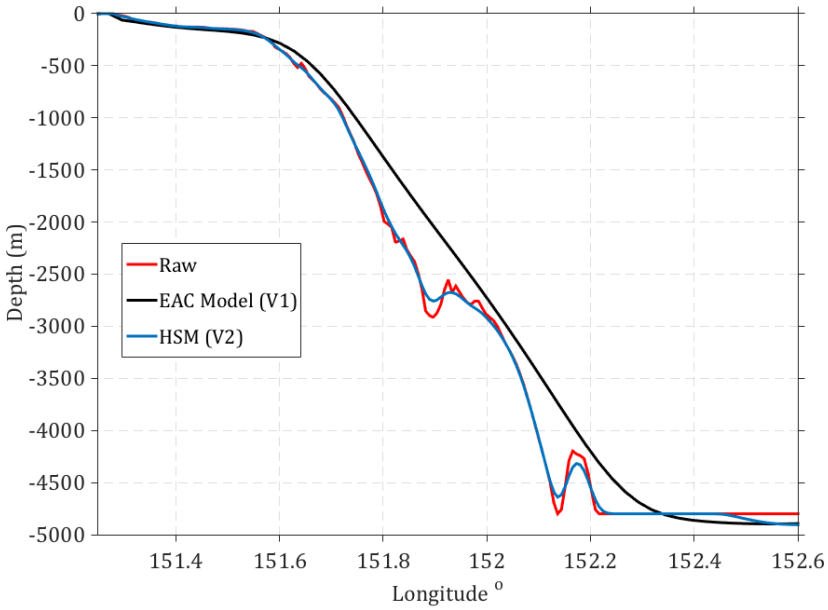

Fig. 2.3. Bottom depth represented by the EAC model, the high-resolution Hawkesbury Shelf Model and the raw bathymetry.

The realistic representation of the shelf's bathymetry introduces steep gradients, which can lead to synthetic flows along the shelf (Haney, 1991; Mellor et al., 1994, 1996). These flows were a result of numerical errors arising in the calculation of the pressure gradient term (HPG) (Haidvogel et al., 2000). The computation of the HPG in ROMS was described in detail by Shchepetkin and McWillams (2003). Thus, slight smoothing of the bathymetry was usually needed to ensure hydrostatic consistency and ensure grid stability (Shchepetkin, 2008).

The ROMS model used here was configured to use a fourth-order centered vertical advection of tracers, fourth-ordered centered vertical advection of momentum, third-order upstream horizontal advection of 3D momentum and third-order upstream horizontal advection of tracers for the mixing of momentum (Shchepetkin and McWilliams, 2003). ROMS uses a split-explicit time stepping scheme and, in this configuration, time steps for the barotropic and baroclinic motions are chosen to be 2.3 s and 32 s (Shchepetkin and McWilliams, 2005). The turbulent mixing scheme for the HSM was the Mellor and Yamada scheme 2.5 (MY2.5, 1982) to be consistent with the parent model setup (EAC model). In addition, as the main focus of the HSM is to simulate the mean, the MY 2.5 mixing scheme was most applicable as it has become standard for coastal ocean applications. Viscosity and diffusivity are scaled down from the EAC model according to the increased grid size of the HSM. Bottom drag is chosen following Lentz et al. (2009), who determined a common value for shelf areas. Instantaneous model outputs are saved in 2-hourly intervals in order to resolve tidal induced motions (~6 hours) and in addition daily averages are saved. Specific sensitivity tests have not been carried out with regards to model parametrization. A summary of the model parameters used are shown in Table 2.1.

Parameter	EAC model (Reanalysis)	Hawkesbury Shelf Model (HSM)
L (# of grid points in along-shelf direction)	315	477
M (# of grid points in cross-shelf direction)	270	197
Δx (horizonal cross-shelf resolution)	2.5-6 km	0.75 km
Δy (horizontal along-shelf resolution)	5 km	0.75 km
Δt (baroclinic time step)	300 s	32 s
Δt_{fast} (barotropic time step)	35 s	15 s
Rdrg 2 (quadratic bottom drag coefficient)	3.0×10^{-3}	3.0×10^{-3}
Δt_{save} (outputs saved)	4 hrs	2 hrs
Turbulent Closure Scheme	Mellor-Yamada 2.5	Mellor-Yamada 2.5
Grid Geometry		
N (number of sigma levels)	30	30
θ_s (surface stretching parameter)	8	6
θ_b (bottom stretching parameter)	5	5
Tcline (critical depth)	400 m	150 m
Stretching Scheme	5	5
Grid Rotation Angle	-20 (deg)	-27 (deg)
Atmospheric Forcing	BOM ACCESS (12 km)	BOM ACCESS (12 km)
Initial and Boundary Forcing	Bluelink Reanalysis (BRAN3.5) Applied daily	EAC model buoyancy fields (SSH, VBAR, UBAR, U, V, Salt, Temp) Applied every 4 hrs
Tidal Forcing	--	TPXO8 Atlas M2, S2, N2, K1, O1, Q1

Table 2.1. Summary of the most important model setup parameters of the EAC model and Hawkesbury Shelf model (HSM).

2.3.2 Open Boundary and Initial Conditions

Sea surface height, temperature, salinity and current velocity outputs from the EAC model (the parent model in this case) were saved as snapshots in 4 hourly increments over the two-year simulation period and specified as the open boundary and initial

conditions (OBCs). The radiation and nudging scheme by Gan and Allen (2005b) was applied including the adaptation for the oblique radiation (Marchesiello et al., 2001).

To avoid noise generation in the boundary file creation process, induced by depth mismatches between the grids, bathymetries are gradually merged over the regional baroclinic Rossby Radius of 19 km (25 grid cells) along the eastern, northern and southern boundary (Mason et al., 2010). Penven et al. (2006) showed that the downscaling of grid resolution along the open boundaries should follow a reasonable ratio of 3:1 and 7:1 between the models. In this thesis, the downscaling ratio was about 3:1 to 5:1. Due to the difference in grid rotation between the two models (-20 degrees for the EAC and -27 degrees for the HSM (Table 2.1) and the variable cross-shore resolution of the EAC model, the ratio of 3:1 increases to 5:1 throughout the eastern boundary. The improvement achieved in resolution along the southern boundary is illustrated in Fig. 2.4.

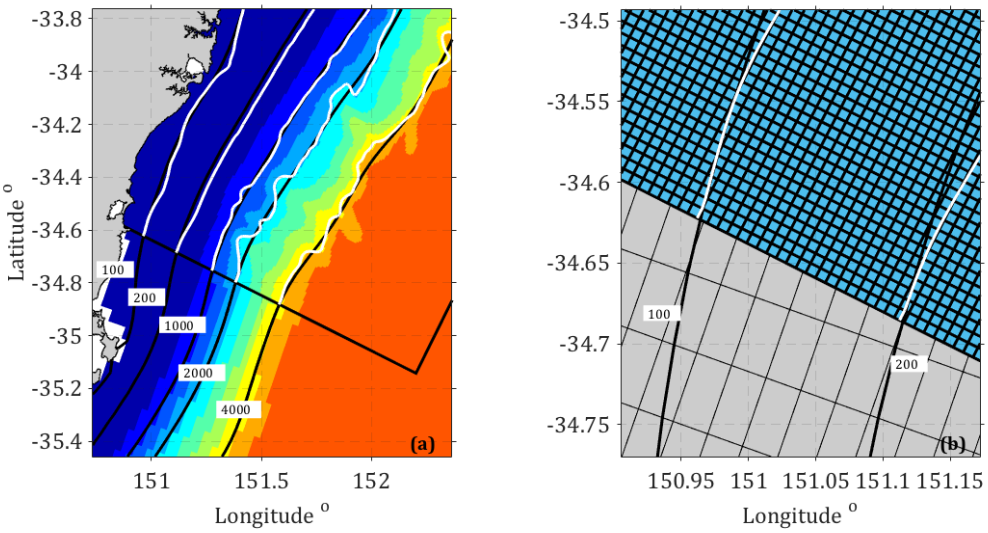

Fig. 2.4. (a) Zoom of the bathymetry showing the southern boundary of the Hawkesbury Shelf model (HSM) and demonstrating the matching of the EAC model bathymetry to that of the HSM boundary region. HSM isobaths are shown in white, EAC model isobaths are shown in black. (b) Schematic showing the improved grid cell resolution along the southern boundary of the Hawkesbury Shelf Model (HSM). Blue shows the grid cell dimensions of the finer grid (HSM) and grey shows the coarser grid (EAC model).

Along the open boundaries, commonly used conditions including the Flather (Flather, 1976) and Chapman condition (Chapman, 1985) were applied to 2D velocities and sea surface height with free-slip boundary conditions on land. For 3D variables, the nudged-radiative boundary condition was used (Marchesiello et al., 2001) with different nudging time scales for inward and outward propagation. 3D variables were nudged at

the OBCs with no nudging of the entire interior domain towards the large-scale climatology and no sponge layer has been applied. The ratio between inward (active) and outward (passive) propagation in this configuration was set to be OBCFAC=15. Thus, the nudging timescale for outward propagation was set to daily with an inward propagation set to 1/15.

2.3.3 Bathymetry

The HSM's grid bathymetry was interpolated using bathymetry data from 2 sources, Sydney Ports and from Geosciences Australia. Inside the Sydney Harbour Estuary, bathymetry from high-resolution bathymetry (25 m) was provided by Sydney Ports. Outside the harbour and throughout the domain, a coarser bathymetry from Geosciences Australia was used (*i.e.* 50 m Multibeam Dataset for Australia, Whiteway, 2009).

Minimum water depth across the domain was limited to 4 m for numerical stability with a maximum depth of 4910 m. All depths exceeding 4910 m were truncated since information at depths deeper than that won't largely impact the shelf circulation.

Since the interaction of the EAC with the shelf plays a key role in this thesis, preserving the shelf bathymetry while applying the required smoothing is of highest priority. The bathymetry is generally smoothed to minimize pressure gradient errors (HPGEs) and allow for a numerically stable grid, satisfying the CFL criterion (Courant-Friedrichs-Lewy condition for computational stability). Values responsible for the grid stability are the r-factors including the 'bathymetric roughness parameter' (rx0) (Beckmann and Haidvogel, 1993) and the 'hydrostatic inconsistency parameter (rx1) (Haney, 1991; Martinho and Batteen, 2006). Rx1 is a measure of HPGEs while rx0 is the associated slope factor. In this case, the bathymetry is smoothed with r-factors rx0 = 0.18 and rx1=9.9. Quantities of rx0 and rx1 are domain maximum values of the respective parameters.

The conventional smoothing method for bathymetry, such as the Shapiro filter, has known limitations especially in shallow shelf regions. Therefore, to smooth the bathymetry of the HSM a linear programming technique described in Sikiric et al. (2009) is applied. Rx1 is strongly controlled by the near bottom grid resolution and thus, to better resolve the bottom boundary layer of the HSM, has been pushed above the usual

range ($3 < rx1 < 7$) (Shchepetkin and McWilliams, 2003). Even though rx1 is outside the conventual range, no grid instabilities or blow-ups were observed during the simulation. Fig. 2.3 illustrates the bottom depth of both grids after smoothing along and the raw bottom depth. This demonstrateed that the HSM not only preserves the original shape of the shelf, but also the minimal amount of smoothing applied.

2.3.4 Atmospheric Forcing

Both the EAC model and the HSM were forced with the same atmospheric forcing data with a 12 km spatial and 6 hourly temporal resolution. Data was made available by the Australian Community Climate and Earth-System Simulation (ACCESS) analysis (Puri et al., 2013). It is likely that higher resolution wind forcing would improve the very representation of the ocean very near the coast where high resolution features become important (such as sea breezes).By applying the standard bulk flux algorithm (Fairall et al., 2003), ACCESS wind fields, air temperature, relative humidity and air pressure are used to calculate the Air-Sea fluxes of momentum and buoyancy. Typically, along the southeast coast of Australia, rainfall is low and river inflow has minimal impact on shelf flows except during time of extreme rainfall, thus, river inflow is neglected (Schaeffer et al., 2016). While the inverse barometric effect may be important in fine scale shelf modelling, it was not included in the nested model to avoid errors along the boundaries where the model is nested.

2.3.5 Tidal Forcing

The main constituents of the diurnal and semidiurnal tidal band (M2, S2, N2, K2, K1, O1, P1, Q1), derived from a global barotropic tidal model, the (TPXO8 Atlas), were used to represent the barotropic tides in the model. The TPXO Atlas assimilates satellite observations with a resolution of 0.25^{o} (Egbert and Erofeera, 2002). As required by the boundary conditions, both phases and amplitudes for the surface and velocity are prescribed in the forcing file, which is applied along the lateral open boundaries.

2.4 Model Validation

The mesoscale EAC model has previously been validated against observations (Kerry et al., 2016) and shown to successfully capture the mesoscale variability. However, coastal applications require a higher resolution on the shelf and the inclusion of tides.

Available temperature and velocity observations that lie within the HSM domain were assimilated into the EAC model (by Kerry et al., 2016) which provided the boundary and initial conditions for the nested HSM. These include the data from the SYD140 mooring. Thus, is was expected for the assimilated model to closely represent the observations. Assessment of the nested model's performance was undertaken against both assimilated and non-assimilated observations (including ORS065 and SYD100 data). Various parameters such as correlation, Root Mean Square Difference (RMSD) and standard deviations were calculated on model simulations to statistically quantify the performance of the downscaled model setup. All the analysis was carried out by transferring model output into observation grid and time.

2.4.1 Nesting

To highlight the benefit of the higher-resolution model in resolving the coastline, surface plots of temperature (two-year mean) for each model resolution along with a vertical cross-section intersecting Sydney was presented. The model suit consisted of 3 grids with a variable cross-shelf resolution (dx) ranging from ~ 10, ~ 2.5 and ~ 0.75 km for Bluelink (supplies the EAC with boundary conditions), the EAC model (supplies boundary conditions to the HSM) and the HSM itself, respectively. The surface layer for the associated models have been used to represent the sea surface. Even though the surface layer of each model has slightly different thickness, the horizontal change in SST has previously been determined to be larger than in the vertical and thus interpolating to the same depth would not modify the gradients (over the whole domain) significantly.

The surface layer depths for different grids were as follows:

i. Bluelink (constant z-level): 2.5 m

ii. EAC model (sigma-layer): 0.3-3.5 m from the coast out to the 4000 m isobath.

iii. HSM (sigma-layer): 0.03 -1.67 m from the coast out to the 4000 m isobath.

To demonstrate the successful resolution downscaling of the HSM, a time series of instantaneous temperature difference plots from the EAC gridded onto the HSM from the initial condition at intervals throughout the run were presented. These plots showed the impact of the EAC model on the HSM and highlighted which parts of the domain contained the additional resolved scales. In addition, this analysis revealed if the open boundaries dominate the HSM's interior or if the interior can evolve independently.

2.4.2 Sea Surface Temperature (SST)

The surface sigma layer representing surface temperature from both the EAC model and HSM have been compared to Sea Surface Temperature (SST) observations from AVHRR (Advanced-very high-resolution radiometer) L3S daily merged maps from 2012-2013 (http://www.ghrsst.org). This product does not include observations through clouds but its high-resolution (2 km x 2 km) near the coast gives important insights into temperature gradients on the shelf. Model outputs were re-gridded into observational space and statistical parameters were computed for periods with no cloud cover. SST observations exhibit a patchy structure, thus, only days with more than 15 % of spatial coverage were kept. Data with less than 15 % of coverage does not provide enough spatial information.

In general ocean models are validated using either SST observations from night or above a certain wind speed threshold to avoid the diurnal cycle as the satellite observations have strong biases during the daytime. Here, a time-series of domain-averaged wind stress (Fig. 2.5) showed that that 97 % of the time, the wind stress was greater than 0.01 Pa (~2.5 ms^{-1} at a height of 10 m). Winds of this magnitude trigger vertical mixing in the near surface layer and are most likely sufficient enough to destroy any stratification in the surface few centimeters. This assumption is based on Lentz (1992), who revealed the subtidal variability of the surface mixed-layer depth can be wind

driven and scales at u*/sqrt(Nf) (detailed derivations can be found in Lentz (1992)). Thus, any SST skin formed due to the diurnal cycle would be mixed through. Therefore, the AVHRR SST represented the SST for a much deeper layer than just the top few centimeters and the use of AVHRR day/night composite is justified in this case.

The main objective of this comparison was to provide a skill assessment for the spatial and temporal variability of SST throughout the modelling system (EAC model and downscaled HSM).

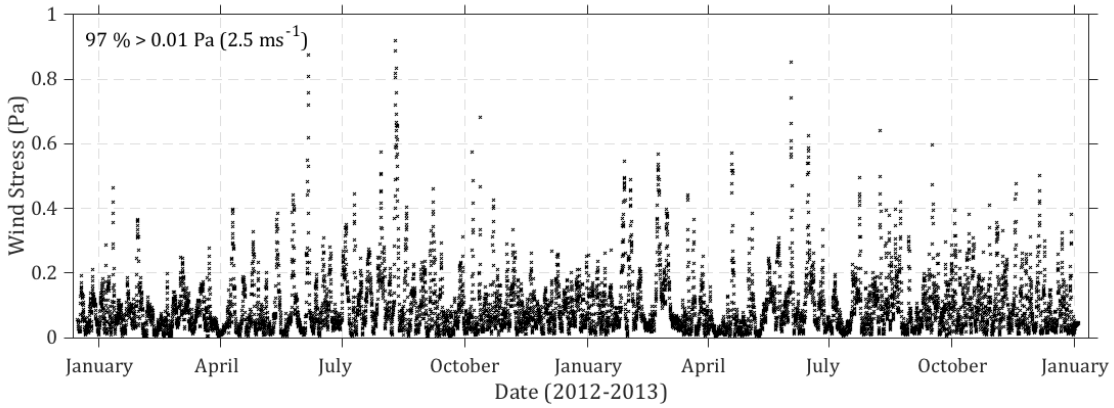

Fig. 2.5. Timeseries of domain-averaged wind stress interpolated onto the HSM for 2012-2013.

2.4.3 Barotropic Tides

To validate sea level variations simulated by the HSM, modelled tidal phases and amplitudes were compared to observations from the Fort Denison Tide Gauge. The Fort Denison tide gauge, being the only tide gauge available inside the HSM domain, was located 1.2 km inside the Sydney Harbour Estuary in 8.45 m water depth. Within the model grid domain, it was located 4 grid cells (3km) upstream from the first wet grid cell in the model at 9.7 m water depth resulting in a tidal lag. The tidal lag for the entire estuary has been estimated to be approximately 10 minutes from the mouth of the estuary.

Tidal harmonics from both the modelled (m) and observed (o) sea level elevations were estimated through harmonic analysis (Pawlowicz et al., 2002). In addition, to quantitatively compare both phases and amplitudes of the data, the absolute RMS error following the method by Cummins and Oey (1997) was used.

$$RMS = \sqrt{\frac{1}{2}(a_o^2 + a_m^2) - a_o a_m \cos(p_o - p_m)};$$

where phase and amplitudes were represented by (a and p - relative to the Greenwich meridian) with subscripts o and m standing for observed and modelled, respectively.

2.4.4 Comparison with in situ Temperature and Velocity Data

Data used for validating the coastal regions via the HSM (Fig. 3.2) included temperature and velocity observations from the NSW (New South Wales) IMOS (Integrated marine Observing Systems) mooring array located off Sydney (Fig. 2.1.c, Table 2.2). Details of the instrumentation, sensors, data quality control and processing can be found in Roughan and Morris (2011). The mooring array consisted of three moorings located across the continental shelf at 2, 10 and 19 km from the coast. The moorings were equipped with ADCP current meter and moored temperature loggers throughout the water column. These moorings were installed to diagnose the influence of the EAC jet and eddies on coastal and shelf waters. The mooring array consisted of 3 platforms named SYD140, SYD100 and ORS065 (Table 2.2).

ADCP current meter data was recorded in 5 min intervals at 2, 4 and 8 m depth bins across the shelf (Table 2) and Temperature loggers at 4, 8 and 8m depth bins, but were averaged to hourly intervals for analysis in this study. For statistical assessments, model outputs were interpolated to mooring times and depths. Available time series were smoothed with a 38-hour low-pass filter using the PL64 filter (Rosenfeld 1983) to remove high frequency variability and inertial oscillations that cannot be captured by the 2-hourly model outputs. In addition, the observed and modelled velocities were rotated into along and across-shelf components.

Mooring Name	Location		Water Depth	Distance from Shore	Observation Depth Intervals		Sensor Depth Range	
					ADCP	Temp	ADCP	Temp
	Lat (° S)	Long (° E)	(m)	(km)	(m)	(m)	(m)	(m)
ORS065	33.8975	151.3153	67	2	2	4	7-59	16-67
SYD100	33.9429	151.3821	104	10	4	8	21-97	18-104
SYD140	33.9944	151.4588	138	19	8	8	39-127	26-143

Table 2.2. Location and depth information (sensor and observation depth intervals) of the NSW Mooring array off Sydney (Roughan and Morris (2011)). Mooring data for SYD140 and ORS065 are available from Jan 2012-Dec 2013, SYD100 from Sept 2012-Dec 2013.

2.4.5 Statistical Assessment of Model Skill

To gain an understanding of the model's ability to reproduce the mean circulation and temperature on the shelf, common statistical measures such as the mean, standard deviations and RMSD of temperature and velocity fields (u,v) were assessed against observations for both the EAC model and HSM.

The statistical measures are defined respectively as:

$$\text{Mean: } \bar{x} = \frac{1}{n}\sum_{i=1}^{n} x_i \;;$$

$$\text{Standard Deviation: } s = \sqrt{\frac{1}{n}\sum_{i=1}^{n}(x_i - \bar{x})^2} \;;$$

$$\text{RMSD: } err = \sqrt{\frac{1}{n}\sum_{i=1}^{n}(m_i - o_i)^2} \;;$$

Where $\bar{x}$ represents the time mean, x_i the time series of each variable; m_i are the modelled outputs and o_i the observed data.

In addition, a statistical assessment of the model performance for temperature across the shelf were presented in form of Taylor diagrams (Taylor, 2001). This

statistical tool simultaneously depicts the correlation coefficients, computed for times series, centered root mean square differences and normalized standard deviations (amplitude of variations) from a temporal mean between the simulations and observations. Model performance is greatest near the reference point.

2.4.6 Circulation Variability across the Shelf

To depict the model's ability to capture the circulation variability on the shelf, mean current and variance ellipses were computed at each mooring station (Fig. 2.1, c, Table 2.2) following the method by Emery and Thomson (1998).

The water column was divided into 3 depth bins to represent the upper, mid and bottom part of the water column. The bins sizes were based on the depth sensor ranges and associated bin depths at each mooring location (Table 2.2). Velocities were depth-averaged for each bin. The upper-depth bin included ranges from 39-63 m for SYD140, 21-45 m for SYD100 and 7-23 m for ORS065. The mid-depth bin included depths from 71-95 m for SYD140, 49-69 m for SYD100 and 25-41 m for ORS065. The bottom-depth bin ranged from 104-127 m for SYD140, 73-97 for SYD100 and 43-59 m for ORS065.

2.4.7 Surface Circulation Variability

The model's ability to capture the variability on the shelf is assessed by decomposing geostrophic surface velocities derived from altimetry and model outputs to find major spatial patterns through the use of Empirical orthogonal function analysis (EOF). The main motivation behind this analysis is to identify circulation structures associated with the EAC. In addition, this analysis is a tool to understand the HSM's capability in successfully downscaling mesoscale variability. In general, EOF analysis is often used in oceanographic and atmospheric science to expose dominant statistical patterns (Lorenz 1956). Results will reveal the particular variance of each mode with regards to its contribution to the overall variability. The temporal fluctuations of each mode are associated with a principal component (PC) time series, which shows the fluctuation signs as a function of time. In this analysis, real-valued EOF analysis

(Björnsson and Venegas 1997) is used to ensure that results have the same units as the original time series.

The EOFs were calculated using daily-averaged geostrophic velocity fields for the simulation period from 2012-2013. Modelled geostrophic currents were interpolated onto the altimetry data points with a resolution of 0.25 x 0.25º (Deng et al. 2010).
The model's sea surface (SSH) height was used to compute the zonal and meridional geostrophic approximations:

$$U_g = \left[-\frac{g}{f}\left(\frac{d\eta}{dy}\right)\right];$$

$$V_g = \left[-\frac{g}{f}\left(\frac{d\eta}{dx}\right)\right];$$

With g representing the gravitational acceleration, f the Coriolis parameter, zonal and meridional gradients of SSH are $\frac{d\eta}{dy}$ and $\frac{d\eta}{dx}$. U and V were then rotated into along and across-shelf velocity components.

2.4.8 Energy Spectra

Spectral analysis is a useful tool for describing the main properties of a current time series and to identify dominating spectral bands. In particular, by combining spectral information in the along and across-shelf components, rotary spectral analysis determines a possible polarization of the flow (Gonella, 1972, Lilly and Odella, 2010). In this case, rotary spectra from observed and modelled velocity time series were compared to detect tidal bands present in both models. Velocities (depth-averaged and at the 39 m mark) at ORS065, SYD100 and SYD140 (Table 2.2) were compared.

2.4.9 Wavenumber Spectra

The motivation behind the following analysis is to understand whether the nested HSM resolves circulation at smaller spatial scales compare to the parent EAC model. A wavenumber analysis revealed the energies contained in the circulation at different scale. Furthermore, the wave number spectrum gave insight on how energies were distributed at different scales and how energies were transferred between scales, based on the steepness of the resulting slopes (Djath et al., 2014). Slopes with a steeper inclination highlight the importance of energy in the mesoscale, while flatter slopes indicate more energy is contained in the submesoscale (Archer, 2016).

To investigate regions of dominant geostrophic currents, the upper 40 m of the water column were depth-integrated in both models. Due to the variable thickness of depth-layers in sigma-coordinates, velocity outputs had to be converted to regular z-coordinates. Regular z-coordinates not only have constant depth layers but also regular dimensions in the x-y plane (in the across and along-shelf direction). Thus, the EAC model grid, which varies throughout the domain from 2.5-6 km in the across-shelf direction to 5 km in the along-shelf direction, had to be interpolated to match 2.5 km in the across-shelf direction and 2.5 km in the along-shelf direction.

Daily output fields were then used to compute the KE spectrum. The spectral analysis was performed over the entire grid domain of the HSM with 349 x 316 grid points and 227 x 159 for the EAC model.

The wavenumber spectrum from modelled velocities was obtained by following the method described by Archer et al. (2018):

The first step to remove the dominant signal of the EAC from the velocities by using the Reynolds decomposition was as follows:

$$u^* = u - \bar{u};$$

$$v^* = v - \bar{v};$$

where ($\bar{}$) presents the two-year mean of the time series and primes (*) express deviations from the two-year mean, respectively.

In the second step, a Hanning window was applied to the velocities before applying the Fourier transform

$$\mathcal{P}_{\mathrm{u}}(\mathrm{k}) = |\mathcal{F}\ \mathrm{u}^{*}\ (\mathrm{k})^{2}|;$$

$$\mathcal{P}_{\mathrm{v}}(\mathrm{k}) = |\mathcal{F}\ \mathrm{v}^{*}(\mathrm{k})^{2}|;$$

With $\mathcal{P}$ being power, k is wavenumber and $\mathcal{F}$ represents the discrete Fourier transform, the Kinetic Energy (KE) wavenumber spectra K(k) was expressed as

$$\mathrm{K}(\mathrm{k}) = \frac{1}{2}[\mathcal{P}_{\mathrm{u}}(\mathrm{k}) + \mathcal{P}_{\mathrm{v}}(\mathrm{k})];$$

A detailed description of the method and steps applied can be retraced in Archer (2016), who applied the KE wavenumber spectra to the surface velocities within the Florida current obtained from HF radar.

To spectrum of KE for both the EAC model and HSM was then calculated by averaging the resulting spectral matrix, containing 745 daily velocity fields (daily means).

2.4.10 Energy Conversion Pathways

Shelf seas are influenced by processes associated with mesoscale circulation features of the adjacent open ocean (*i.e.* eddies and boundary currents) and the interactions between them (Zhong et al., 2016). Along southeast Australia, the interaction of the EAC and its eddies with the continental shelf plays a key role in driving the circulation variability on the Hawkesbury Shelf. Therefore, investigating the eddy-mean flow interaction on the shelf aids in understanding if eddies intruding on the Hawksbury Shelf actually extract or supply kinetic energy from or to the mean flow. Moreover, such analysis provides insight into energy redistribution processes, ultimately providing a tool to assess the nested model's (HSM) ability to capture mesoscale variability and the influence of resolution downscaling on model energetics

As a first step towards understanding the energy redistribution processes on the shelf, transfer pathways between the main energy reservoirs and the nature of the dynamic instabilities were determined.

The main energy reservoirs on the shelf and associated energy conversions were calculated based on the derivations made by Kang and Curchitser (2015). For the Hawkesbury shelf, the upper 40 m of the water column were depth-integrated in both models, as shown in section 2.4.9. Daily velocity fields were used to compute the following energy reservoirs (J m^{-3}):

$$MKE = \frac{1}{2}\rho_0\left(\overline{u^2} + \overline{v^2}\right);$$

U and v represent the along and across-shelf velocity components for the two-year simulation period, ρ_0=1025 kg m^{-3} is the constant background density and the horizontal bar above the values stands for the two-year time mean. Primes (*) express deviations from the two-year mean, respectively.

$$EKE = \frac{1}{2}\rho_0\left(\overline{u^{*2} + v^{*2}}\right);$$

$$u^* = u - \bar{u};$$

$$v^* = v - \bar{v};$$

While kinetic energy is associated with the velocity field, potential energy is a function of the mass field distribution. The two forms of potential energy (Kang and Curchitser, 2015) used in this study were

$$MPE = \frac{g^2\,(\bar{\rho} - \rho_r)^2}{2\rho_0 N^2};$$

$$EPE = \frac{g^2\,\overline{\rho^{*2}}}{2\rho_0 N^2};$$

With N being the buoyancy frequency such that

$$N = g.\ \rho_{0.}\ d\rho_r\ d_z;$$

$$N^2 = -\ g.\ \rho_{0.}\ d\rho_r\ d_z;$$

The energy transfer between the reservoirs was then performed using the Reynolds-averaged Navier – Stokes equations under the hydrostatic and Boussinesq approximations as derived by Kang and Curchitser (2015).

The conversion from MKE to EKE and EKE to MKE was determined as follows

$$\mathrm{MKE} \rightarrow \mathrm{EKE} = -\rho_0[\overline{u^*\mathbf{u}^*}.\nabla\bar{u} + \overline{v^*\mathbf{u}^*}.\nabla\bar{v}];$$
$$\mathrm{EKE} \rightarrow \mathrm{MKE} = -\rho_0[\bar{u}\nabla.\overline{\mathbf{u}^*u^*} + \bar{v}\nabla.\overline{\mathbf{u}^*v^*}];$$

The energy transfer from MKE to EKE was associated with barotropic disturbances, often caused by large horizontal shear induced by strong mean flows (Zhan et al., 2016). Positive values of MKE to EKE revealed that eddies draw energy from the mean flow causing a deacceleration. On the contrary, negative values indicated that eddies feed back into the mean flow, resulting in the acceleration of the mean flow through the decay of eddies (Oliveira at al. 2009).

The energy transfer from MPE to EPE and EPE to MPE was determined as follows

$$\mathrm{MPE} \rightarrow \mathrm{EPE} = -\frac{g^2}{2\rho_0 N^2}\,.\,\overline{\rho_a^*\mathbf{u}^*}\,.\,\nabla\overline{\rho_a}$$
$$\mathrm{EPE} \rightarrow \mathrm{MPE} = -\frac{g^2}{2\rho_0 N^2}\,.\,\nabla\overline{\rho_a}\,.\,\overline{\mathbf{u}^*\rho_a^*}\,;$$

In this case, the energy transfer from MPE to EPE was associated with baroclinic disturbances of the mean flow. Positive values of MPE to EPE, indicate that $\overline{\rho_a^*\mathbf{u}^*}$ is against the direction of the mean density gradient, thus, dissipation of potential energy occurs and MPE is converted to EPE. In the case of negative values, $\overline{\rho_a^*\mathbf{u}^*}$ is directed along the horizontal density gradient of mean density, and mean potential energy is generated throughout the mean flow.

At last, to understand the temporal evolution of the MKE and EKE over the entire domain, daily domain-averaged MKE and EKE time series have been computed over the HSM domain.

2.5 Results

2.5.1 Impacts of Nesting

Fig. 2.6 demonstrated the impact of nesting in representing the shelf and coast. The nesting approach was based on the scientific fact that to study shelf and coastal processes, the model has to resolve the transition over the shelf break and into the coastal ocean, which in turn, requires a fine resolution. Bluelink, with a 10 km horizontal resolution was lacking the fine scale resolution along the coast, therefore neglecting the impact of estuaries (Fig. 2.6, a, d, g). The resolution of the EAC model increased by ~ 50%, with 2.5 km over the shelf, slowly increasing to ~6 km outside the shelf break (Fig. 2.6, b, e, h). The HSM showed the finest and most realistic representation of the bathymetry on the shelf (Fig. 2.6, c, f, i).

Fig. 2.7 illustrated the successful nesting of the HSM. Temperature difference plots between the HSM and EAC model for monthly snapshots of 2012 showed that the HSM is not just offsetting the temperature by +/- 2 degrees but also resolving finer scales. Starting at the initial conditions, the difference between the models was neglectable since all the data came from the EAC model, dominating the HSM. As time progresses, the boundary difference became small, but the interior difference became larger (or different). Plots of the local Rossby numbers (Fig. 2.8) showed how the nested model resolved finer scales and the impact of open boundary conditions in smoothing out the scales. This further emphasized that the interior of the HSM evolved independently to the EAC open boundaries and finer scale patterns were revealed.

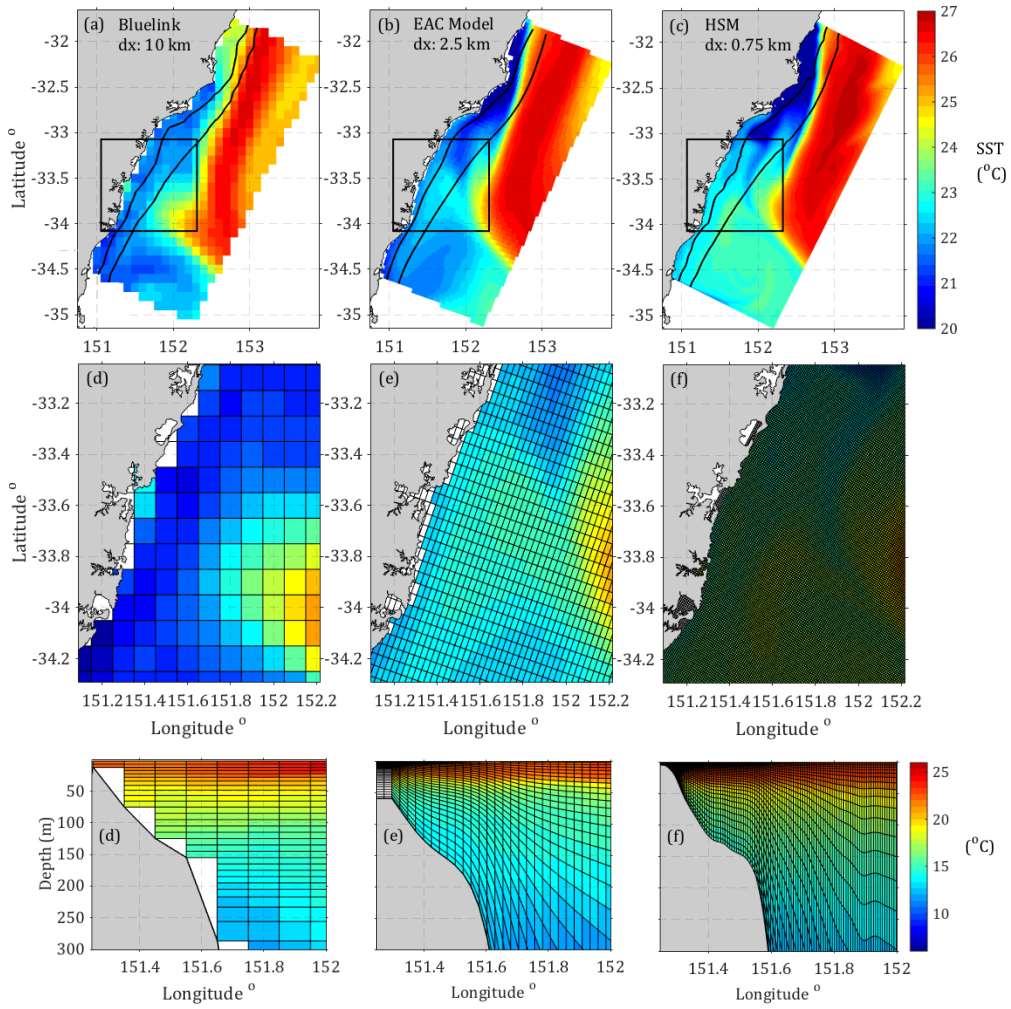

Fig. 2.6. Snapshot of domain wide sea surface temperature from 3 model resolutions for the 9 of January 2013: (a) Bluelink Reanalysis 10 km x 50 z-levels, (b) EAC model ~2.5-6 km x 30 sigma level, (c) HSM 0.75 km x 30 sigma levels. Black boxes show the boundaries of the zoomed region below (d-f). Solid black lines indicate the 100 and 200 m isobaths, respectively. Black across-shelf lines show the location of vertical sections (g-i). Red crosses are the locations of the across-shelf mooring stations used for in situ comparisons (Table 2.2).

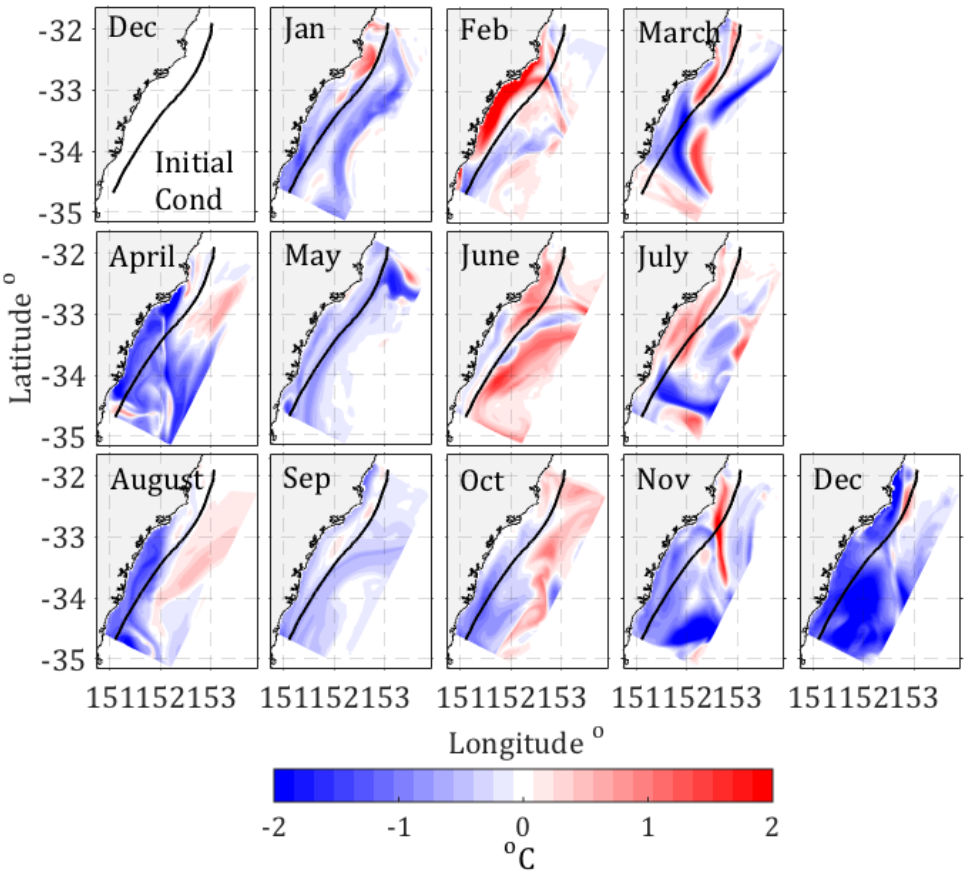

Fig. 2.7. Difference plots of temperature (both models have been interpolated to 2 m) between the EAC model and HSM at monthly intervals for 2012 (negative values indicate warmer temperatures in the HSM). Snapshots are taken at the 16th of each month at 00:00:00 hrs. EAC data has been interpolated onto HSM space. The black solid line represents the 200 m isobath.

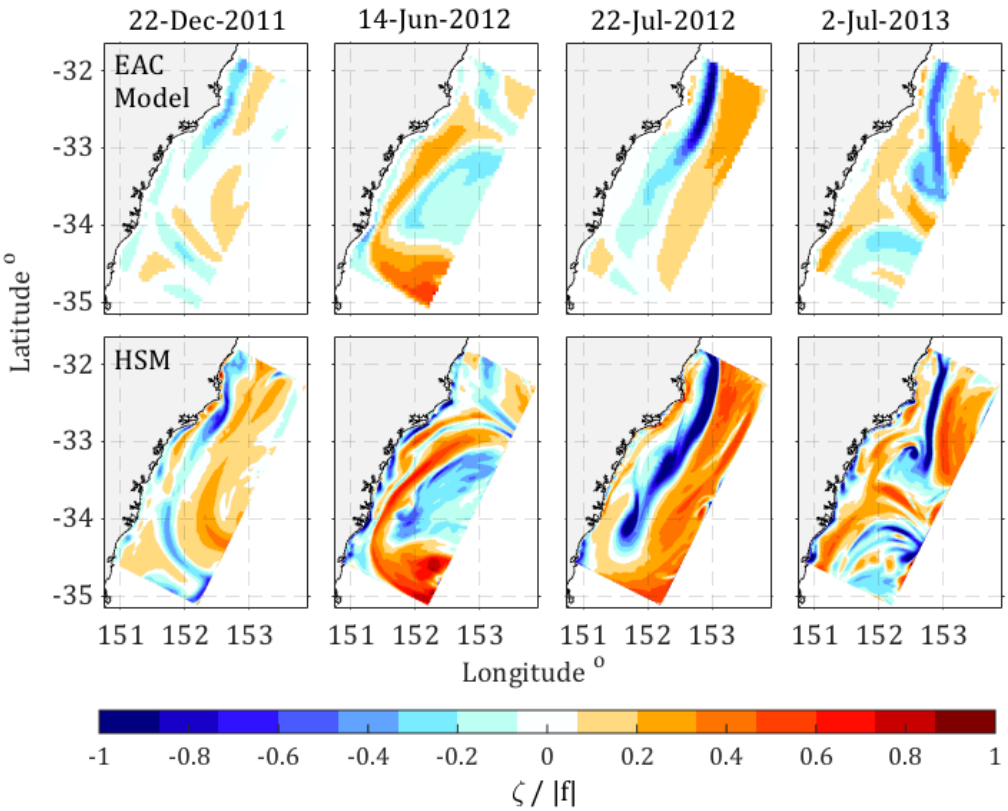

Fig. 2.8. Estimates of the Rossby number of the upper ocean vorticity divided by the absolute value of the Coriolis parameter (upper 40 m of the ocean were depth integrated). Upper row represents snapshots of the EAC model, Lower row of the HSM.

2.5.2 Sea Surface Temperature (SST)

Mean SST fields for 2012-2013 were extracted from AVHRR satellite data and compared with results from the EAC model and HSM. Comparisons revealed that both simulations reproduced the overall pattern of observed SST fields and their variability, induced by the meandering of the EAC (Fig. 2.9, a-c).

Inside the 200 m isobath, lower temperatures (19-21°C) stretched along the coast while offshore of the 200 m isobath, a warm water tongue (with temperatures reaching a maximun of 23°C) extended from 31.5 to 33°S. South of 33°S, that warm water tongue started to weaken and surface temperatures were lower with an alongshore temperature gradient of ~4°C. The two-year time series of the spatially averaged SSTs showed that both the HSM and the EAC model estimated temporal SST fluctuations well. Correlations (Fig. 2.9, g) were high with values of 0.98 (EAC model - AVHRR) and 0.96 (HSM – AVHRR).

Differences in temperature between simulations and observations showed in the RMSD (Fig. 2.10). Both models overestimated SSTs with an RMSD of 0.8°C throughout the entire domain. The largest RMSD (1.25°C) occured in the southeast part of the HSM (Fig.2.10). The EAC model presented overall lower RMSD values than the HSM, a direct consequence of satellite observations being assimilated into the EAC model. The temperature bias (difference) between the models and the observations were shown in Fig. 2.11. Both the EAC and HSM have a warm bias. The HSM has a temperature bias ranging from 0.5°C in the northeastern part of the domain to 1.5°C in the southern part. The SST bias in the EAC model is only very close to the coast. The bias is likely introduced by atmospheric forcing, which is only partially corrected through the EAC assimilation. Errors in parametrization of surface fluxes, mixing and boundary conditions can also lead to temperature biases.

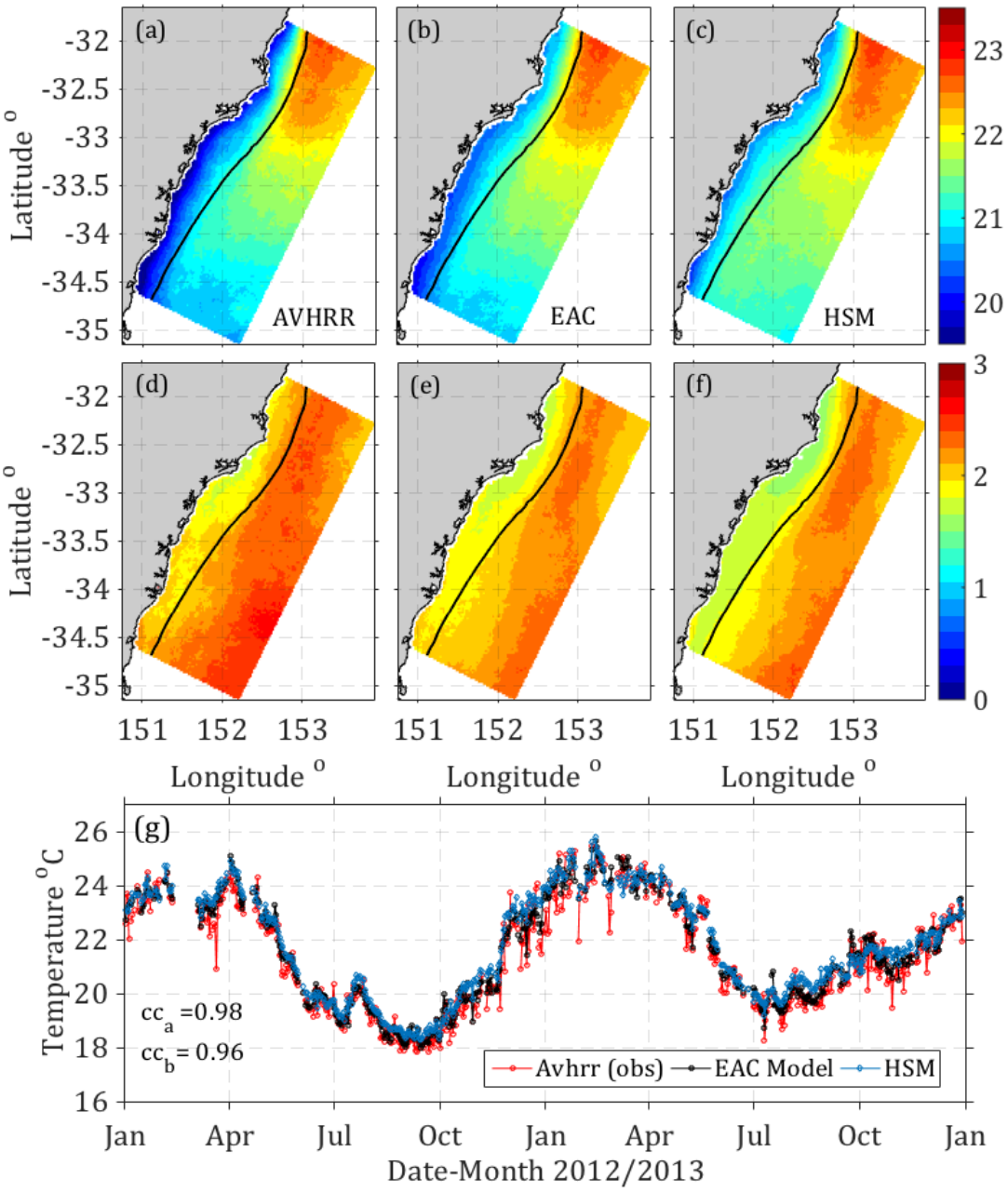

Fig 2.9. Domain wide two-year mean sea surface temperatures and their associated standard deviations. (a) AVHRR L3S satellite, (b) EAC model, (c) HSM. Black lines show the 200 m isobath. Associated standard deviations are shown in (d-f). (g) Spatial means for time periods with 15 % or more spatial coverage of satellite data. cc_a is the correlation between the satellite and EAC model SST, cc_b is the correlation between the satellite and HSM.

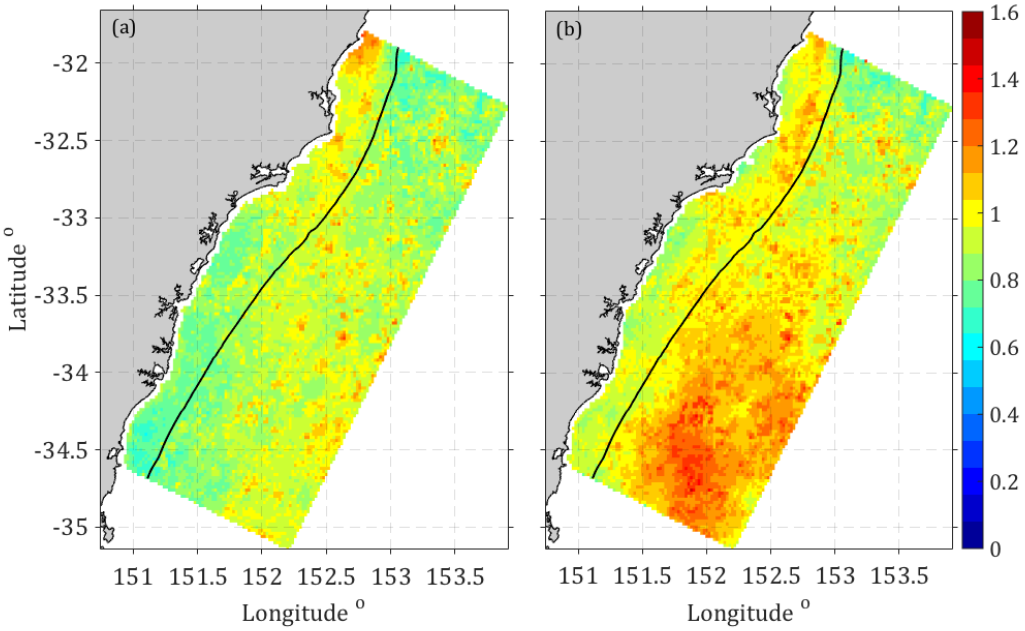

Fig. 2.10. RMSD comparisons for 2012 and 2013, calculated from daily averaged SST. (a) Satellite and EAC model, (b) Satellite and HSM. Black lines indicate the 200 m isobath.

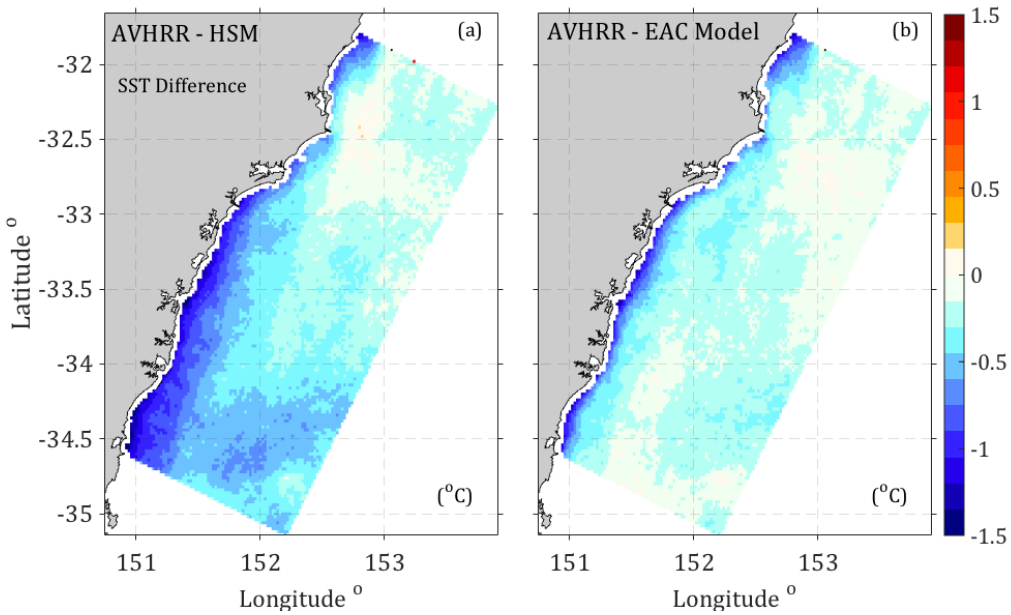

Fig. 2.11. Two-year mean temperature bias comparisons calculated from daily averaged SST. (a) Satellite and EAC model, (b) Satellite and HSM.

2.5.3 Barotropic Tides

Good agreement (correlation coefficient of 0.93, 95% confident intervals) between modelled and observed sea level heights indicate the HSM's skill in adequately reproducing sea level height variations induced by barotropic tides.

Comparisons of extracted tidal constituents show a good agreement in the semidiurnal tidal band (Table 2.3). Constituents M2 and S2 are underestimated by approximately 4 and 2 cm in terms of amplitude. Components of the diurnal tidal band, such as K1 and O1 are represented better with only 1 cm difference with regards to amplitude. However, the overall discrepancy resulting from amplitude and phase, as indicated by the absolute RMS is less that 10% for most constituents, except for K1 and S2, which exhibit an RMS of 38 and 16%, respectively.

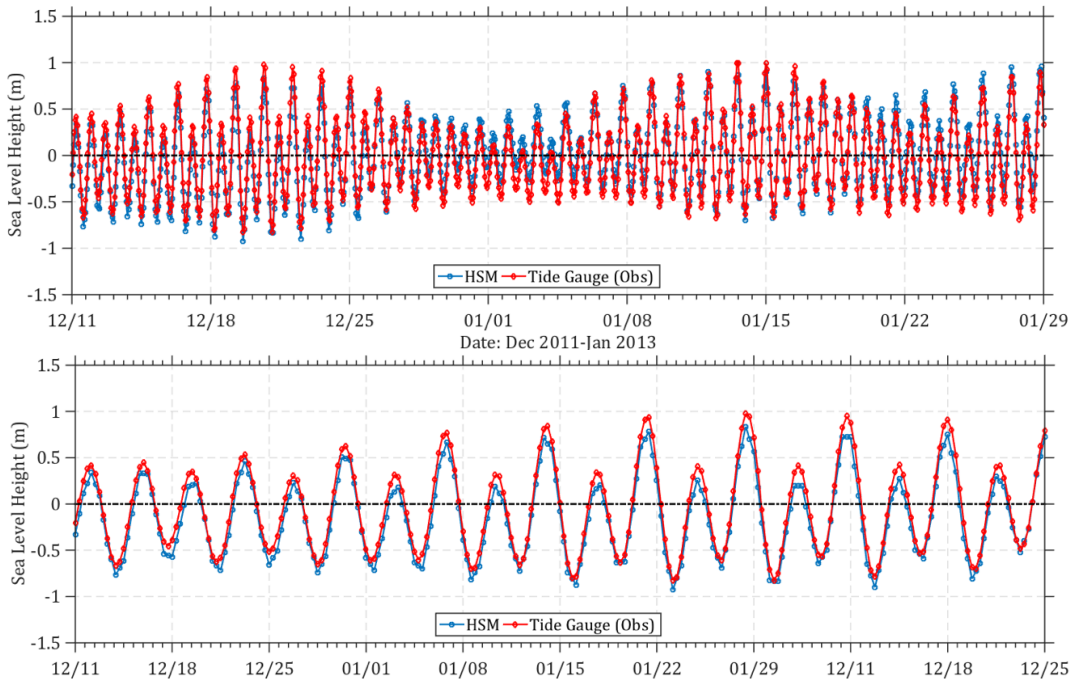

Fig. 2.12. Sea Level Height (meters) simulated by HSM (blue) and tide gauge data at Fort Denison (red). (CC=0.93, with 95% confidence level) between shelf model and tide gauge. (top panel): 48-day time series. (bottom panel) 18-day zoom. The mean has been removed from both series. CC is the correlation between the observed and simulated (HSM) time series. Both the model and tide gauge data are in UTC time.

Tidal Constituents		Amplitude (m)	Phase (°)	RMS (m)	RMS (%)
M2	Tide Gauge HSM	0.51 0.47	305.98 305.12	0.028	5.55
K1	Tide Gauge HSM	0.16 0.15	329.27 314.91	0.057	38.00
S2	Tide Gauge HSM	0.13 0.11	332.19 320.91	0.021	16.15
N2	Tide Gauge HSM	0.11 0.11	298.82 297.20	0.006	5.55
O1	Tide Gauge HSM	0.09 0.09	312.31 305.35	0.008	8.89
Q1	Tide Gauge HSM	0.02 0.02	287.98 285.99	0.001	5.00

Table 2.3. Comparison of surface amplitudes and phases between the Hawkesbury Shelf Model and sea level height observations at the tide gauge Fort Dension in Sydney Harbour. Phases are relative to Greenwhich, respectively.

2.5.4 Comparison with In Situ Data

The two-year mean and associated standard deviations of modelled temperature, across and along-shelf velocities (Fig. 2.13) were assessed against observations from 3 shelf moorings off Sydney (Fig. 2.1c, Table 2.2).

2.5.4.1 Mean Temperature Structure across the Shelf

The observed two-year mean temperature values reached a maximum of 20.2°C at the outer shelf mooring SYD140 (located 19 km from the coast, close to the 200 m isobath) and 19.6°C at the inner shelf mooring ORS065 (located 2 km from the coast). Maximum modelled temperatures ranged between 20.9 - 21.3°C in the HSM and 20.6 - 20.8°C in the EAC model. By comparing the observed and modelled thermocline, the models exhibited a vertical temperature gradient of 0.5°C compared to the observed 1.6°C in the upper 50 m (Fig. 2.13, a,d,g; Fig. 2.14). In addition, modelled temperatures have a 2°C warm bias throughout the water column (Fig. 2.13, a, d, g; Fig. 2.14).

2.5.4.2 Mean Velocity Structure on the Shelf

Mean along and across-shelf velocities were well represented in the simulations. However, the HSM outperformed the EAC model, particularly at the inner shelf mooring (ORS065) (Fig. 2.13, b, c; Fig. 2.14). The along-shelf velocity component for the EAC model and HSM was strongest in the surface layer peaking at -0.2 m s^{-1} and -0.18 m s^{-1}. The overall across-shelf velocities were up to 50% weaker in magnitude compared to the along-shelf components and mainly onshore in nature. Peak across-shelf velocities were -0.1 m s^{-1} in the model and -0.09 m s^{-1} in the observations.

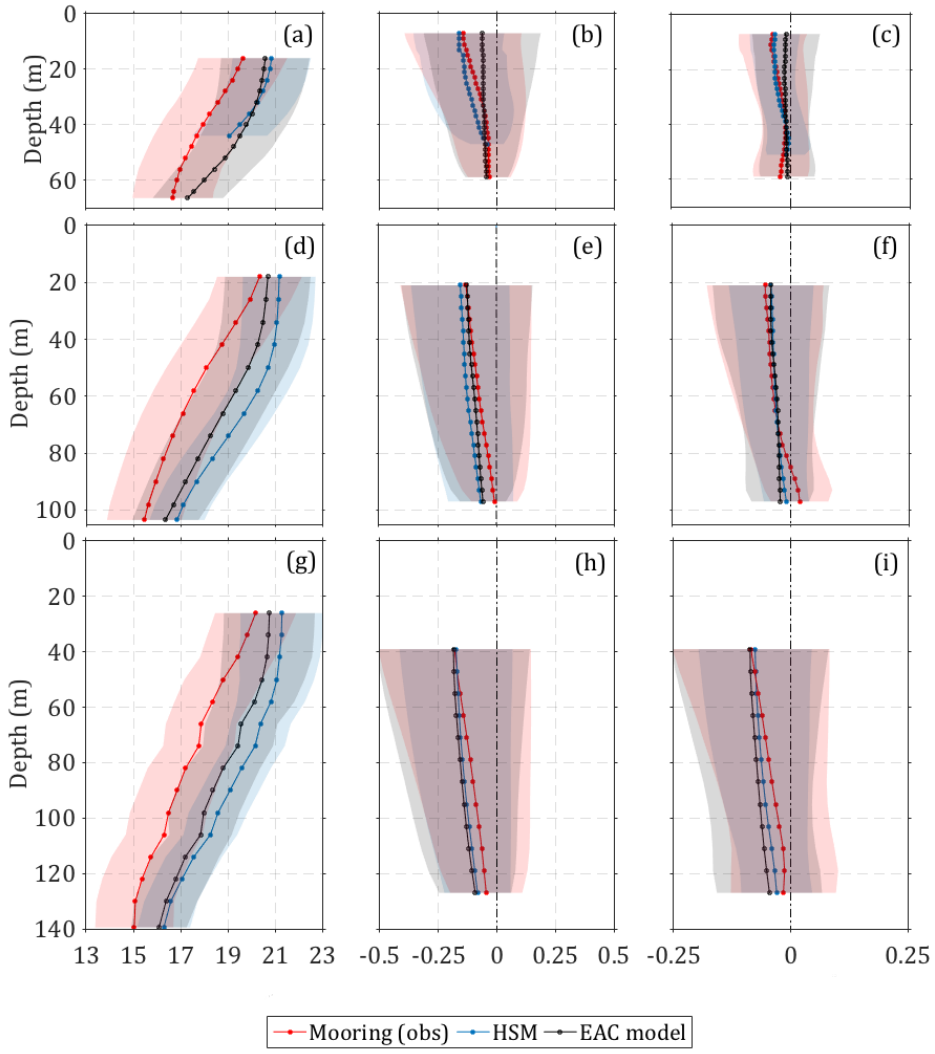

Fig. 2.13. Observed (red) and modelled (EAC model (black), HSM (blue)) vertical structure of the time-mean temperature (left column), along (middle column) and across-shelf (right column) velocities at the three mooring stations across the shelf (ORS065 (a,b,c), SYD100 (d,e,f), SYD140 (g,h,i). Shaded areas represent the associated standard deviations. Statistics are calculated over a two-year period for ORS065 and SYD140, and 15 months for SYD100. The black dashed lines indicate the 0 crossing.

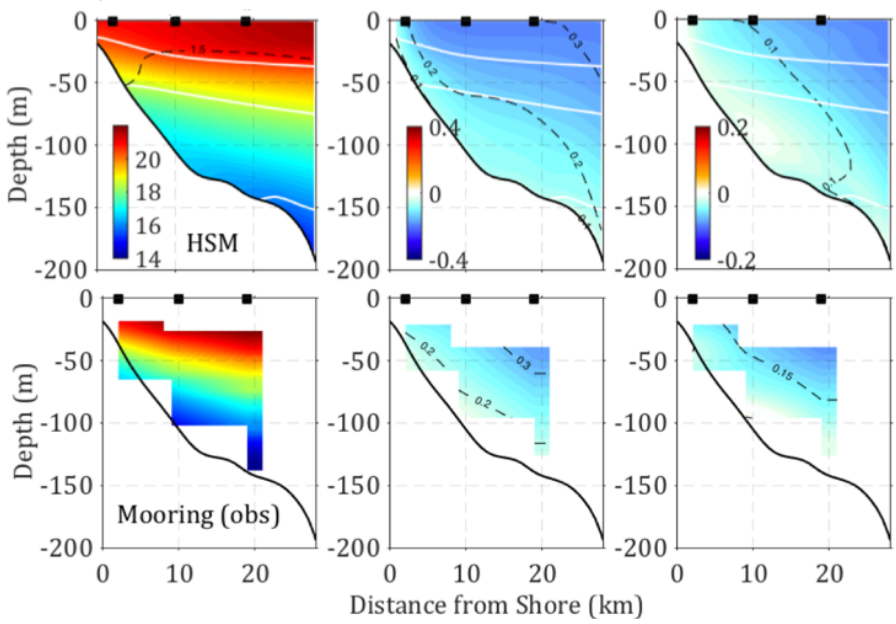

Fig. 2.14. Modelled (top panel) and observed (bottom panel) cross-section view of the mean temperature (left column), along-shelf velocity (middle column, negative poleward) and across-shelf velocity (right column, negative onshore) off Sydney (34°S). The location of the moorings is indicated by black squares. Dashed lines show the standard deviations with contour intervals of 0.5 for temperature, 0.1 for along-shelf and 0.05 for across-shelf velocities. White solid lines represent lines of constant density with a contour interval of 1024: 0.5: 1028 kg/m^3. Due to the lack of salinity observations at the mooring sites, no density lines are shown in the bottom panel.

2.5.4.3 Temperature Variability on the Shelf

To looker closer at the vertical temperature distributions based on temporal variability, standard deviations and correlations of temperature were determined; results were presented in Taylor diagrams (Taylor, 2001) in Figure 2.15. To identify the differences between the modelled and observed temperature fields, distinct colors and symbols were utilized for each variable (Fig. 2.15). The comparison was broken down with regards to the 3 cross-shelf moorings (Table 2.2). It has to be noted that even though the EAC model assimilated temperature only at SYD100 and SYD140 (Fig. 2.15, Table 2.2), readings at the ORS065 were most likely impacted by the assimilation due to the close proximity of the 3 moorings.

At the mooring closest to the shelf break (200 m isobath (SYD140)), correlation coefficients ranged from 0.39 to 0.78 for the HSM and 0.61 to 0.82 for the EAC model. The scattered distribution of points from both models also highlighted the varying model skill in the vertical structure. Better agreement with observations was achieved in the

upper (26-42 m) and near bottom depths (106-139 m). Larger discrepancies emerged in the mid water column, with lower correlations of 0.39 and 0.61 for the HSM and EAC model respectively. RMS amplitudes of modelled versus observed temperatures were between 1 and 1.4 for shallow depths. This indicated that the models produced fluctuations larger than observed for shallow depths and underestimating fluctuations throughout the middle water column (58-82 m). However, the normalized RMS amplitudes of the surface time series were close to 1, demonstrating that simulated temperature fluctuations had amplitudes close to the observed value. The RMS differences between the HSM and observations range from 0.69 -1.2. The EAC model ranged from 0.59 -0.85. These discrepancies among the two models resulted in spatially scattered points on the Taylor diagram (Fig. 2.10).

At the mid-shelf mooring (SYD100), correlations ranged from 0.44 - 0.88 for the HSM and 0.80 – 0.92 for the EAC model. RMS amplitudes were clustered around 1 for the EAC model and 0.75 for the HSM. The mid water column presented a decreased skill similar to the decrease at SYD140 (42-58 m). Both HSM and EAC model had high correlations between 0.73 and 0.85 with RMS amplitudes close to 0.9. This was an indication that the models underestimated fluctuations throughout the water column.

At the inner-shelf mooring (ORS065), correlations ranged from 0.73- 0.80 for the HSM and 0.71- 0.86 for the EAC model. RMS amplitudes are located round 0.5-0.75 for both models.

Overall, the spread of model points in the Taylor diagram was largest at the outer and mid-shelf mooring (SYD140, SYD100) and smallest at the inner-shelf mooring (ORS065). Results revealed a varying model skill in reproducing the vertical structure of temperature.

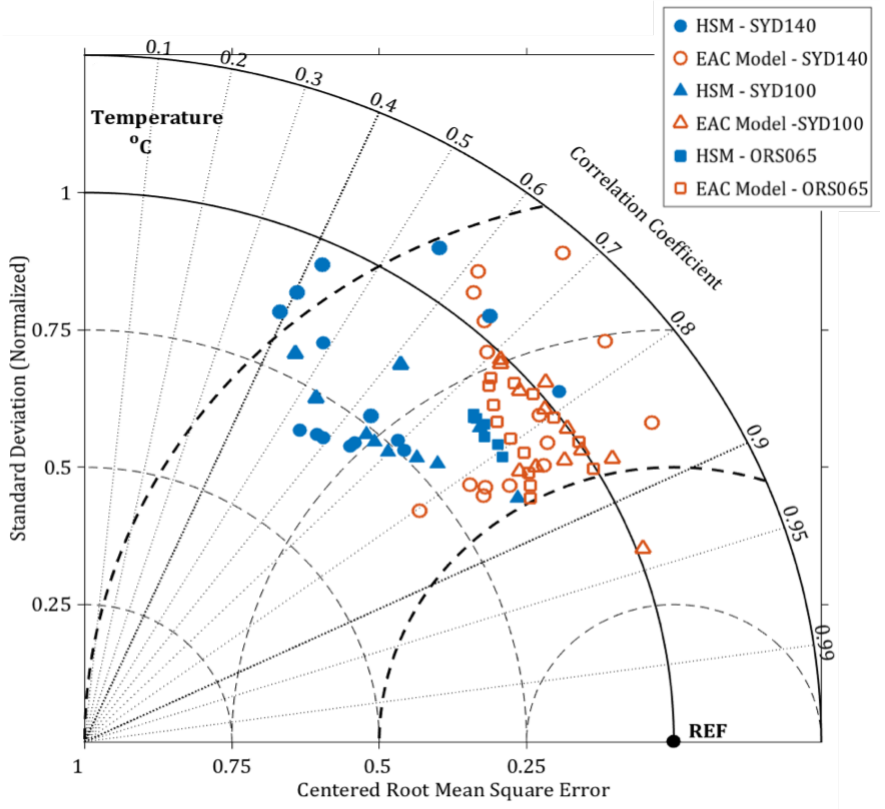

Fig. 2.15. Taylor diagram showing correlations, standard deviations and RMS errors between the model and the observations (from HSM in blue and EAC model in red) vs observations (Temperature loggers). The radial coordinate of the Taylor diagram is the normalized standard deviation with respect to observations, the angular coordinate is the Pearson correlation and grey arcs represent centered root mean square difference between the models and the observations. Circles: SYD140, triangle: SYD100, square: ORS065.

2.5.4.4 Circulation Variability across the Shelf

In agreement with the velocity observations at the three ADCP mooring sites (Table 2.2), modelled mean current velocities were predominantly poleward in direction and strongest in magnitude at SYD140 (Fig. 2.16, a-d; Table 2.4).

In the upper-depth bin, modelled along-shelf velocities were overestimated by 20% (0.03 m s^{-1}) at the ORS065 and by 27% (0.04 m s^{-1}) at SYD100. At SYD140 however, velocities were underestimated by 25% (0.04 m s^{-1}) (Fig. 2.16, b, Table 2.4. top panel). In the middle-depth bin, the HSM overestimated along-shelf velocities by 51% (0.06 m s^{-1}) at ORS065, by 39% (0.05 m s^{-1}) at SYD100 and 15% (0.02 m s^{-1}) at SYD140 (Fig. 2.16, c; Table 2. centre panel). The bottom-depth bin showed the largest overestimation of modelled along-shelf velocities throughout the water column with 56%

(0.04 m s^{-1}) at ORS065, 66% (0.06 m s^{-1}) at SYD100 and 42% (0.04 m s^{-1}) at SYD140 (Fig. 2.16, d; Table 2.4, bottom panel). The HSM successfully simulated direction and magnitudes of velocities on the shelf. The model was slightly less skilled at reproducing the variability, particularly in the along-shelf direction as indicated by the variance ellipses.

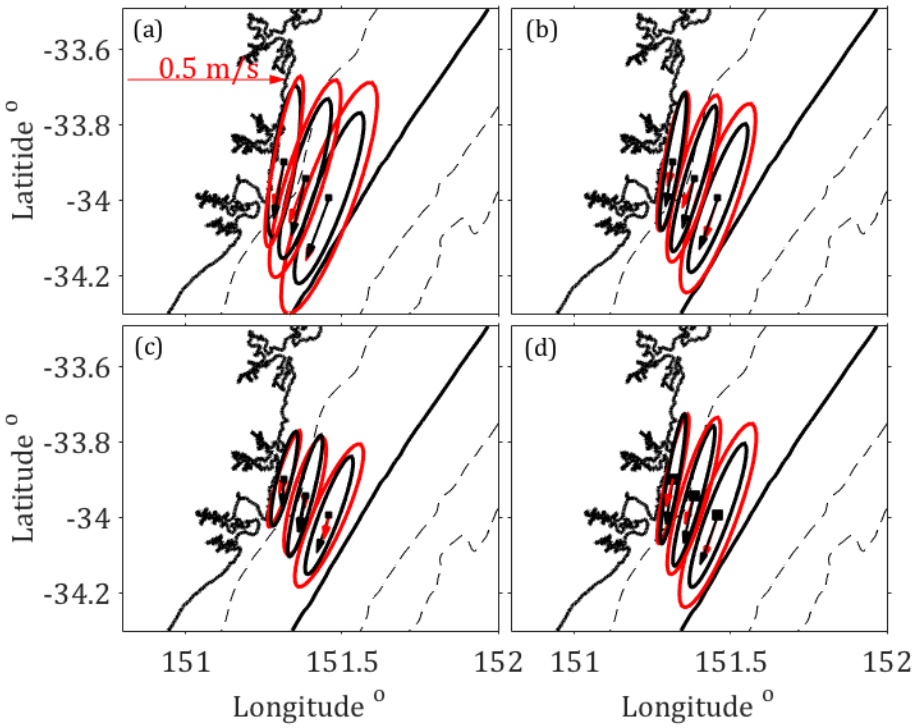

Fig. 2.16. Mean current vectors and variance ellipses of modelled (HSM, black) and observed (red) velocities for 2012-2013. Dashed lines show the 100, 1000 and 2000 m isobath; the solid black line shows the location of the 200 m isobath. (a) Upper - depth bin, (b) mid - depth bin, (c) bottom - depth bin and (d) depth - averaged velocities.

Upper		ORS65	SYD100	SYD140
U Across-shelf (m s^{-1})	Mooring HSM	-0.034 -0.034	-0.049 -0.042	-0.073 -0.055
V Along shelf (m s^{-1})	Mooring HSM	-0.120 -0.148	-0.114 -0.149	-0.163 -0.128
Major axis orientation (º)	Mooring HSM	12.89 10.74	21.04 19.27	24.16 24.23
Minor axis orientation (º)	Mooring HSM	0.03 0.04	0.06 0.04	0.08 0.04

Middle		ORS65	SYD100	SYD140
U Across-shelf (m s^{-1})	Mooring HSM	-0.017 -0.023	-0.036 -0.036	-0.043 -0.059
V Along shelf (m s^{-1})	Mooring HSM	-0.062 -0.117	-0.075 -0.129	-0.110 -0.133
Major axis orientation (º)	Mooring HSM	13.25 11.60	18.62 19.38	23.08 24.45
Minor axis orientation (º)	Mooring HSM	0.03 0.02	0.05 0.03	0.06 0.04

Bottom		ORS65	SYD100	SYD140
U Across-shelf (m s^{-1})	Mooring HSM	-0.016 -0.007	-0.000 -0.021	-0.017 -0.038
V Along shelf (m s^{-1})	Mooring H3SM	-0.036 -0.072	-0.029 -0.091	-0.060 -0.096
Major axis orientation (º)	Mooring HSM	21.00 16.62	19.98 17.55	28.24 24.71
Minor axis orientation (º)	Mooring HSM	0.02 0.02	0.04 0.02	0.05 0.03

Table 2.4. Mean depth-averaged current speeds for the across-shelf (U), and along-shelf (V) velocities and their associated axis orientations for variance ellipses: (top) upper - depth bin, (centre) mid - depth bin, (bottom) bottom - depth bin.

2.5.5 Surface Circulation Variability

To show that the Hawkesbury Shelf Model reproduces the dominant circulation patterns, geostrophic velocities derived from altimetry and the HSM were decomposed via empirical orthogonal function analysis (EOF, Fig. 2.17). Results revealed that the spatial structure of the mean geostrophic velocities and spatial modes were well captured by the HSM.

Between 32 - 33°S, velocities were strongly poleward, with a poleward maximum of -0.84 m s^{-1} (observations) and -0.90 m s^{-1} (HSM). Small directional differences could be seen south of 34°S, where the EAC has typically separated from the coast and eddies impact the shelf leading to a higher current variability. EOF modes 1-3 explained ~ 76% of the circulation variability in both the observed and modelled data.

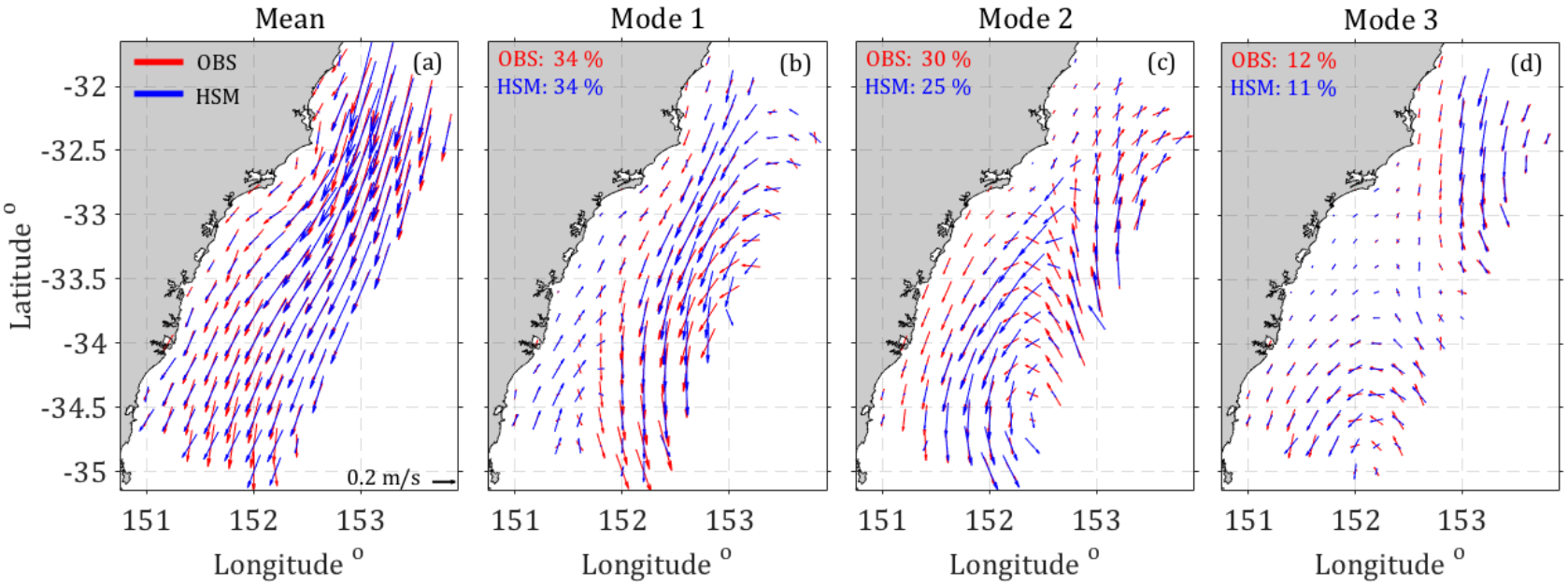

Fig. 2.17. EOF analysis of daily geostrophic velocities from the HSM (blue) and satellite (red) for 2012-2013. Spatial structure of the (a) Mean, (b) Mode 1, (c) Mode 2 (d) Mode 3 showing velocity fields (arrows). Percentages show the variances accounted for by the specific modes.

The first spatial mode showed all poleward flow and accounts for 34% of the variability in both the modelled and observed data sets (Figure 2.17a). The second mode depicted an eddy dipole which accounted between 25% (modelled) and 30% (observed) of the variability (Figure 2.17b).

The principal component timeseries and the model-data correlations were presented in Fig. 2.18. The correlations between the model and observations were strong. For modes 1, 2 and 3 respectively the expansion coefficients had correlations CC=0.69, CC=0.66 and CC=0.74. The sign of the timeseries oscillated between positive and negative ~ 50% of the time.

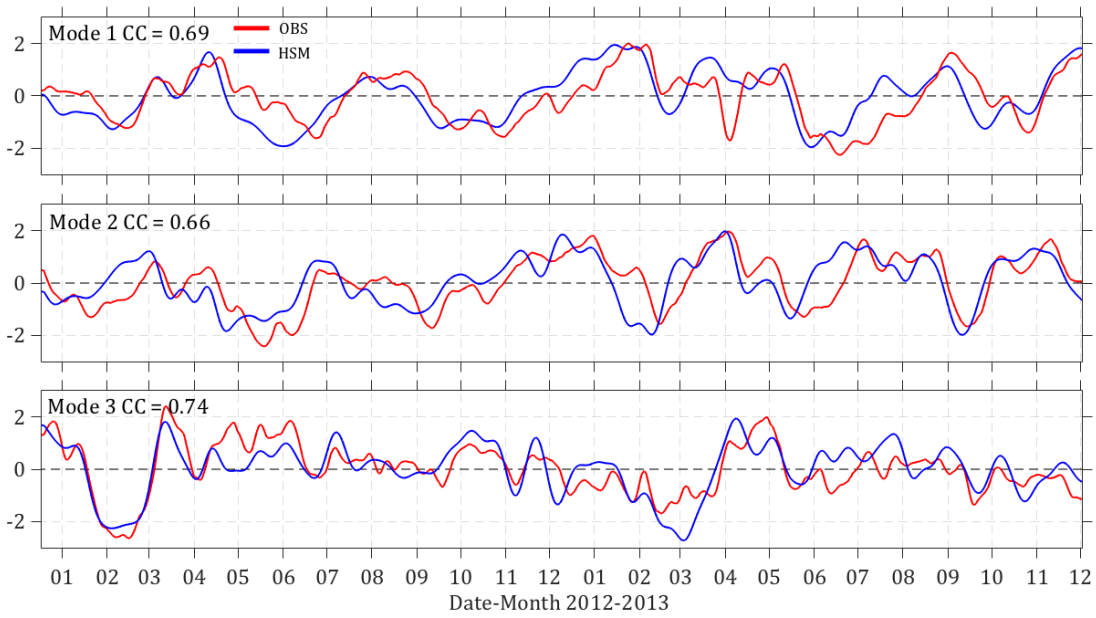

Fig. 2.18. The principal component time series (PC) for EOF modes 1, 2 and 3 from the HSM (blue) and observations (red), respectively. CC stands for the correlation coefficient between the HSM and observations. The correlation coefficients are above the 95% level of confidence.

Spectral analysis of the expansion coefficients for mode 1, 2 and 3 (Figure 2.19) highlighted the agreement between the model and observations in representing the spatial variability, with dominant peaks in the mesoscale frequency band between 93-124 days. These results showed that the dominant spatial patterns of the Hawkesbury Shelf region were overall well captured by the HSM (Fig. 2.19).

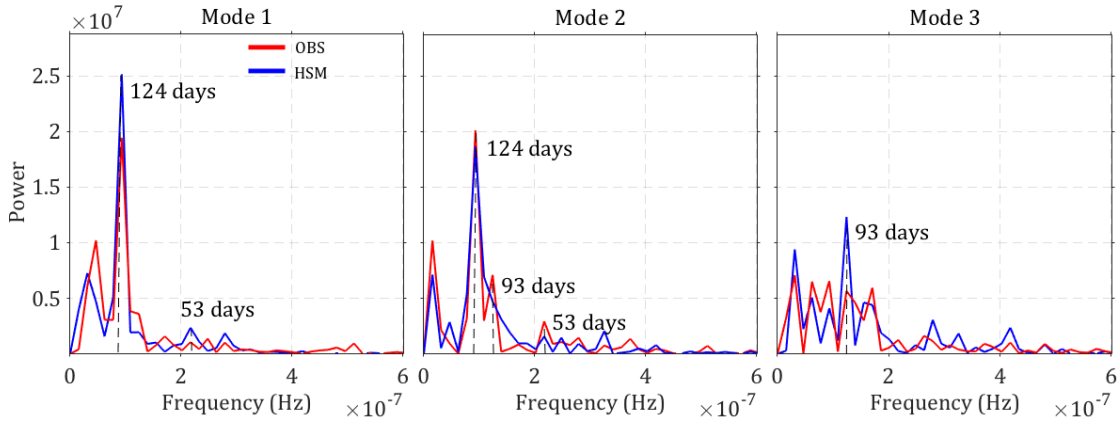

Fig. 2.19. Power spectra for the PC time series for EOF mode 1-3.

2.5.6 Energy Spectra

Rotary spectra were calculated at 39 m below the surface (Figure 2.20) and using the depth averaged velocities (Figure 2.21). Overall, energy spectra at all three mooring sites were dominated by the tidal and inertial frequency band (inertial frequency is 21.5 hours at latitude 33ºS, Fig. 2.20, 2.21). While the EAC model was not forced with tides, energies still indicated peaks at the diurnal and inertial frequency band. This can be the result of combined surface heat flux, sea breeze and inertial motions in the flow which possibly introduced extra energy at the diurnal-band. At 39 m below the surface, modelled velocity rotary spectra were underestimated in the diurnal and semidiurnal frequency band. In the semi-diurnal band, differences were largest at the inner shelf mooring ORS065 (Fig. 2.21). Energy spectra were lower at the inner (ORS065) than the outer shelf (SYD140) as a result of weaker stratification. For depth-averaged velocities, energies contained in the tidal bands were higher in near-shore regions and lower throughout the outer shelf regions.

Velocities at 39 m showed a counter-clockwise polarization while the depth-averaged velocities are polarized in the clockwise direction (Fig. 2.20, Fig. 2.21). This is due to changing flow directions with depth. The asymmetry between the clockwise and counter-clockwise energy distribution at 39 m and in the depth-averaged velocity field, could be related to sea-breeze forced diurnal motions as explained by Lerzak et

al., (2001). Overall, diurnal and semidiurnal processes across the shelf are consistent between observations and simulations, indicating that the HSM can reproduce internal processes within the diurnal and diurnal frequency bands.

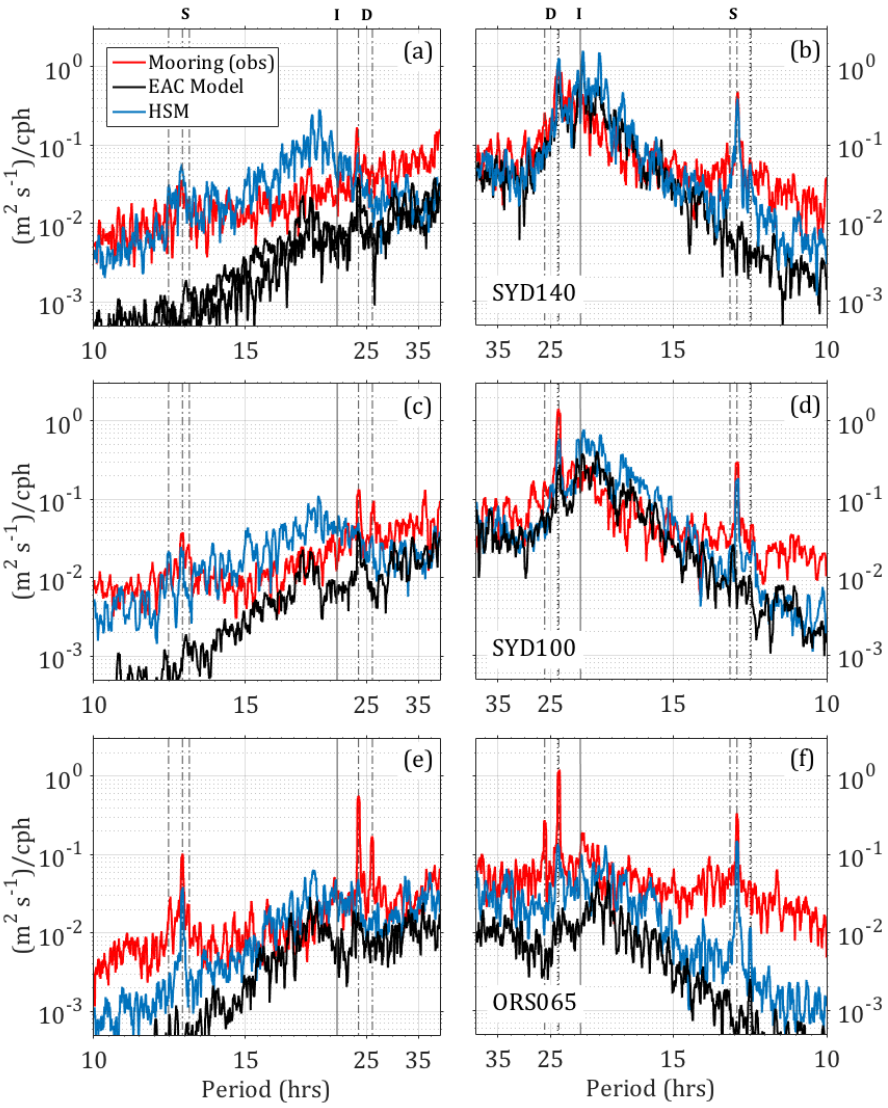

Fig. 2.20. Rotary spectra at 39 m below the surface (left panel: clockwise, right panel: counter clockwise) for simulated velocities: HSM (blue), EAC model (black), and observed velocities (red) at the 3 mooring stations. The dashed lines show tidal constituents in the diurnal (D) and semi-diurnal (S) band. The solid line indicates the inertial frequency (21.4 hrs, I).

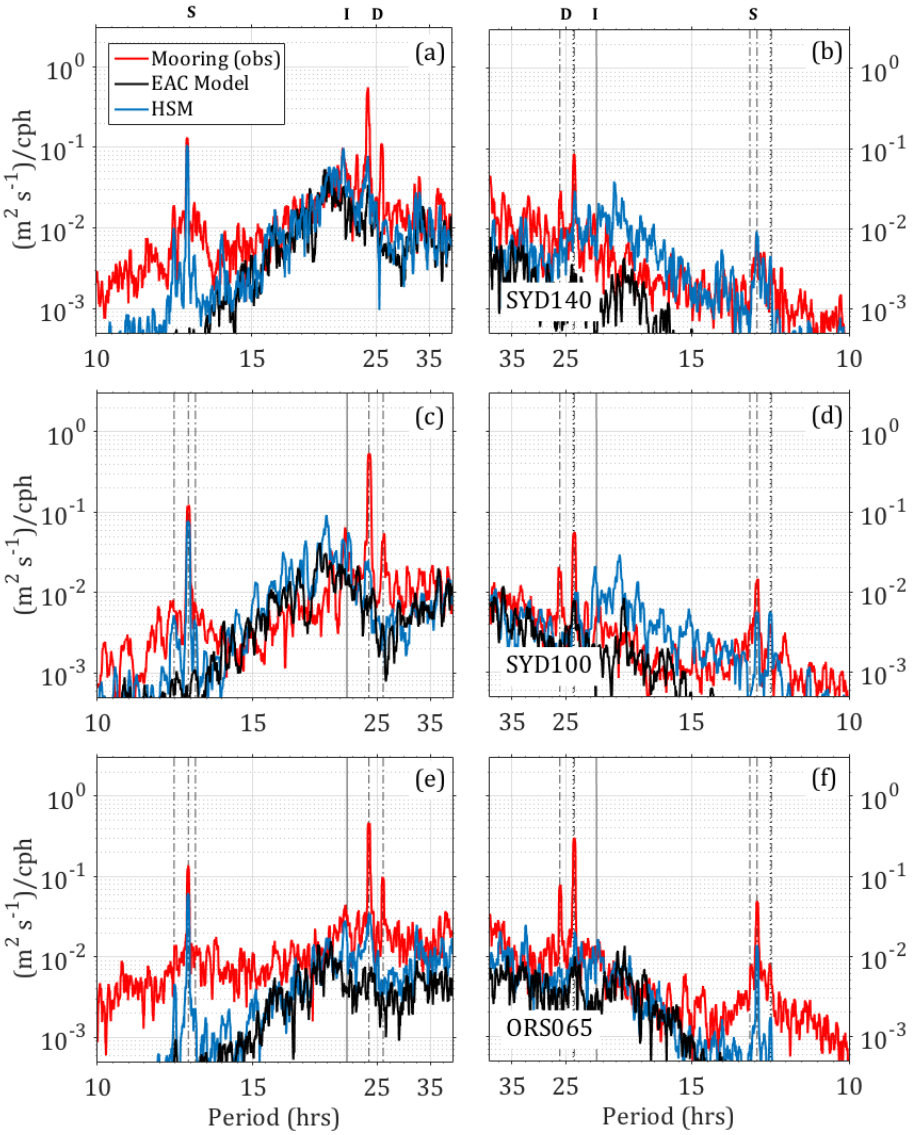

Fig. 2.21. Rotary spectra of depth-averaged velocities (left panel: clockwise, right panel: counter clockwise). HSM (blue), EAC model (black), and observed velocities (red) at the 3 mooring stations. The dashed lines show tidal constituents in the diurnal(D) and semi-diurnal (S) band. The solid line indicates the inertial frequency (21.4 hrs, I).

2.5.7 Wavenumber Spectra

The wavenumber spectrum of the upper 40 m of the ocean were shown in Fig 2.22. The steep inclination of the slopes revealed a partitioning of energies for both models between $50 < \lambda < 100$ km, and for $25 < \lambda < 50$ km.

For wavelengths between 25 and 50 km, the slopes for both models converged. Between 50 and 100 km, slopes followed a spectrum with $\sim k^{-5/3}$, but energies rapidly tailed off to smaller scale regimes, with a steep $\sim k^{-4}$ slope between 50 and 5 km. At wavelengths of less than 10 km for the EAC model and 2.5 km for the HSM, noise dominated the calculation resulting in a steepening of the slope. It is noteworthy to point out that the slope of the spectra did not vary significantly between the models. However, the HSM did exhibit larger energies for $\lambda < 25$ km.

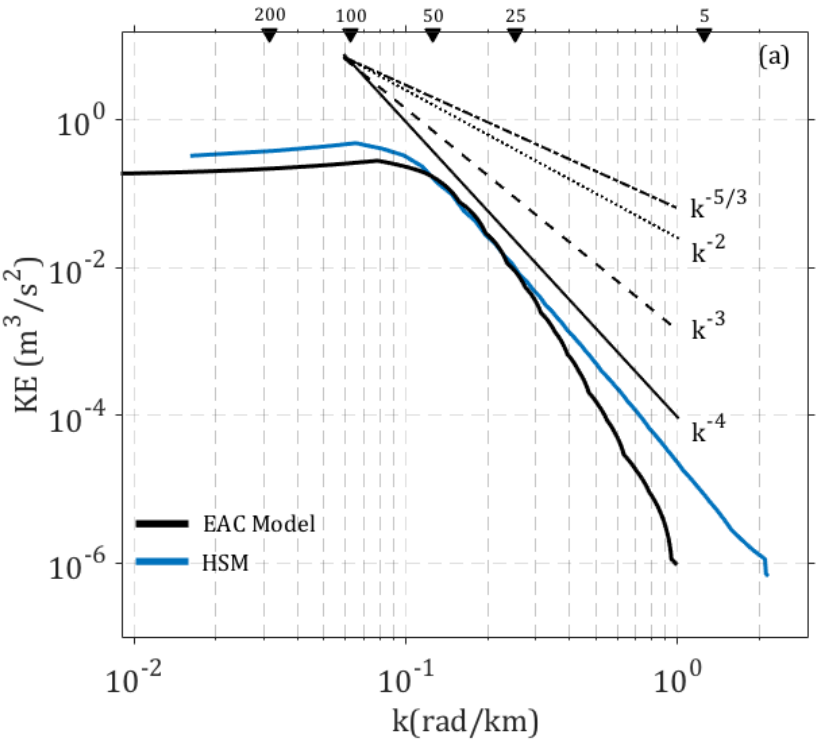

Fig. 2.22. Wavenumber spectra (EAC model (dx=2.5 km) and HSM (dx=0.75 km)) for horizontal surface velocities encompassing the HSM domain (Black triangles show the wavelength in km). Black lines indicate spectrum slopes.

2.5.8 Eddy-Mean Flow Interactions on the Shelf

2.5.8.1 Energy Reservoirs and Conversion Paths

Both models presented similar energy distributions throughout the domain. This further confirmed the successful mesoscale downscaling of the HSM (Fig. 2.23). Additionally, simulated mesoscale variability in both models displayed the same spatial structure, with lower (higher) values inside (outside) the 200 m isobath.

The horizontal distribution of EKE (energy reservoirs are defined in section 2.4.10) was spatially irregular in both models with patches of high EKE (>170 J $m^{-3)}$ outside the 200 m isobath. Overall, the HSM presented peaks with a 16% increase in EKE compared to the EAC model. Inside the shelf break, energies were significantly lower in both simulations, particularly in the along-shelf direction with 20-100 J m^{-3} in the north and 20 – 60 J m^{-3} in the south. Results also showed that in both simulations, EKE is generally higher than MKE. However, the region between 32 and 33°S, had MKE values twice as high as EKE. Mean potential (MPE) and eddy potential energy (EPE) had a different horizontal distribution then EKE and MKE. MPE had high values along the coast and low values in offshore regions outside the 200 m isobath. Differences were largest (typically 40%) south of 32°S (Fig. 2.23, g, h). At 32°S, the EAC model displayed an increase in MPE of 20% whereas the HSM had an increase only inside the 200 m isobath. The distribution of EPE revealed a significant positive area outside the 200 m isobath in both simulations (100 J m^{-3} along the coast, to 250 J m^{-3} offshore). This lead to the assumption that baroclinic instabilities in the offshore region produce an increase in EPE outside the 200 m isobath in both simulations.

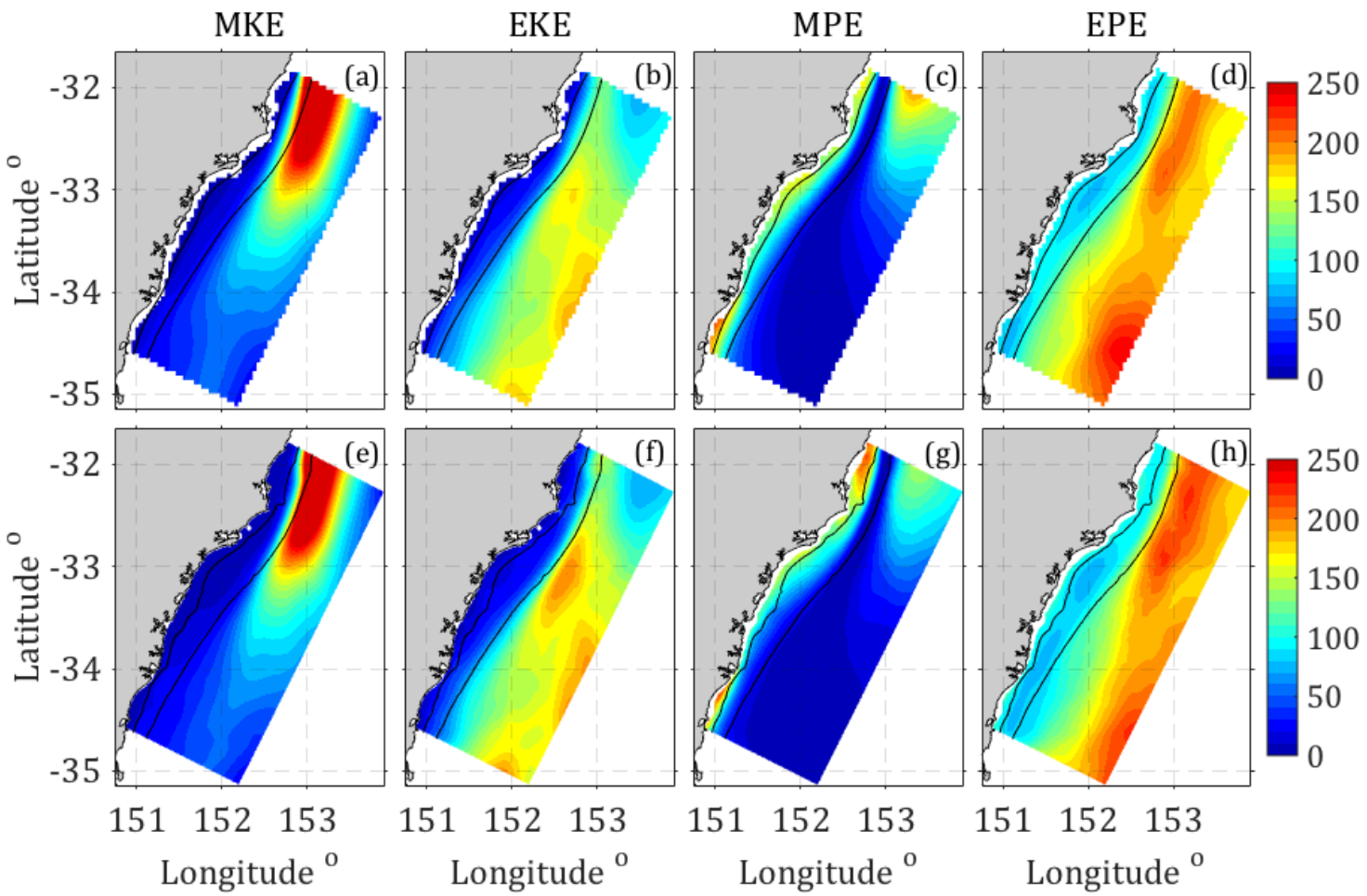

Fig. 2.23. Energy reservoirs for the upper 40m (J m $^{-3}$). The EAC model is shown in (a,b,c,d) and the HSM (e,f,g,h). Black lines show the 100 and 200 m isobath.

The energy ratio between the mean and fluctuating parts of the surface circulation (MKE: EKE) gave an estimate of the surface circulation steadiness. Values below 1 (MKE < EKE) indicated a strong variability of the currents; values larger than 1 (MKE > EKE) indicated a more stable mean current. This was shown for both models on the Hawkesbury Shelf (Fig. 2.23).

The MKE: EKE ratio elucidated a pattern that showed dominating EKE throughout the domain. Nevertheless, a clear dominance of MKE over EKE was found between 31.5 -33°S with values reaching up to 3.3 (EAC Model) and 2.94 (HSM). Below 33°S, the ratio became less than 1, indicating a dominating EKE over MKE.

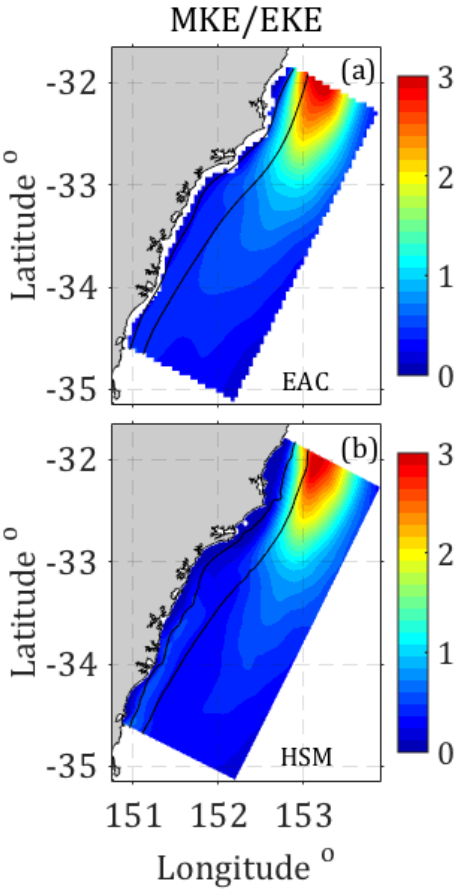

Fig. 2.24. Mean kinetic energy and eddy kinetic energy ratio for (a) the EAC model and (b) HSM. Black lines show the 100 and 200 m isobath.

The energy conversions between the major reservoirs were disclosed in Fig. 2.25. The barotropic conversion (MKE to EKE) showed an energy intense positive patch

situated offshore of the 200 m isobath, which extended throughout the domain from 31.5 - 34°S. Along the coast however, a slight negative barotropic conversion was confined by the 200 m isobaths.

The stripes in the HSM resulted from calculating the gradient calculations dvdy and dudx which introduce artefacts due to the high spatial resolution. However, even with the stripes included, the general pattern is similar to the EAC model which gives further reassurance in the validity of the results.

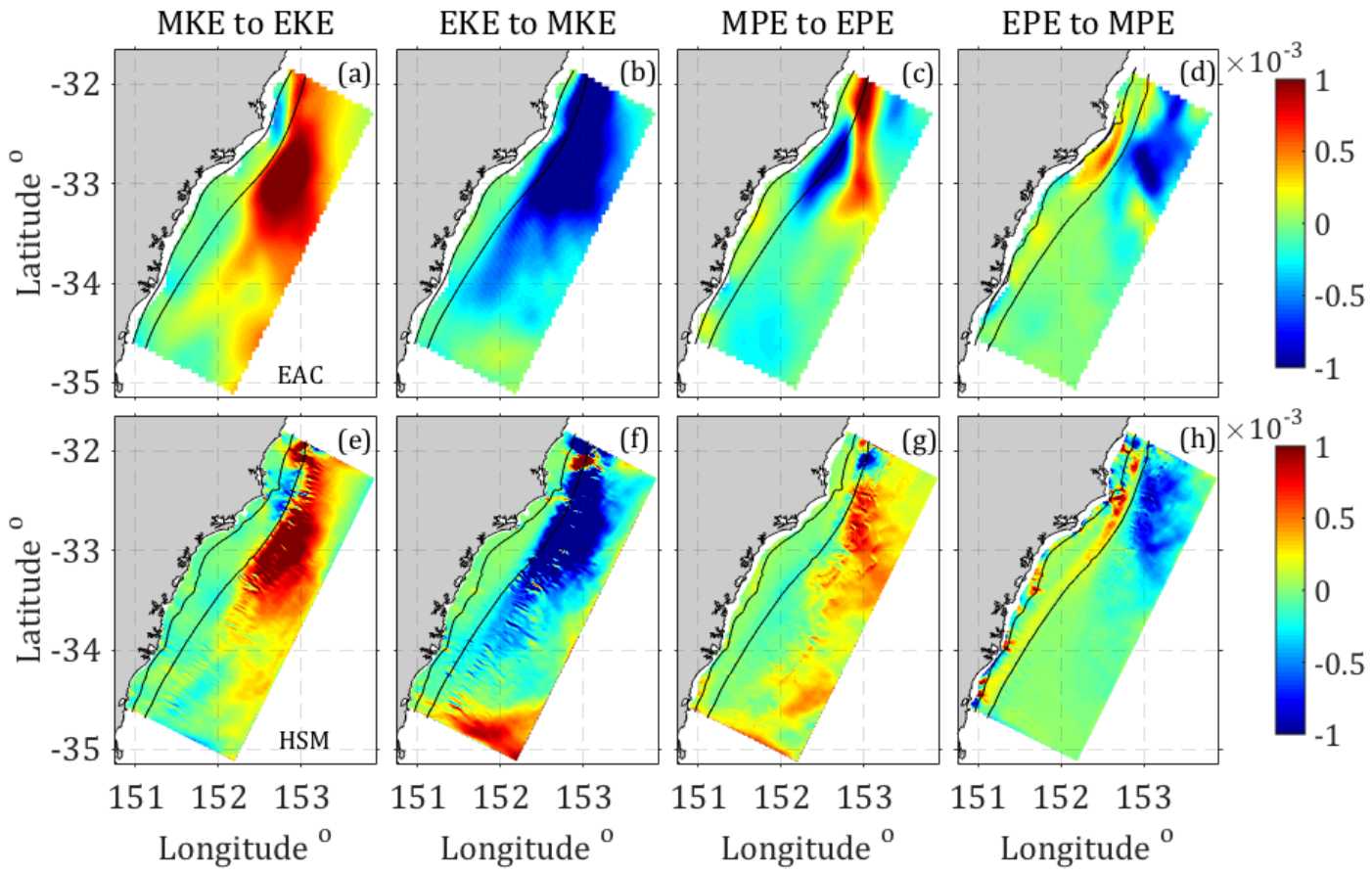

Fig. 2.25. Energy transfer rates (W m^{-3}) of the upper 40 m of the ocean. Upper row shows results from the EAC model (a-d), lower row shows the HSM (e-g).

2.5.8.2 Domain-averaged MKE and EKE

The temporal evolution of domain-averaged energy reservoirs (MKE and EKE) of the HSM is in good agreement with the EAC model (Fig. 2.26). Correlations for MKE and EKE were high with values of 0.97 for MKE and 0.91 for EKE.

Overall, MKE and EKE varied throughout simulation period (2012-2013), with lower values from February to April and June to August relative to the rest of the year. MKE rapidly increased until the end of April with a relative minimum in August. It is interesting to note that in both models a relative maximum of MKE appeared in Spring and Summer 2012/2013. Peaks occurred in February 2013 with an MKE of 350 J m^{-3}.

The MKE and EKE seasonal cycles had positive correlations (February peak for MKE as well as for EKE). Periods between June and July had large EKE peaks which were opposed with small MKE for both 2012 and 2013.

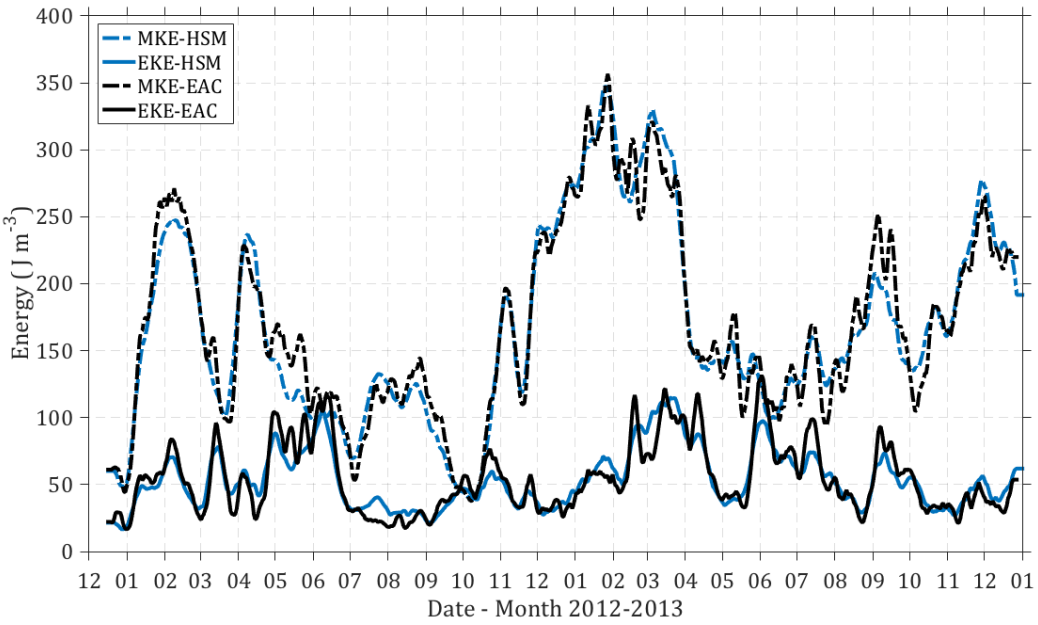

Fig. 2.26. Domain-averaged and daily mean simulated MKE (dashed lines) and EKE (solid lines) for the upper 40 m. $cc_{mke\ (EAC\text{-}HSM)}$ = 0.97; $cc_{eke\ (EAC\text{-}HSM)}$=0.91; cc is the correlation between the EAC model and HSM.

2.6 Discussion

2.6.1. SST Observations

The EAC and HSM qualitatively represent the mean spatial SST distribution and temporal variability within the EAC separation zone. The simulation of a band of colder temperatures found along the inner shelf has been previously observed as a result of the EAC encroachment onto the shelf, (Schaeffer and Roughan, 2015). The encroachment of eddies onto the shelf can lead to upwelling as result of intense bottom stress and carry colder water into shallow coastal areas (Oke and Middleton, 2000; Roughan and Middleton, 2002, 2004; Schaeffer et al., 2013).

A study by Ridgway et al. (1997) concluded that after the main jet of the EAC has detached from the coast, only about 1/3 of volume transport continues poleward, which leads to colder, more variable temperatures downstream of the EAC separation and along the coast. The higher variability in the satellite observations compared to the models is most likely a result of missing observation data in the model domain. This results in errors in the overall mean including a higher variability. Overall, the sea surface temperature (SST) is influenced by various processes, primarily by surface heat flux, vertical mixing and upper ocean processes (Marta-Almeida et al., 2013; Davis et al., 1981; Large et al. 1986; Alexander et al., 2000). Thus, the spatial distribution of SST and its variability serves as a good indication of the model's ability to reproduce the major circulation pattern. The outer EAC model provides the boundary conditions for the HSM model and thus, potentially restricting its performance by passing biases (deeper thermocline, stronger poleward flow and temperature bias) to the nested grid.

2.6.2. Barotropic Tides

The agreement between observed and modelled sea level time series highlights that the HSM reproduces the general barotropic tidal regime in the nearshore region, classified as predominantly semi-diurnal (Table 2.3, Fig. 2.12). The phase error detected within the diurnal tidal band, in particular the K1 constituent, may be the result of diurnal oscillations induced by land-sea breezes. As shown by Wood et al. (2016), land-sea breezes generated from warming and cooling of the land masses and sea, result in diurnal

peaks of the local wind stress spectra which may have a strong impact on diurnal variations (Guarnieri et al., 2013). It follows that errors in the resolution of the diurnal constituents reveal the inability of the model to produce the wind-related processes in the diurnal energy band, such as the sea-breeze cycle, impacting tidal phases and amplitudes (Guarnieri et al., 2013).

In addition, the rotary power spectra of near surface and depth-averaged current data also shows that the majority of energy lies within the diurnal frequency band. Velocities reveal a flow polarization with counter-clockwise motions, indicating the signature of anti-cyclonic motions on the shelf and implying the propagation of warm core eddies on the shelf.

The coarse parent EAC model, which is not forced with tides also exhibits energies in the diurnal and inertial frequency (21.5 hrs) band. This leads to the assumption that extra energy at the diurnal and inertial band is introduced through surface heat flux and inertial motions within the flow.

2.6.3. Circulation Variability

Dominant modes of variability found in the surface geostrophic current field of the HSM compare well with observations with the majority of the mesoscale variability can be accounted for by EOF modes 1-3. It is therefore concluded that the HSM correctly reproduces the dynamical features of mesoscale variability in this dynamic region. Between 32 - 35 ^{o}S the mean geostrophic currents are dominated by a poleward flowing EAC. In agreement with previous modelling studies by Oke and Middelton (2000) and Roughan et al. (2003) maximum velocities follow regions where the EAC is most coherent (from 32 - 33^{o}S), before its separation from the coast. In addition, model results reveal a poleward directed flow along isobaths, in accordance with findings by Schaeffer et al. (2015) who investigated the mean geostrophic circulation and variability inside the 200 m isobath using glider deployments.

Overall, the modelled mean geostrophic current field confirms the dominance of the EAC on the circulation variability of the Hawkesbury Shelf.

2.6.4. Energy Pathways on the Shelf

The kinetic energy spectra of both models approximately follow a $\sim k^{-5/3}$ spectrum for $50 < \lambda < 100$ km. For $\lambda > 50$ km (about 2.5 times the local Rossby Radius for the modelling domain (~19 km)), energy is transferred from smaller to larger scales in accordance with the geostrophic turbulence theory (Vallis, 2006); Ferrari and Wunsch (2009). For wavenumbers between $25 < \lambda < 50$ km, the slopes converge and rapidly steepen to follow a k^{-4} spectrum. This convergence is most likely is the result of the EAC dominated large-scale variability impacting on both modelling systems (EAC model and HSM). For wavenumbers with $\lambda < 25$ km, the HSM continues to follow the k^{-4} spectrum while the EAC model steepens beyond the k^{-4} spectrum. Higher kinetic energy values of the HSM, indicated by a flatter slope between $5 < \lambda < 25$ km relative to the EAC model, show that the HSM is generally more energetic than the larger-scale EAC model. This result is anticipated for the small scales because the HSM has a higher grid resolution than the EAC model. Capet et al. (2008) investigated the energy cascades from mesoscale to submesoscale in the wavenumber range for the California Current System utilizing a suite of simulations with horizontal grid resolutions ranging from 12.5 to 0.75 km. Similar results were observed in the KE spectra with higher energies associated with finer grid resolutions (flatter slope in the finer grid compared to steeper slopes in coarse grid resolutions).

In addition, Capet at al. (2008) highlights that in the submesoscale range, where ageostrophic dynamics are dominant, energy is transferred from larger to smaller scales (forward cascade) with continuing dissipation at even smaller scales. The slopes associated with forward cascade approximately follow a k^{-3} (Capet et al., 2008). The steep slope of k^{-4} as explained by LaCasce et al. (2010) is associated with linear dissipation acting on all scales, instead of only at larger scales, as argued for in the two-dimensional theory. Furthermore, LaCasce (2010) showed, when the linear dissipation only acted on larger scales, the spectral slope would be closer to -3, as expected. This suggests that in this case, linear dissipation or Rayleigh damping (possibly due to bottom friction) is dissipating the energy at all wavenumbers.

The upper ocean energy pathways between the main reservoirs MKE and EKE reveal that the EAC separation zone is an area dominated by barotropic instabilities. Particularly between 32 and 33.5°S, where strong along-shelf flows lead to horizontal

shears and favour barotropic instabilities. This is in agreement with Stammer et al. (1997), who argued that the mesoscale eddy activity in the EAC between 32 -35ºS is more barotropic in nature.

In both simulations, energies are lower inside the 200 m isobath relative to offshore regions, particularly for MKE and EKE. Although in this study local wind regimes are not further investigated, previous studies found that due to the interaction of surface and boundary layers on the inner shelf, wind stress can induce large horizontal shears, and thus impacting on local flow instabilities (Kang and Curchitser, 2015). Furthermore, positive values of both the barotropic and baroclinic conversion terms, indicate that the eddies draw energy from the mean flow, ultimately deaccelerating the mean flow (Zhan et al, 2006).

The dominance of MKE over EKE has been reported by previous studies (Sloyan et al., 2016), particularly upstream at 27ºS, where the EAC is most coherent and due to the location of the EAC, increasing the MKE over EKE. This result could be induced by the meandering of the EAC on and off the shelf as well as its equatorward recirculation (Sloyan et al., 2016). High EKE values found in the simulations agree with previous studies of the EAC. Bowen at al. (2005), found higher EKE values between 32 and 35ºS due to intrinsic instabilities of the current, which are initialized by the bifurcation of the EAC from the coast and into the Tasman Sea. In addition, Nilson and Creswell (1998) argue that the higher eddy activity below 32ºS is the result of the recirculation of the EAC and interaction with the shelf. Marchesiello and Middleton (2000) also conclude that this process plays a key role in eddy shedding simulated by models which are focused on the separation region.

Overall, higher MKE and EKE peaks are found in the HSM offshore of the 200 m isobath. These peaks are most likely the result from larger mean flow instabilities caused by the finer resolution of the shelf.

2.6.5. Impacts of Nesting

Even though data assimilating models offer an advanced and realistic tool to improve accuracy of predictions, hindcasts of oceanic currents and hydrographic conditions, observations needed to constrain submesoscale model circulation like altimetry currently do not resolve these scales. Thus, the circulation resolved by the HSM

would not be effectively constrained by data assimilation and is therefore not appropriate for this study.

For that reason, high-resolution free running models can be downscaled from coarser data assimilated models to ensure the use of the best possible boundary conditions. However, an increase in resolution does not necessarily improve the model's performance. For example, incoherencies can appear because the lateral open – sea boundary conditions are obtained by interpolating the coarse resolution model outputs (Auclair et al., 2001; Vandenbulcke et al., 2006; Bricheno et al., 2013). In addition, the nested grid model can contain small-scale processes that are unable to propagate out of the domain generating spurious elements (Barth et al., 2008).

The model comparisons show a successful nesting and highlight the HSM's ability to capture the coastal circulation and its variability. The model's tendency to overestimate the mean currents by ~10% on the shelf, suggests that the strong poleward flowing and meandering EAC impinges further onto the shelf in the model than seen in observations. Few studies have considered the effects of vertical resolution on nested grids; however, Zhang et al. (2011) finds that solving boundary layer dynamics and capturing stratification is key to model the mean circulation across the New England Shelf; this in turn is achieved by using an increased number of vertical layers.

The HSM shows a temperature bias which is stronger in the southern part of the domain, an area where the EAC impact is less (Fig 2.11). The temperature bias in the HSM is overall greater than the bias seen in the EAC (data assimilating model) which only shows a small bias by the coast. By using 4-D VAR data assimilation, biases in the atmospheric heat fluxes are reduced in the EAC model, leading to lower errors in SST.

The temperature bias is also addressed in Kerry et al. (2016) who describe the configuration of the EAC model. Temperatures in the free run (a two-year EAC model run without assimilation) are compared to observations and a bias of up to 0.7^{o}C in the upper 100 m of the water column prior to data assimilation was identified. Furthermore, after data assimilation, Kerry et al., (2016) show a small net bias over the 2012–2013 period (0.28). The temperature bias observed in the assimilation and free running model reveals that atmospheric forcing (ACCESS) leads to a significant temperature increase in the upper 250 m of the water column.

The HSM is nested inside the assimilating EAC model and forced towards the EAC model daily at the boundaries with no relaxation to the observed SST. Due to the fact that it is run as a free running model, it is unable to correct the bias introduced by the

atmospheric forcing.

This means, when using the same atmospheric forcing (ACCESS), the surface flux is not corrected and impacts the surface temperature and stratification in the HSM. Consequently, a larger temperature bias is observed (Fig. 2.11), which extends throughout the water column on the shelf (when compared to mooring observations in Fig. 2.13).

2.7 Summary

In this chapter, a 750 m high-resolution numerical model that captures both the mesoscale circulation offshore and the circulation across the continental shelf has been configured and validated for the Hawkesbury Shelf (2012-2013). Comparisons of modelled and observed statistical patterns confirm that the HSM reproduces the dominant dynamical features of the mesoscale and coastal variability off Sydney (34^{o}S). The spatial distribution of barotropic energy transfers reveal higher energies along the path of the EAC separation, where strong along-shelf velocities induce large horizontal shears. The kinetic energy spectra of the HSM is partitioned into two main regimes. While large scale regimes are agreement with the SQG theory (Blumen, 1978), energies rapidly tail off to smaller scaler regimes, indicating that on smaller wavenumbers, friction is dominating. Compared to the EAC model, the HSM contains energies that are larger in the smaller wavenumber range, highlighting the impact of the resolution downscaling on model energetics.

Overall, the performance of the 750 m high-resolution model is sufficient for further investigations of shelf dynamics including the mean circulation, variability and exchange processes with the open ocean.

In the upcoming chapters 3 and 4 of this thesis, the HSM outputs are used respectively to

1) Investigate the mean circulation and its variability across the Hawkesbury shelf, and to depict its major sites for ocean-shelf exchange.

2) Understand the impact of the shelf circulation on the coastal ecosystem by identifying water sources on the inner shelf and over an offshore artificial reef located off Sydney.

Chapter 3

The mean circulation, variability and transport regimes of the Hawkesbury Shelf (31.5-34.5ºS)

3.1 Introduction

Exchange processes responsible for transporting water masses across and along the shelf-slope boundary are controlled by mesoscale circulation features such as eddies, fronts and current meanders. This is particularly true for regions adjacent to dynamic western boundary currents, such as the east coast of Australia, where warm (anti-cyclonic) and cold core (cyclonic) eddies are periodically shed from the current every 90-110 days (Oke and Middleton, 2000; Bowen et al., 2005; Cetina-Heredia et al., 2014).

The encroachment of eddies on the shelf can lead to upwelling as result of intense bottom stress that drives cold, dense water upward into the shallow depths of the euphotic zone (Oke and Middleton, 2000; Roughan and Middleton, 2002, 2004; Schaeffer et al., 2013). In the along-shelf direction, water is mainly transported along dominant shelf flows advecting biota and other tracers (Schaeffer et al., 2013). Thus, transport processes are a key factor in the distribution of important oceanic properties such as heat and nutrients, impacting the productivity of coastal ecosystems (Falkowski et al., 1988; Roughgarden et al., 1988; Austin, 1999).

Along southeast Australia the circulation is largely dominated the poleward flowing EAC and its separation from the coast. Typically, the EAC separates between 30.7 - 32.4ºS, although it has been observed to separate anywhere between 28 - 38ºS (Cetina-Heredia et al., 2014). The volume transport of the EAC in the along-shelf

direction has previously been studied using deep water mooring arrays as well numerical models. Mata et al. (2000) estimated the mean volume transport from a mooring array upstream of the separation at 30ºS with 22.1 Sv over a 4-year period. A more recent study by Kerry et al. (2016) confirms the strongly poleward along-shelf transport upstream at Coffs Harbour (30.3ºS) with a low variability and a magnitude of 21.9 Sv. However there have been no studies investigating shelf transport and onshore / offshore export.

In addition to the varying circulation up and downstream of the EAC separation zone, previous studies highlight that the strength of the EAC also varies throughout the year, with poleward surface currents about twice as strong in austral summer than in winter (Hamon et al., 1975; Ridgway and Godfrey, 1997; Godfrey et al., 1980).

The shelf circulation, however, seems to remain fairly unaffected by the seasonal variability of the EAC. A long-term study conducted by Wood et al. (2016), revealed that the circulation variability inside the shelf break is less affected by EAC's seasonal variability contributing only 6% to the overall variability. This raises an important question on the profound impact of the EAC variability on different regions of the shelf.

It is well known that inner shelf regimes are often isolated from offshore variability due to a combination of factors. On the mid and outer shelf, larger depths separate the surface and bottom boundary layers, favouring cross-shelf exchanges with the open ocean and adjacent mesoscale circulation features, such as eddies and current meanders. Cross-shelf exchanges are therefore dependent on the location of such features with respect to the shelf and the frequency at which they interact with the shelf. This ultimately results in variable cross-shelf velocities along the continental shelf, often an order of magnitude smaller than its along-shelf counterpart. These exchanges can be current, or wind driven in nature. According to the classic Ekman theory (1905), cross-shelf exchanges on the mid and outer shelf are largely driven by along-shelf wind stresses.

On the inner shelf however, where depths are much shallower, the water column is well mixed because the surface and bottom boundary layers overlap. As a consequence, the along-shelf wind stresses become negligible as a driving force of cross-shelf exchange. Ekamn (1905); Austin and Lentz (2002) and Lentz and Fewings (2012) show that the momentum induced by along-shelf wind stresses mixes the water column before the Coriolis acceleration can be effective. This has the potential to inhibit the cross-shelf exchange and thus isolate he inner shelf from offshore variability.

The EAC's large scale transport has been quantified and well documented in the literature through both observation and modelling studies. However, the bulk of this

transport is contained in waters adjacent to the shelf, in depths exceeding 2000 m. The high spatial and temporal variability of cross-shelf exchange makes quantifying the shelf transport a challenging task (Csanady, 1997). The lack of spatial resolution has also inhibited the investigation of variations in transport across different shelf sections (*i.e.* the inner shelf, middle and outer shelf); in particular for the quantification of cross-shelf transport.

As a result, transport estimates for the narrow continental shelf off southeast Australia, encompassing the Hawkesbury region, are to date not available. This chapter focuses on quantifying the across and along-shelf transport, for the first time comprehensively in space (over the shelf), and time (over two-years with 2-hourly outputs), to identify regions of shelf-exchange with implications for upwelling and productivity. In addition, the surface circulation variability is decomposed into its dominant modes. The impact of each mode on the transport budget is examined. This will further aid in obtaining a complete 3D picture of the mean circulation and variability on the shelf.

To overcome limitations of sparse observations, outputs from a regional 750 m shelf model (Hawkesbury Shelf Model, HSM), are used to investigate the transport regimes on the Hawkesbury Shelf.

3.2 Aims and Objective

The overarching aim of this chapter is to characterize the cross and along-shelf transport on the Hawkesbury Shelf; specifically, to identify the major regions for shelf water import and export. The transport variability is further detailed between the inner (<100 m), middle (<200 m), and outer shelf (2000 m), and results are discussed in the light of the forcings driving the local dynamics. The study domain is partitioned meridionally focusing on 3 main transects along the shelf.

The specific aims are:

1. Characterize the mean and seasonal 3D circulation on the Hawkesbury Shelf for 2012-2013 and its variability.

2. Evaluate the transport variability on the shelf (in the along and cross-shelf direction), specifically to determine the major regions for shelf water import and export.

3. Determine the two-year mean and seasonal shelf transport budget.

This chapter is organized as follows: The methodology used throughout the chapter is described in section 3.3. Section 3.4.1-3.4.2 presents the mean surface and depth-averaged flow and its effect on mean temperature. 3.4.3 highlight the circulation variability of the surface and with depth and. In sections 3.4.4-3.4.5 the mean along and cross-shelf transports across the 100, 200 and 2000 m isobath are described along with the volume transport budget of the. In the discussion section 3.5, mechanisms responsible for the mean circulation, temperature fields, and transport regimes are explained/proposed along with broader implications of the findings. Finally, the main findings are summarized in section 3.6.

3.3 Methods

3.3.1 Mean and Variability

3.3.1.1 Mean

Two-year means were calculated by time averaging each variable (u, v, temperature) over the simulation period from 2012 to 2013. Surface fields were based on the surface sigma layer; cross-sectional transects extending from the coast out to the 2000 m isobaths were chosen off Seal Rocks (32.2^{o}S, Newcastle(32.9^{o}S) and Sydney (33.9^{o}S) denoted as S1, S2 and S3 (Fig. 3.1). Velocities were rotated into along and across-shelf components.

Additionally, domain-averaged means were calculated by averaging the HSMs model area; results are illustrated as time series separately for the mean of 2012, 2013 and a total mean over the two-year simulation period.

Composite seasonal means for the surface ocean were calculated for u,v, and temperature by time averaging each variable over the following time periods (according to austral season):

1) Summer: 1 Jan 2012 to 29 Feb 2012; 1 Dec 2012 to 29 Feb 2013;
   1 Dec 2013 to 31 Dec 2013
2) Autumn: 1 Mar 2012 to 31 May 2012 and 1 Mar 2013 to 31 May 2013
3) Winter: 1 June 2012 to 31 Aug 2012 and 1 June 2013 to 31 Aug 2013
4) Spring: 1 Sep 2012 to 30 Nov 2012 and 1 Sep 2013 to 30 Nov 2013

3.3.2 Spatial Variability of the Surface Circulation

To investigate and depict the dominant spatial patterns of the surface circulation variability which are responsible for the transport pathways on the Hawkesbury Shelf, an empirical orthogonal function analysis of the surface circulation field (u,v) was used following the approach for the EOF analysis as discussed in Chapter 2. The major difference that sets the two analyses apart is the higher horizontal resolution. In this chapter, outputs at each grid cell with a horizontal spacing of 0.75 km were used; whereas in Chapter 2, surface geostrophic currents had been interpolated onto observational space with horizontal spacing of 2.5 km. Here, daily surface current velocity fields for 2012 and 2013 were used. The circulation variability of the surface ocean was decomposed into its dominant modes of variability using the singular value decomposition method by Björnsson and Venegas (1997). The mean has been removed prior to analysis and each mode represents a percentile of the total variability of the system.

3.3.3 Variability of the Along-Shelf Circulation on the Shelf

The along-shelf circulation on the Hawkesbury Shelf and its relation to the EAC mesoscale variability has been investigated. An empirical orthogonal function analysis (EOF) was applied to the 3D along-shelf current fields at transects perpendicular to the

coastline off Seal Rocks (S1), Newcastle (S2) and Sydney (S3). Simulated 3D daily velocity fields were rotated to match the shore normal orientation of each section.

The transects start at the coast and extend across the domain. Since the model is based on a terrain-following coordinate system, the uneven vertical distribution of grid points has to be compensated, to assure that spatial patterns are invariant to the vertical distribution of sigma coordinates (Baldwin et al., 2009). This was accomplished by applying a weighting matrix to each transect of velocity fields before conducting the EOFs. In addition, a spectral analysis of the principal component obtained with the EOF analysis was performed to identify the periodicities dominating the 3D along-shelf circulation.

3.3.4 Transport Calculation Method

3.3.4.1 Cross and Along shelf Transport

The along-shelf transport of the EAC has been the focus of various modelling and observational studies, however, their lack in spatial and temporal resolution inhibited the assessment of cross-shelf exchanges. It follows that despite the significance of cross-shelf transport and its implications for productivity, the impact of the EAC on cross-shelf transport is to date, not documented in the literature

In this study, 2-hourly outputs from the HSM were used to determine variations of across and along-shelf volume transports in the along-shelf direction on the Hawkesbury shelf for 2012 and 2013.

To compute the along-shelf transport, the shelf transects off Seal Rocks, Newcastle and Sydney (S1, S2, S3) were broken down into 3 main segments representing the inner shelf (0 - 100 m), the middle shelf (100 - 200 m) and the outer shelf region (200 - 2000 m) as seen in Fig. 3.12, left panel; all transects are normal to the shore.

For the cross-shelf transport, three isobaths were designated to compute the transport across the inner (100 m isobaths), middle (200 m isobaths) and outer shelf (2000 m isobaths). To determine the variability of the cross-shelf transport throughout the shelf, the isobaths were split into three equal latitudinal segments of approximately 119 km spanning the model domain of 357 km (Fig. 3.13., left panel). From north to south the segments for the cross-shelf transport are denominated xS1, xS2 and xS3, and correspond

to the region off Seal Rocks, Newcastle and Sydney respectively. This analysis highlights the major regions of shelf water import and export along the Hawkesbury Shelf.

However, the along and cross-shelf distances and corresponding subsurface areas of the shelf sections vary with the shelf width, impacting the volume transport. Width and length of each along and across-shelf segment is shown in Table 3.1. Segments used for the cross-shelf transport calculations follow the direction of the isobath closely, even though bathymetric meanders smaller than the grid resolution (750 m) have not been accounted for in the estimates.

Shelf Sections (m)	**S1** Width (km) / Area (km2)	**S2** Width (km) / Area (km2)	**S3** Width (km) / Area (km2)
0 - 100	9.1 / 670	13.4 / 837	8.9 / 668.4
100 - 200	22.2 / 3070	42.1 / 6522	19 / 3151
200 - 2000	16.6 / 18397	25 / 29155	27 / 28619
0 - 2000	48 / 22137	81 / 36514	55 / 32438.4

Table 3.1. Width (km) and area (km ^{2}) of the shelf sections at S1 (Seal Rocks), Newcastle (S2) and Sydney (S3).

The normal components of velocity v_n were used to compute the depth integrated across (a) and along (b) shore transports through the segments as follows:

$$(a) \quad V_{ny\pm} = \int_{-H}^{0} \int_{y_0}^{y_i} v_n dz\, dy \;;$$

$$(b) \quad V_{nx\pm} = \int_{-H}^{0} \int_{x_0}^{x_i} v_n dz\, dx \;;$$

subscript + (-) denotes the offshore (onshore) transport for the cross-shore component (V_{ny}), and equatorward (poleward) transport for the alongshore component (V_{nx}).
H represents the water depth. Since daily velocity fields have been used, the free surface height was neglected. The two-year mean transports and their associated standard deviations were calculated for 2012-2013.

3.3.5 Correlations

Correlation analysis was performed on both the along-shelf and cross-shelf transport time series, specifically to

i) Understand the relationship between different shelf sections (*i.e.* to determine if the inner shelf is correlated with the middle or outer shelf, across each transect at S1, S2, S3).
ii) Understand if the shelf sections are correlated along the coast (*i.e.* to determine if the inner shelf is correlated all along the coast at S1, S2 and S3).

To depict dominant periodicities for along and cross-shelf transport at each transects, wavelet power spectrums were calculated for the daily along and cross-shelf transport time-series using the wavelet analysis based on the Matlab scripts distributed by Torrence and Compo (1998) and the bias correction by Liu et al. (2007).

The correlation coefficient (CORR) or the covariance between different shelf transects was formulated here as follows:

$$CORR = \frac{1}{n-1}\sum_{i=1}^{n}\left(\frac{(ts1_i - \widehat{ts1})(ts2_i - \widehat{ts2})}{\sigma_{ts1}\sigma_{ts2}}\right);$$

with n representing the number of days, $ts1$ being the first transport transect and $ts2$ being second transect, σ being the standard deviation of ts1 and ts2, respectively. The $\wedge$ stands for the two-year mean of the time series of the variable it appears over.

This analysis will reveal the relationship between the different shelf regions and expose different transport regimes that may be present throughout the shelf.

3.3.6 Budget

For the purpose of considering the mean transport budget of the shelf, an enclosed shelf was defined by 3 (north to south) boxes delimited by the coast and the outer edge of the shelf (*i.e.* the 2000 m isobath, Fig. 3.16, left panel). The mean depth-averaged

transport was calculated across each side of the box, with exception of the western side, representing the coastal boundary. Note that the net transport out or into the box cannot sum up to zero since the varying free surface has not been taken into account.

Box A (referred to as Seal Rocks Box) is restricted to the north by the northern boundary of the HSM domain; this box corresponds to a segment that extends from 32.06 to 33.02ºS, covering a distance of 119 km in the latitudinal direction. In the horizontal, box A extends out to 153.43ºE, intended to follow the outer edge of the shelf (*i.e.* the 2000 m isobaths). However, to obtain a more accurate estimate of the budget, calculations were performed along the grid cell boundaries. The meandering nature of the 2000 m isobath leads to deviations from the 2000 isobath into deeper waters throughout the domain (down to 4100 m, Fig. 3.16, left panel).

Box B (Newcastle Box) is positioned between 33.02 and 33.85ºS covering 104 km in the latitudinal direction and extends out to 152.86ºS.

The most southern and largest box, encompassing Sydney is Box C. It extends horizontally out to 152.35ºE and latitudinally from 33.86ºS down to the southern boundary of the HSM domain at 34.93ºS, covering 134.25 km in the latitudinal direction. The transport budget analysis sheds light on the variability of shelf import and export regions with varying circulation patterns. To obtain the budget over the entire two-year simulation period, the mean transport in and out of the boxes was calculated.

Moreover, to investigate the impact of each dominant mode of variability on the shelves transport budget (modes were previously extracted from the surface circulation (see Section 3.3.2)); budgets were calculated separately for time periods when EOF modes (1-3) dominated. The period over which each EOF mode dominates was identified using their principal component time series (PC, from Dec 2011 – Dec 2013). Composites where then constructed for each mode using the times when the absolute amplitude of each mode dominated.

Finally, to test if regions of maximum transport relate or are influenced by the EAC separation throughout the HSM domain, the latitudinal range of the EAC separation from the coast was identified adapting the approach described in Cetina-Heredia et al. (2014).

The first step included the identification of the Sea Surface Height (SSH) isoline that corresponds to the maximum poleward surface velocity across a latitudinal section at 31.5ºS. The second step consisted of following the isoline in the poleward direction and identifying the latitude at which it meanders offshore (more than 70 km from the

coast). The resultant latitude was then documented as the separation latitude. This method was applied to daily-averaged velocity outputs for the two-year simulation period.

3.4 Results

3.4.1 Surface Temperature and Current Fields

3.4.1.1 Mean

The spatial structure of the mean surface velocities concurred with the two-year mean of geostrophic velocities shown in Chapter 2. Strong poleward flows were observed between 32 - 33.5°S with maximum velocities of -0.91 m s^{-1}. The same region showed highest mean surface temperatures between 22.54 and 23.4°C (Fig. 3.1, right panel and Fig. 3.2, right panel). The flow between the coast and the 200 m isobath closely followed the isobaths, with maximum poleward velocities of -0.42 m s^{-1}. Outside the 200 m isobath velocities were up to ~50 % stronger in magnitude. The largest standard deviations of the velocity field were adjacent to the shelf-break boundary at the 200 m isobaths (Fig. 3.1). South of 34°S, velocities started to decrease in magnitude with temperatures declining to 21.5°C (Fig.3.2). Throughout the entire modelling domain from north to south, the inner to mid-shelf region (from the coast out to the shelf-break boundary) exhibited an overall weaker, less variable flow field than that found throughout the outer shelf. Within the inner and middle shelf mean velocities ranged between -0.1 and -0.2 m s^{-1}, while in the outer shelf they reach -0.91 m s^{-1}.

The depth-averaged flow showed similar structure to the surface having maximum velocities of -0.5 m s^{-1} between 32 to 33.5°S. However, the highest variability was constrained to the shelf-break along the 200 m isobaths; whereas that for the surface currents exhibited relatively high variability along the path of the EAC without being constrained to the 200 m isobath (Fig. 3.1, right panel).

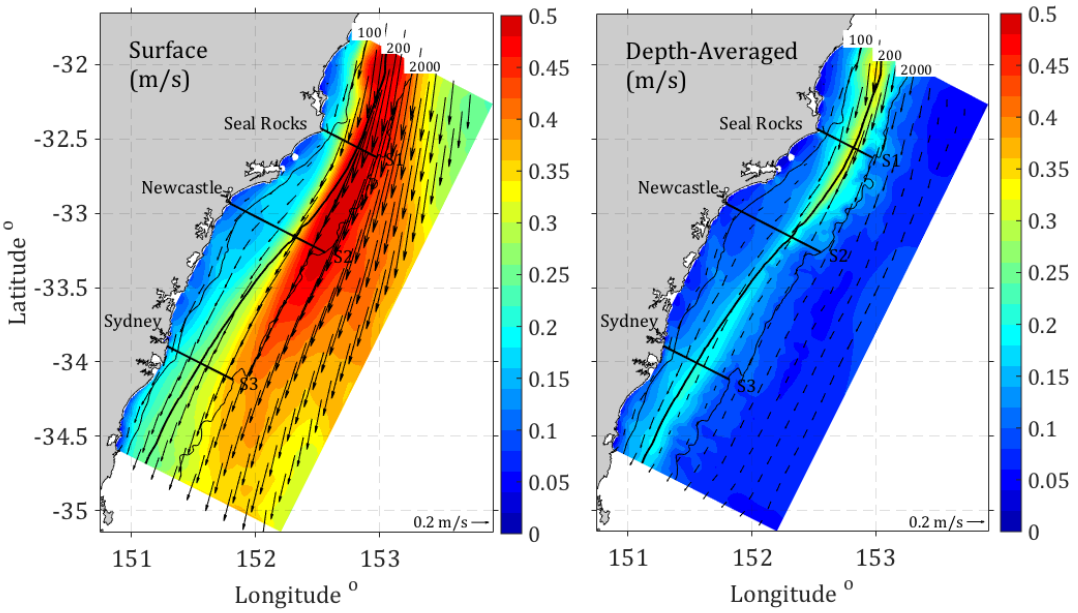

Fig. 3.1. Domain-wide two-year mean velocity fields (arrows) for the surface (left panel) and depth-averaged (right panel). The reference arrows in the bottom right of each panel represent 0.2 m s^{-1}. Color contour are the speed standard deviations. Every 20th vector is shown for clarity. Solid black lines show the 100, 200 and 2000 m isobath. Cross-sectional transects are indicated by black solid lines extending from the coast out to the 2000 m isobath at Seal Rocks, Newcastle and Sydney.

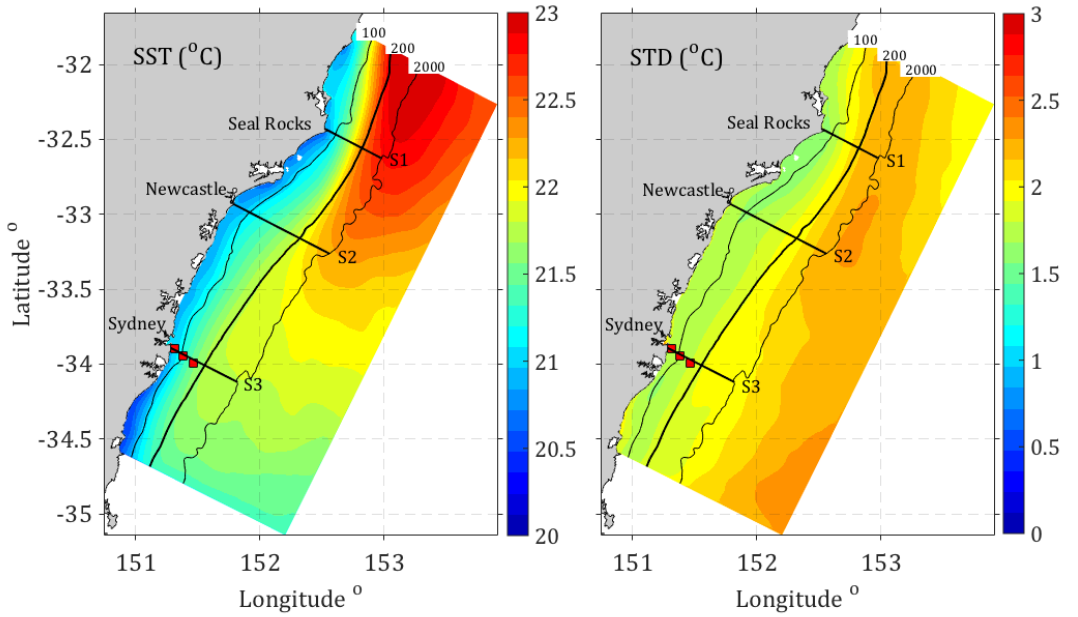

Fig. 3.2. Domain-wide mean Sea Surface Temperature (SST, left panel) and Standard Deviation, respectively (STD, right panel). Solid black lines show the 100, 200 and 2000 m isobaths. Red boxes indicate the location of the 3 mooring stations located across the shelf. Cross-sectional transects are indicated by black solid lines extending from the coast out to the 2000 m isobath at Seal Rocks, Newcastle and Sydney.

.

3.4.1.2 Seasonality

In summer, the EAC intensifies and separates from the coast further south as exemplified by various studies (*e.g.* Ridgway and Godfrey, 1997; Hamon et al., 1975; Godfrey et al., 1980). The intensification was successfully captured in the mean surface temperature and velocity fields outside the shelf break (outside the 200 m isobath). The highest mean temperatures ranged between 21 to 25°C and coincided with maximun velocities (peaking at -1.33 m s^{-1}) during the summer months (Fig. 3.3). Moreover, while the poleward flow turned slightly eastwards between 32 - 33.5°S, a weakened and variable poleward flow with warm temperatures continued south along the coast until 35°S. The variability of the surface circulation reflects the meandering of the EAC, with the largest variability found along the shelf-break boundary and beyond (Fig. 3.5).

Inside the shelf break (inside the 200 m isobath) (Fig. 3.5, a), mean surface temperatures were on average ~2.5°C lower in winter compared to summer, ranging between 18 - 20°C (Fig. 3.3, c). In offshore waters outside the 200 m isobath, mean temperatures were up to 5°C lower in winter than in summer. Highest temperatures extended down to 33°S, while poleward velocities dropped in magnitude at the same time by 52% (maximum of -0.69 m s^{-1}) (Fig. 3.3, Fig. 3.5). In addition, the poleward flow turned east further north (between 32°S and 33.5°S) in winter compared to summer (between 33.5°S and 34.5°S). Interestingly, as the EAC turned east during winter, it caused northward flowing currents outside the 200 m isobath and downstream on the shelf, provoking the formation of a small clockwise-rotating cold core eddy. However, this seasonal northward flow appeared to remain on the outer shelf and did not propagate across the shelf break boundary.

The seasonal signal for autumn and spring presented more transitional phases between summer and winter rather than strong individual seasons. In autumn, temperatures began to drop, and velocities became weaker in magnitude between 32°S and 33.5°S. During spring season, the pattern reversed, and the warm temperature tongue (EAC signal) started to extend further south after being restricted to the northern domain during winter. Instead of forming a small clockwise-rotating cold core eddy south of the separation zone as seen in winter, a slight eastward shift occurred between 33.5°S and 34.5°S with a poleward continuation until the southern end of the domain.

Domain averaged time series of SST (Fig. 3.3, bottom panel) for 2012 and 2013 revealed temperatures of ~24°C between January and April (summer and autumn).

Between April and June, temperatures dropped by as much as ~4°C. Spring marked the beginning of warmer temperatures in agreement with the seasonal signal of the EAC. However, the most notable distinction between 2012 and 2013 arose from the 3.5°C temperature difference between August and November.

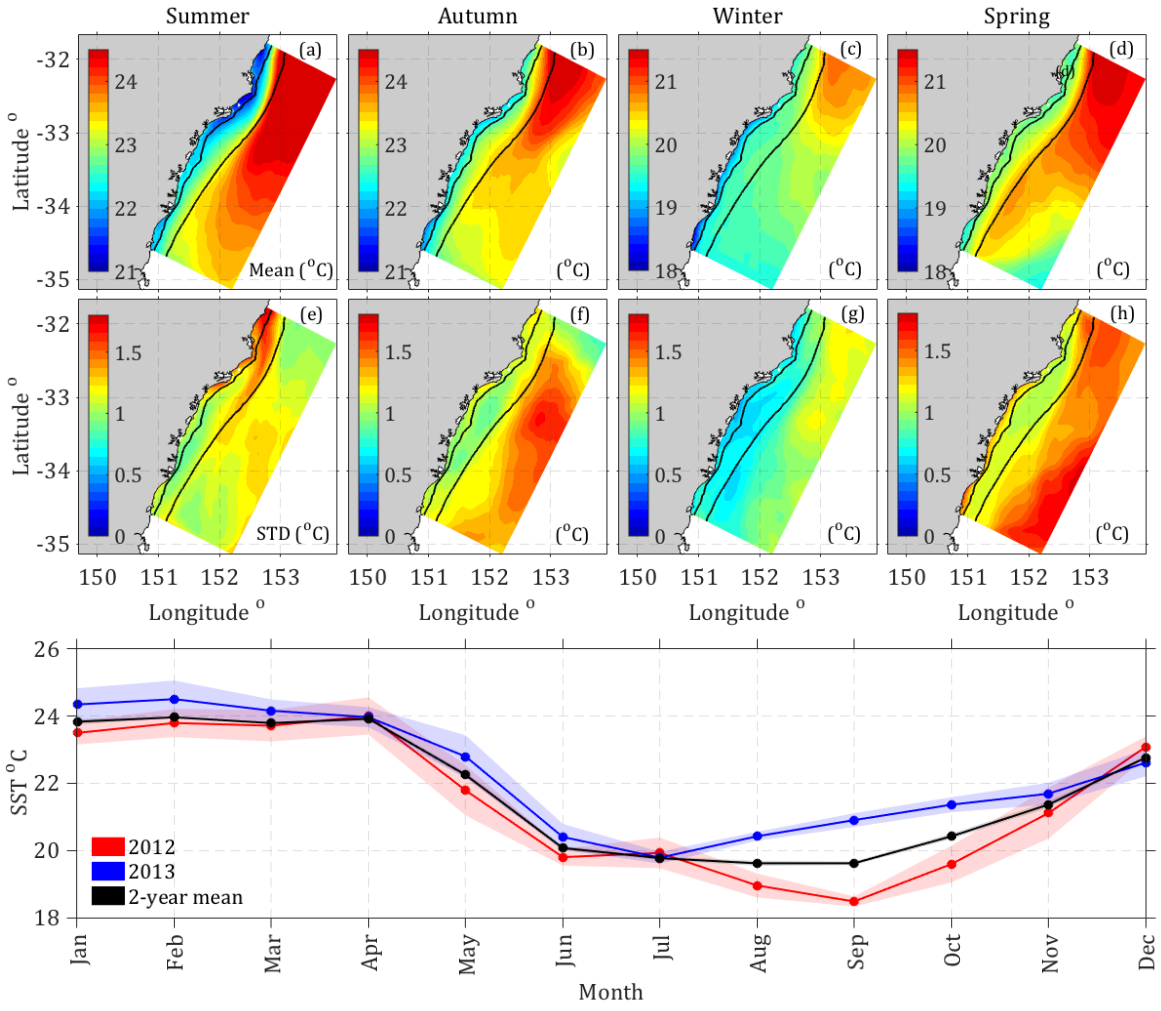

Fig. 3.3. Domain-wide seasonal mean Sea Surface Temperatures (SST, a,b,c,d) and associated standard deviations (e, f, g, h). Solid black lines indicate the 100 and 200 m isobath. Bottom: Area averaged SST showing monthly means for 2012 (red), 2013 (blue) and the total two-year mean (black). Shaded areas represent the standard deviations.

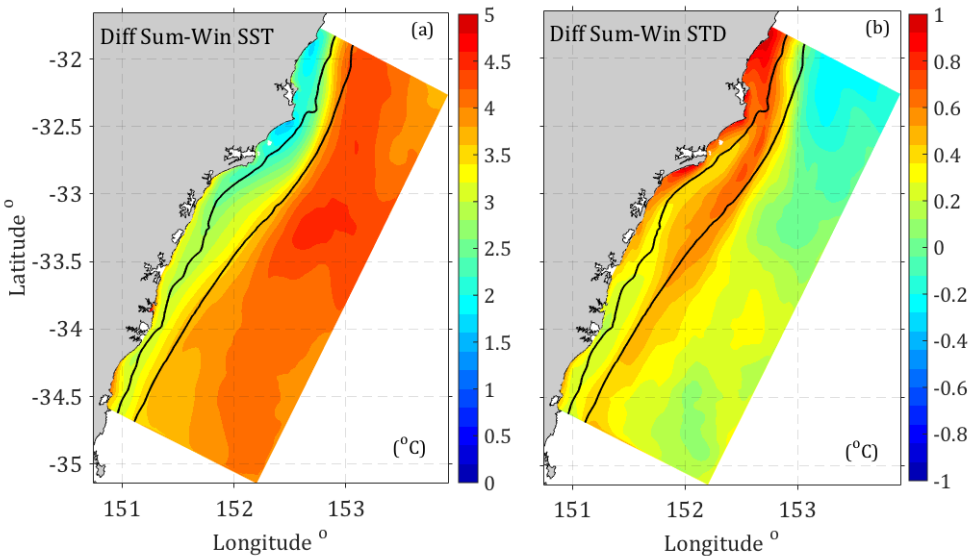

Fig. 3.4. Differences in domain-wide seasonal mean Sea Surface Temperatures for Summer and Winter (a) and associated differences in standard deviations (b). Solid black lines indicate the 100 and 200 m isobath.

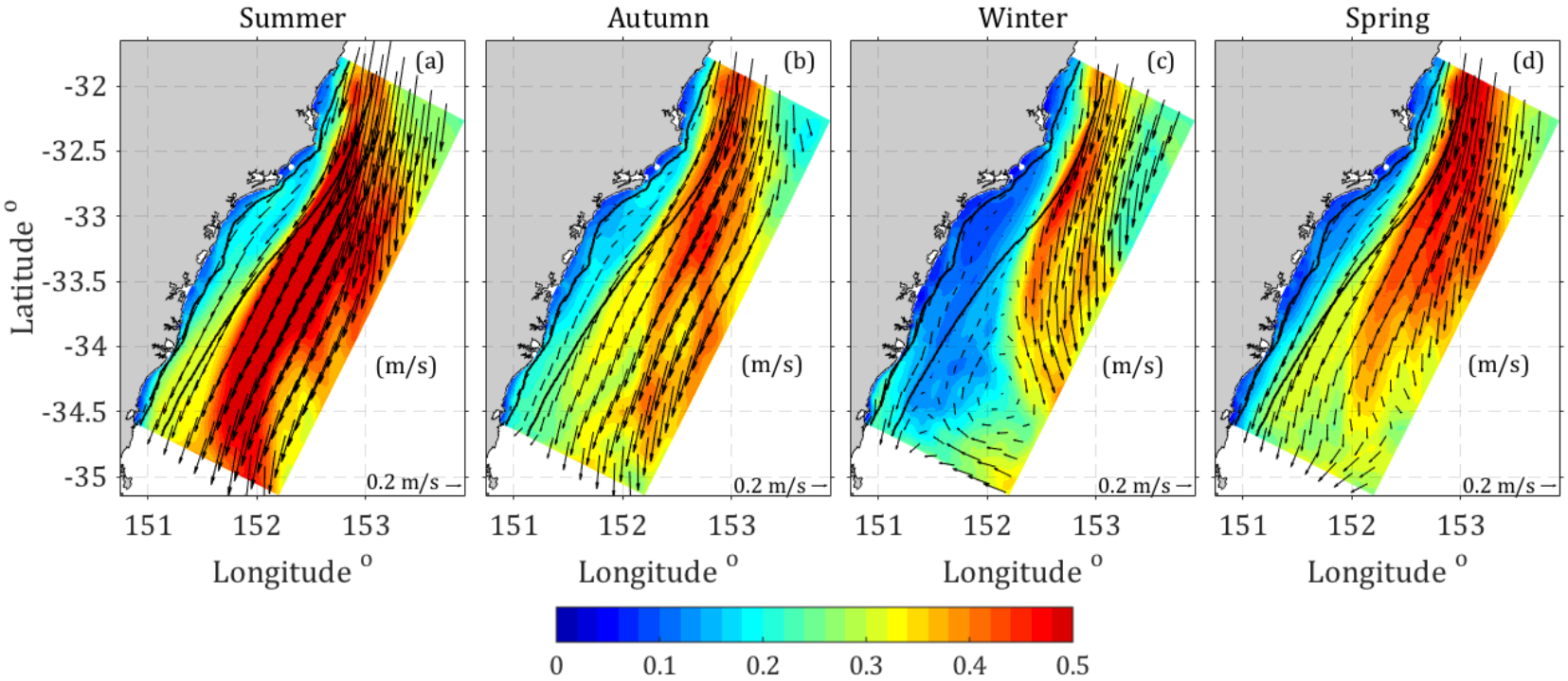

Fig. 3.5. Domain-wide seasonal mean velocity fields for the surface circulation. Colour contours are the speed standard deviations. Every 20th vector is shown for clarity. Solid black lines show the 100, 200 and 2000 m isobath. The reference arrows in the bottom right of each panel represent 0.2 m s^{-1} for the surface velocities.

3.4.2 Vertical Sections of Temperature and Velocity

3.4.2.1 Mean Temperature

Temperature patterns extending offshore from the coast, further highlighted the EAC's impact on the shelf. Temperature differences of about ~1ºC between the north (Seal Rocks) and the south (Sydney) (Fig. 3.6, left column) were observed in the upper 200 m of the water column.

At Seal Rocks, an uplift of density isolines coincided with a warm temperature tongue (mean temperature of 22.8ºC) that stretched 40 km in the longitudinal direction from the coast offshore and to about 50 m vertically in depth. The high variability was most likely driven by the meandering of the EAC and its occasional impingement on the shelf.

Off Newcastle (32.86ºS), the previous uplift of isolines started to flatten (Fig. 3.5, left column) and mean temperatures dropped by ~0.6ºC. The warm temperature tongue was now located between ~60 km to 80 km from the coast offshore (start of the 2000 m slope). While the warm temperature tongue migrated further offshore, it became shallower in nature, extending down to only 30 m in depth (Fig. 3.6, left column).

The Sydney transect at 33.9ºS revealed a more uniform temperature cross-shore distribution in the upper 30 m of the water column, with temperatures reaching 21.8ºC. In the along-shelf direction temperatures became colder and less stratified throughout the water column from Seal Rocks to Sydney (Fig. 3.6, left column).

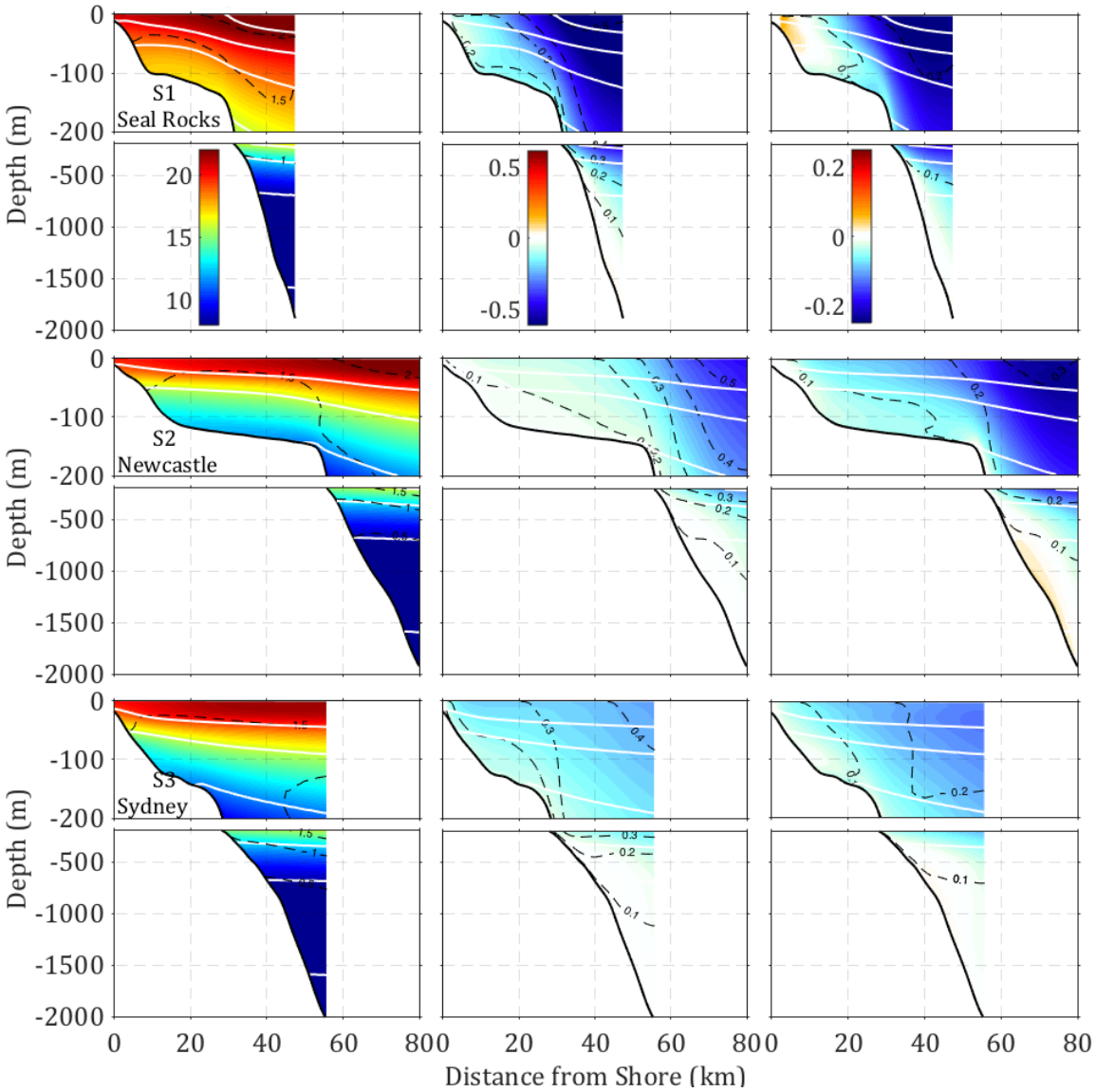

Fig. 3.6. Cross-sectional view of the mean temperature, along-shelf velocity (negative, poleward) and across-shelf velocity (negative, onshore) along the northern (top panel, S1), middle (middle panel, S2) and southern (bottom panel, S3) transects from 0-2000 m. The locations of the transects are marked by the black solid lines shown in Fig. 3.1. Dashed lines indicate the standard deviations with contour intervals of 0.5 for temperature, 0.1 for along and 0.05 for across-shelf velocities. White solid lines represent lines of constant density with a contour interval of 1024:0.5:1028 kg/m^3.

3.4.2.2 Along and Across-Shelf Velocities

The mean 3D shelf circulation was predominately poleward in direction with decreasing velocities from Seal Rocks (S1) in the north to Sydney (S3) in the south (Fig. 3.6, middle column). Maximum poleward velocities occurred between the shelf-break boundary (at the 200 m isobath) and the slope/open ocean boundary (at the 2000 m isobath). Across the narrow shelf off Seal Rocks (S1), the EAC impacted the shelf flow further inshore with maximum mean poleward velocities of -0.63 m s^{-1}. Off Newcastle, mean poleward velocities were 32% lower in magnitude reaching a maximum of -0.43 m s^{-1} at the shelf break boundary (200 m isobath). The weakest poleward flow with maximum speeds of -0.26 m s^{-1} (Fig. 3.6, middle column) were observed at the shelf break boundary off Sydney. Compared to the poleward flow, the magnitude of the mean across-shelf flow is about 50% weaker in magnitude and directed westward (negative, onshore) on the shelf.

3.4.2.3 Seasonality

The vertical temperature structure on the shelf reflected the EACs seasonal signal with temperature distinctions between summer, winter and spring (Fig. 3.7). The strong stratification during summer and autumn transitioned to a well-mixed water column in winter. In spring, a more stratified water column was then reestablished with the increase in temperatures.

At the shelf/slope boundary (*i.e.* 2000 m isobath) off Seal Rocks, temperatures of ~18^{o}C extended down to 200 m, with upward tilted isolines towards the coast. In autumn, temperatures decreased to ~10^{o}C at 100 m depth, while during summer temperatures of ~17^{o}C where found at similar depth. This rapid change in temperature with depth, however, has only been seen off Seal Rocks. Here, the EAC intrudes farther inshore, potentially pushing colder water up the slope and onto the shelf. Across Newcastle and Sydney, temperatures distributed more evenly during the summer and autumn periods with temperatures of ~24^{o}C in the upper 30 m and 15^{o}C at 200 m depth. The water column on the shelf is well-mixed during the winter period with ~ 4^{o}C colder temperatures compared to summer and autumn periods (Fig. 3.7).

Throughout the year, the signature of the EAC was strongly felt on the shelf, particularly off Seal Rocks. During summer, maximum mean poleward velocities (-1.12 m s^{-1}) were found 20 to 40 km from the coast. In Autumn and Winter, maximum velocities were found farther offshore and closer to the shelf break at a 40 km distance from the coast (Fig. 3.8, upper row). Inside the shelf break, poleward velocities were 50% weaker in magnitude and coherent through the upper 500 m of the water column. The vertical structure remains coherent throughout autumn, winter and spring.

Throughout the year, the prevalence of strong poleward velocities was confined to Seal Rocks. Off Newcastle, poleward velocities showed a 50% drop in magnitude compared to velocities off Seal Rocks, with maximum velocities of -0.65 m s^{-1} in summer. A warm temperature tongue located ~60 km from the coast and out to the 2000 m isobath accompanied the strong poleward flow. In agreement with Seal Rock, poleward velocities inside the shelf break were 50% weaker in magnitude. This is a strong indication that the outer shelf is more receptive to the influence of the EAC. During autumn and winter a more variable flow dominated the shelf circulation. A weak equatorward flow trapped between the 150-170 isobaths/40-60 km from the coast developed in summer and peaked with ~ 0.09 m s^{-1} in winter. However, this feature was absent in spring (Fig. 3.8). Off Sydney, mean poleward velocities increased inside the shelf break compared to Newcastle. Nonetheless, a decline of 20% in magnitude to -0.4 m s^{-1} was observed near the shelf break. During winter, the weak equatorward flow trapped to the shelf break off Sydney occurred 30-40 km from the coast, and it was pushed to a 1000 m depth, deeper than the equatorward flow off Newcastle. The equatorward flow patterns on the shelf were associated with across-shelf flows in an eastward (offshore) direction (Fig. 3.9). Offshore (positive) flow was seen for all seasons throughout the inner-shelf and water column only off Seal Rocks, at the shelf break off Newcastle and deep off Sydney during winter.

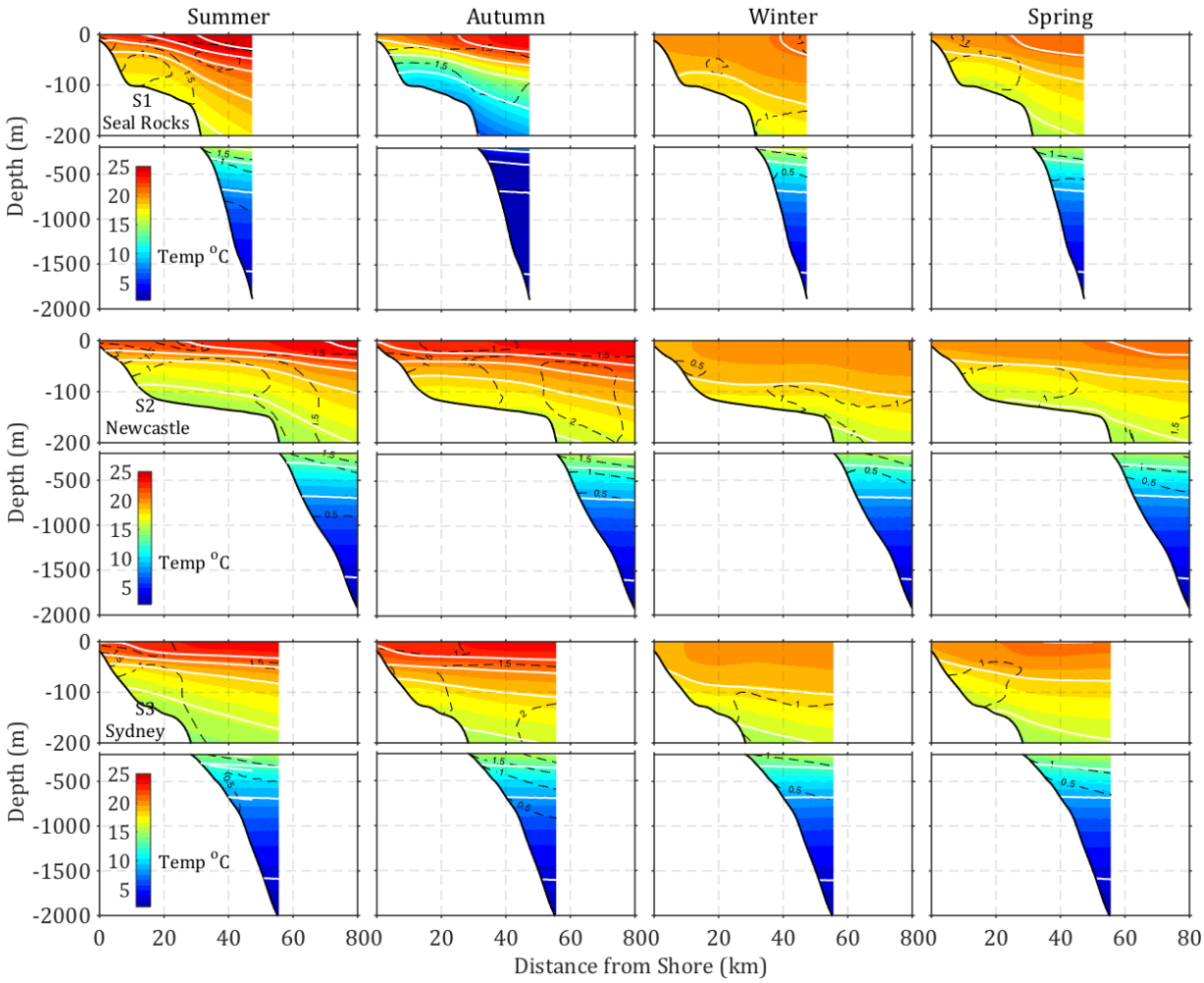

Fig. 3.7. Cross-sectional view of the seasonal mean temperature, across the northern (top panel, S1), middle (middle panel, S2) and southern (bottom panel, S3) transects from 0-2000 m. The location of the transects are marked by the 3 solid lines shown in Fig. 3.1. Dashed lines indicate the standard deviations with contour intervals of 0.5°C. White solid lines represent lines of constant density with a contour interval of 1024:0.5:1028 kg/m^3.

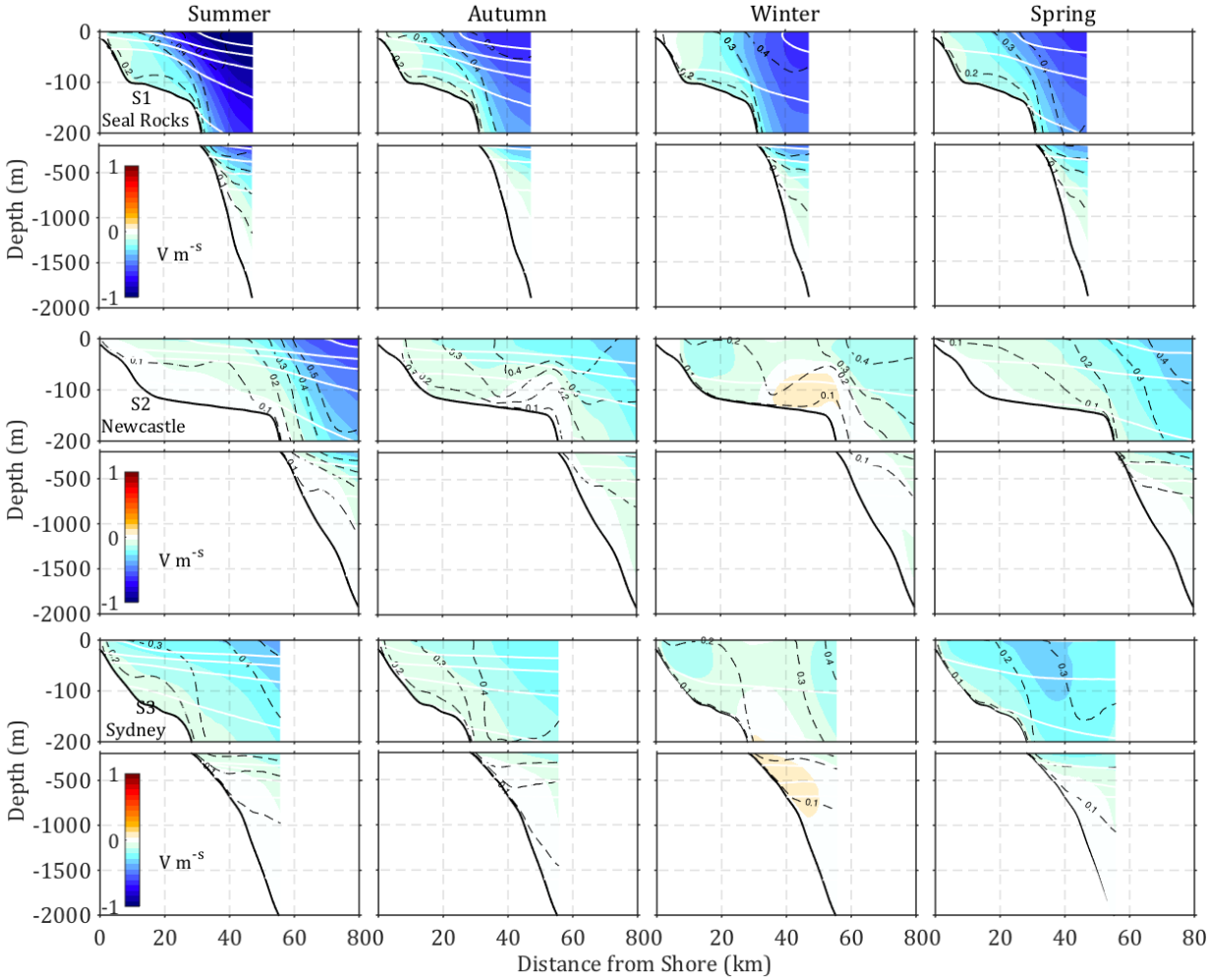

Fig. 3.8. Cross-sectional view of the seasonal mean along-shelf velocity (negative, poleward) across the northern (top panel, S1), middle (middle panel, S2) and southern (bottom panel, S3) transects from 0-2000 m. The location of the transects are marked by the 3 solid lines shown in Fig. 3.1. Dashed lines indicate the standard deviations with contour intervals of 0.1 m s^{-1}. White solid lines represent lines of constant density with a contour interval of 1024:0.5:1028 kg/m^3.

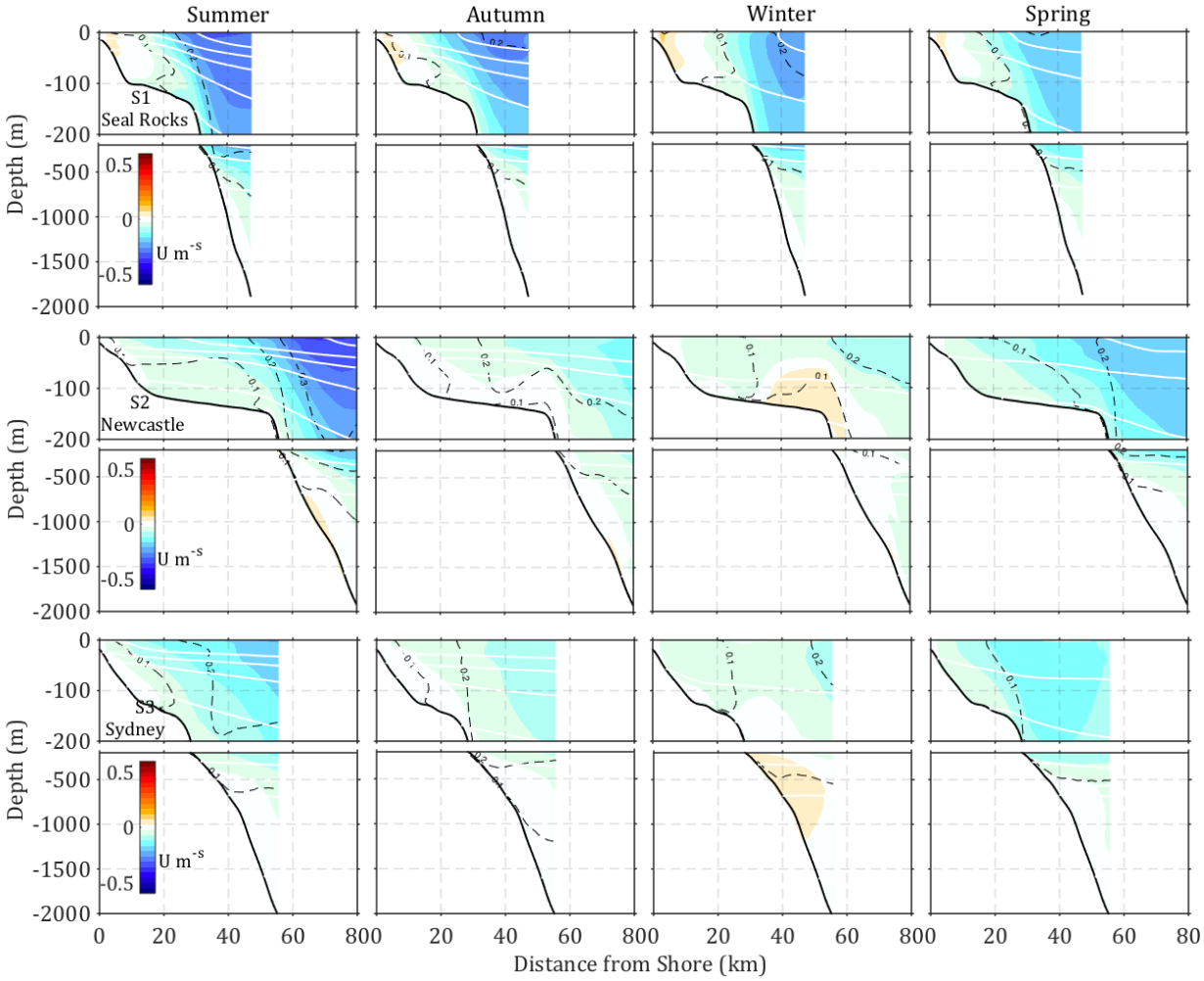

Fig. 3.9. Cross-sectional view of the seasonal mean across-shelf velocity (negative, onshore) across the northern (top panel, S1), middle (middle panel, S2) and southern (bottom panel, S3) transects from 0-2000 m. The location of the transects are marked by the 3 solid lines shown in Fig. 3.1. Dashed lines indicate the standard deviations with contour intervals of 0.1 m s^{-1}. White solid lines represent lines of constant density with a contour interval of 1024:0.5:1028.

3.4.3 Spatial Variability

3.4.3.1 Surface

The circulation variability can be explained by EOF modes 1-3 (Fig. 3.10, a-d), which accounted for ~ 62% of the overall circulation variability. The first spatial mode explained 30% of the variability and represents the path of the EAC and its separation from the coast. The second mode explained 21% of the variability and captured a dipole, showing the eddy dominance in the region. The dipole was characterized by a clockwise rotation in the north and anticlockwise in the south. The spatial pattern of Mode 3 accounted for 11% of the total variability and exhibited a structure similar to that previously found by Wilkin and Zhang (2007) who described it as being comparable to a planetary wave. This structure was characterized by a clockwise rotation in the northern domain, anticlockwise in the south, and a small eddy forming in the space between. Barnier (1988), and Moore and Wilkin (1998) theorized that the propagation of a planetary wave over a mid-ocean ridge, such as the Lord Howe Rise (LHR), could be a possible mechanism for the spatial pattern of mode 3 by emitting energy south-westward along the shelf. LHR extends about 2000 m across the basin (southwest of New Caledonia to the Challenger Plateau (Geoscience Australia) with depths of a 1000 m along the upper crest (Ridgway and Dunn 2003).

The temporal evolution of the spatial modes was indicated by the principal component time series (Fig. 3.10, e). For mode 1, it generally indicated a strong poleward circulation during the summer periods (positive values) and an equatorward direction (negative values) between the autumn and winter transition (May-July). An opposite trend was highlighted by mode 2, with positive values during winter and negative in summer. Due to the dipole structure of mode 2, this lead to an equatorward flow north of 34^{o}S during winter and poleward flows south of 34^{o}S. Mode 3 on the other hand was characterized by a more variable pattern. A spectral analysis of the principal component time series reveals peaked at 124 days in all three modes with the highest power in mode 1 and 2. High energy associated with a 93 days periodicity were seen in mode 2 and 3, but absent in mode 1 (Fig. 3.10, f).

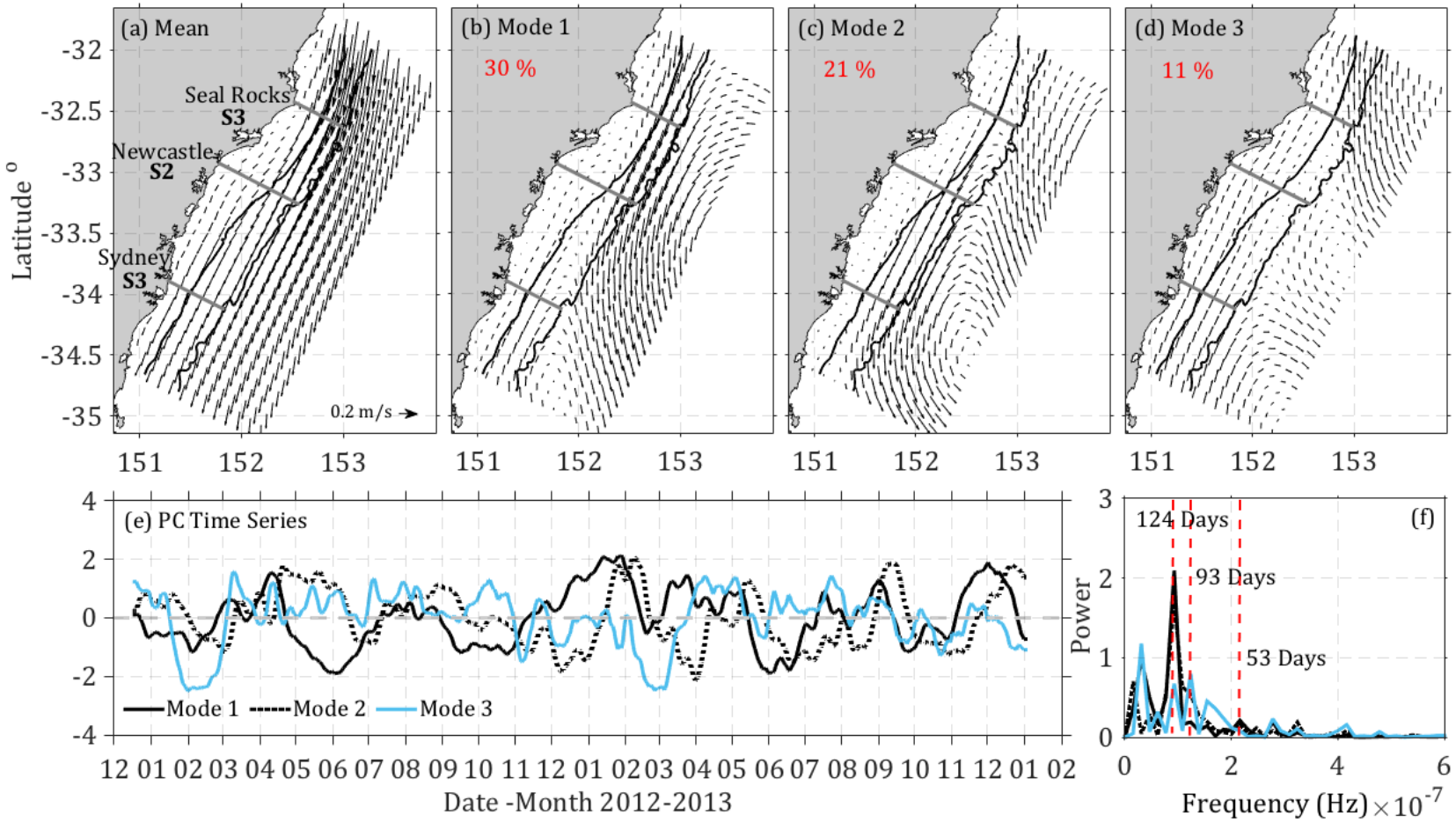

Fig. 3.10. EOF analysis for daily surface velocities from the HSM. (a) Mean, (b-d) Mode 1-3. Percentages represent the variances accounted for by modes 1-3. The associated principal component analysis (PC) for modes 1-3 is shown in (e). Solid black lines indicate cross-sections at Seal Rocks (S1), Newcastle (S2) and Sydney (S1). (f) Power spectrum of PC time series for modes

3.4.3.2 Vertical Sections across the Shelf

The variability of the along-shelf velocity component is to ~90% explained by the first 3 EOF modes (Fig. 3.11). Mode 1 contributed ~70% to the overall variability and was characterized by along-shelf flows in opposing directions throughout the inner (~0-50 km from the coast) and outer shelf (~50-and more km from the coast). Poleward flows were observed closest to the shelf break at Seal Rocks; whereas off Newcastle and Sydney, zero velocity contour lines (delimiting flow reversals) were pushed further offshore, away from the shelf break.

Mode 2 contributed between 14-17% to the variability. Off Seal Rocks it showed a coherent along-shelf flow on the shelf. A tripole emerged off Newcastle: weak velocities inside the shelf break; along-shelf flow in the opposite direction close to the coast and offshore. Sydney had a more variable pattern with a dipole structure developing on the shelf. During a positive temporal component equatorward flows dominated from the coast out to the slope/open ocean boundary with the adjacent flow being poleward (Fig. 3.11).

Mode 3 had a tripole structure along each transect contributing 7-9% to the total variability. Most obvious was the encroachment of the poleward flowing velocities across the shelf break off Seal Rocks, when the temporal component is positive and equatorward flows occured offshore. Newcastle and Sydney on the other hand presented the transition of the tripole feature farther offshore.

The spectral analysis of the principle component time series of all three EOF modes (Fig. 3.12, d-f) exposed a prominent peak at 122 days. This peak was most defined in mode 1, off Sydney and Newcastle. Additional peaks appeared at 73 days in mode 2, which turned out to be most energetic off Seal Rocks.

The correlations between the principle component time series of the EOFs were strongest between Seal Rocks and Newcastle (greater than 0.66, indicating that these modes typically vary together). Correlations between Seal Rocks and Sydney were less than 0.4, stating that Sydney varies more independently).

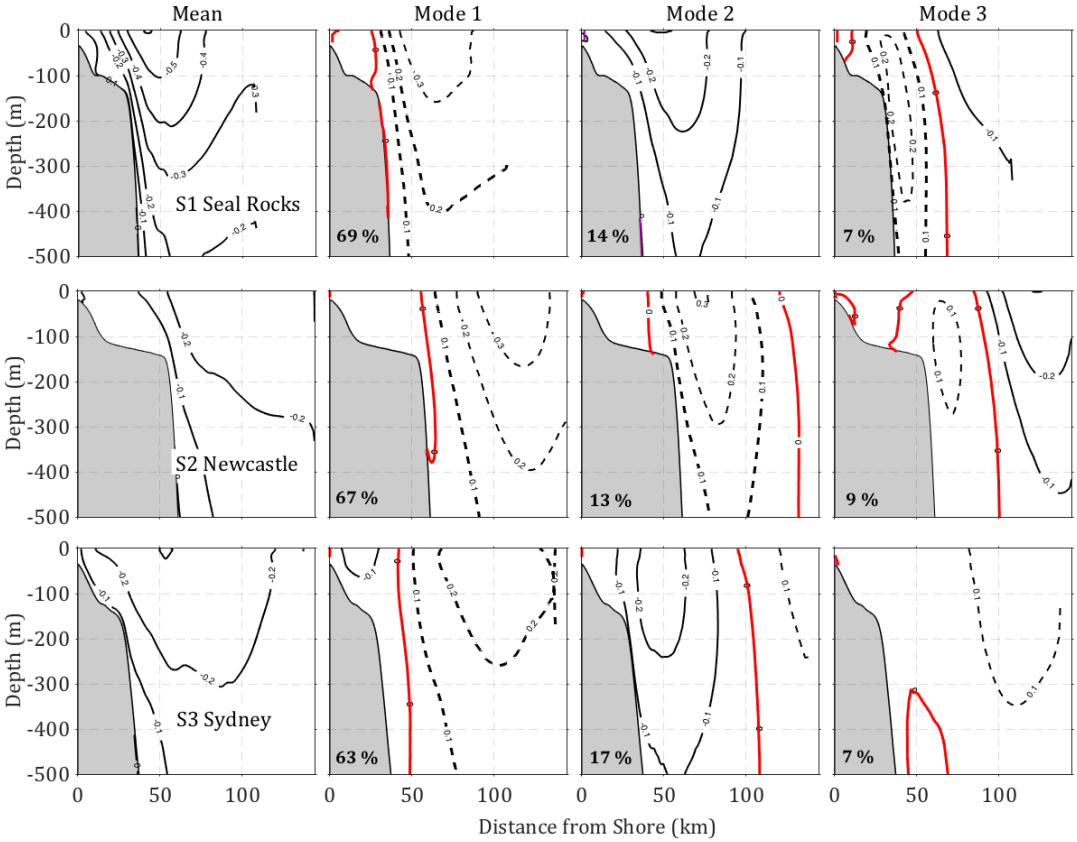

Fig. 3.11. Mean and EOF modes of modeled along-shelf velocities at sections S1 (top row), S2 (middle row) and S3 (bottom row). Negative, positive values are contoured with solid, dashed lines, respectively. Contour intervals are 0.1 m s^{-1} for means and EOF modes. The red line indicates the 0 contour. Percentages show the variances accounted for by the specific modes.

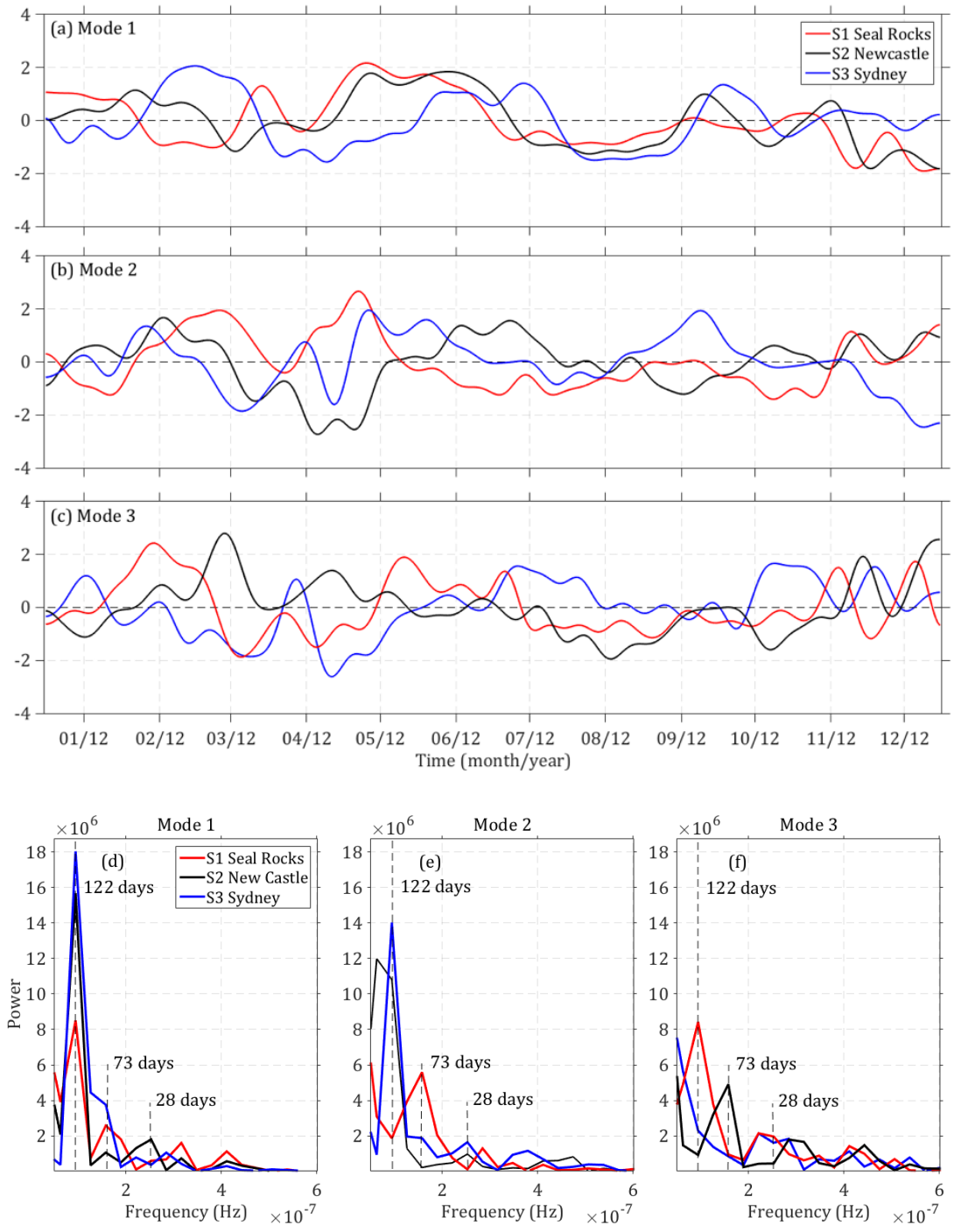

Fig. 3.12. The principal component time series (PC) for EOF mode 1-3 with the x-axis presenting the date, y-axis the amplitude of the PC; (d-f) Power spectrum of PC time series for modes 1-3.

3.4.4 Along and Cross-Shelf Transport on the Shelf

3.4.4.1 Mean Along shelf Transport

The overall two-year mean transport calculated for transects extending across the shelf (from the coast out to the 2000 m isobath) showed a maximum along-shelf transport off Seal Rocks. Southward along the coast, the transport decreased (Fig. 3.13). This pattern is in good agreement with the mean poleward velocity fields found on the shelf (section 3.4.2.).

The along-shelf transport across the Seal Rock transect with magnitudes of - 4.4 Sv (STD 4 Sv), coincided with the strongest observed EAC velocities. Off Newcastle, the along-shelf transport displayed a 30 % decrease compared to Seal Rocks with a mean magnitude of -3.1 (STD 5.7 Sv). Across the shelf off Sydney, velocities were weakest and exhibited a 48% decrease in magnitude with a mean of -1.6 (STD 5.6 Sv) compared to Seal Rocks (Fig. 3.12).

3.4.4.2 Seasonality

Maximum poleward transport happened during the summer and spring months (Fig. 3.13). While summer had the largest mean transport off Seal Rocks (-5.4 Sv), the remaining seasons (Autumn, Winter and Spring) suggested almost no variability in transport means (-3.3 Sv in Autumn and -3.8 Sv in spring). This highlights the persistence of the EAC throughout the year off Seal Rocks (Fig. 3.13). In Newcastle on the other hand, where the flow started to become more variable, a ~50% drop in transport to -1.56 Sv was observed during the winter period. Summer and spring periods had transports of -3.58 Sv and -3.36 Sv. In comparison to Seal Rocks and Newcastle, Sydney exhibited the largest seasonal variability with transports peaking in spring (Fig. 3.13). Here, peak poleward transport was found during the spring period with -3.35 Sv; standard deviations revealed a higher variability in summer and autumn.

3.4.4.3 Variability over the Shelf

To gain a better understanding of the transport variability on the shelf, the along-shelf transport was examined across the length of each shelf segment (*i.e.* across the inner (0-100 m), middle (100 -200 m), outer shelf (200-2000 m)), as well as the total transport (0-2000 m).

The two-year mean transport across the middle and outer shelf revealed a steady decrease in magnitude from Seal Rocks to Sydney. The opposite case occurred across the inner shelf, where the transport increased by 50% from Seal Rocks (-0.03 Sv) to Sydney -0.07 Sv (Fig. 3.13). Interestingly, off Seal Rocks, transport magnitudes increase from the coast towards the core of the EAC (Fig. 3.13, a-d). In contrast, a reversed pattern emerges in Sydney where the transport decreases towards the core (Fig. 3.13, i-l).

The seasonal means on the inner, middle and outer shelf exposed a variable impact of the EAC on the shelf (Fig. 3.13). The outer shelf (200-2000 m) had the highest seasonal poleward transport during summer. The structure in the along-shelf direction presented a similar pattern to the overall transport, with decreasing magnitudes from Seal Rocks to Sydney. During autumn, the transport became more variable in nature, suggesting that flow reversals were more frequent, particularly off Sydney. While poleward transport on the outer shelf dominated during Summer, Autumn and Spring; equatorward transport occurred off Sydney during Winter. This equatorward transport was confined only to the outer shelf.

The inner shelf uncovered an overall different picture, where the transport is less affected by the actual EAC signal. Strongest magnitudes along with a low variability occurred during spring off Sydney. Seal Rocks on the other hand, had the largest variability during winter. Furthermore, correlations of daily along-shelf transport between Seal Rocks, Newcastle and Sydney have been computed to understand if the circulation was coherent from north to south, or if different circulation regimes were present.

The inner shelf section (0-100) was correlated from north to south, with a CC= 0.65 correlation between Seal Rocks and Newcastle, and 0.55 between Seal Rocks and Sydney (Table 3.2). Interestingly, correlations across the middle (100-200 m) and the outer shelf sections (200-200 m) were much lower. No significant correlations were determined between the middle shelf off Seal Rocks and Newcastle, or between Seal Rocks and Sydney. However, Newcastle and Sydney were highly correlated with a

CC=0.72 (Table 3.3). The outer shelf section, however, clearly elucidated that transport patterns off Seal Rocks and Newcastle were similar with CC=0.62. The transport between Newcastle and Sydney had a smaller correlation as well as the correlation between Seal Rocks and Sydney with CC=-0.3 (Table 3.3)

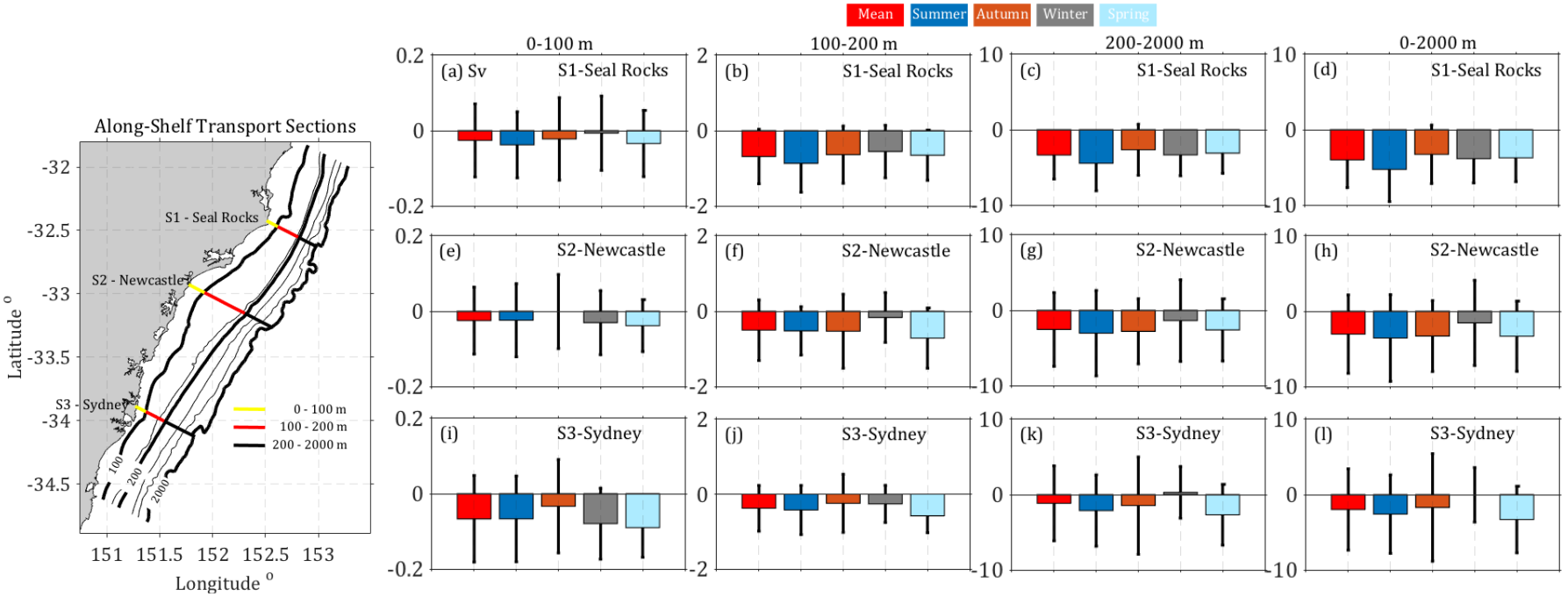

Fig. 3.13. Seasonal along-shelf transport (mean) on the Hawkesbury Shelf. (a,e,i) section across the inner shelf (0-100 m) , (b,f,j) across the middle shelf (100-200) and (c,g,k) across the outer shelf (200-2000), (d,h,l) across the entire shelf (0-2000) for Seal Rocks (S1), Newcastle (S2) and Sydney (S3), respectively. Errorbars show the associated standard deviations

Shelf Sections (m)	S1 / S2	S1 / S3	S2 / S3
0-100 lag (hrs)	0.65	0.55	0.78
100-200 lag (hrs)	0.37	0.04	0.72
200-2000 lag (hrs)	0.63	-0.30	0.25

Table 3.2. Correlation coefficients of along-shelf transport between shelf sections at Seal Rocks (S1) and Newcastle (S2); Seal Rocks (S1) and Sydney (S3); Newcastle (S2) and Sydney (S3). Correlation coefficients shown are significant with a 99% confidence interval.

Shelf Sections (m)	S1	S2	S3
0-100 / 100-200 lag (hrs)	0.65	0.66	0.85
100-200 / 200-2000 lag (hrs)	0.70	0.35	0.71
0-100 / 200-2000 lag (hrs)	0.13	-0.03	0.41

Table 3.3. Correlation coefficients of along-shelf transport between shelf regions: inner (0-100) and middle (100-200) shelf, middle (100-200) and outer shelf (200-2000), inner (0-100) and outer shelf (200-2000). Correlations shown represent shelf regions at Seal Rocks (S1), Newcastle (S2) and Sydney (S3). Correlation coefficients shown are significant with a 99% confidence interval.

3.4.4.4 Mean Cross-Shelf Transport

Over the two-year period, the mean cross-shelf transports revealed a strong and dominant offshore flow across the S1x segment encompassing Seal Rocks (Fig. 3.14, a-c, red shading). Standard deviations indicated that onshore flow occurs, but it is small in magnitude, while offshore flow can be twice as large than the mean. Offshore transport occured throughout the shelf, across the 100 m, 200 m and 2000 m isobaths, increasing

in magnitude towards the open ocean. More specifically, the mean cross-shelf transport ranged from 0.14 Sv across the 100 m isobath, to 4.6 Sv across the 2000 m isobath.

Downstream, across the S2x section a more complex pattern emerged with mean transport directions towards the coast across the 100 and 200 m isobaths, but transport in the offshore direction across the 2000 m isobath (Fig. 3.14, a-c, green shading). Magnitudes were up to 5 times smaller compared to the offshore transports off Seal Rocks and variability roughly centered at zero inducing across-shelf transport in both directions. Further south, across the S3x section, which covers the Sydney area, the mean across-shelf transport showed onshore flow across the 100 m isobaths (Fig. 3.14, a-c, blue shading), and offshore flow across the 200 and 2000 m isobaths. The variability indicated flow reversals across the inner, middle, and outer shelf.

3.4.4.5 Seasonality

The seasonal signal for the Seal Rocks section was weak, highlighting a persistent transport in the offshore direction throughout the year with strongest magnitudes associated with the summer period (Fig. 3.14, a-c).

Near Newcastle, there was a consistent onshore transport across the 100 m isobath with similar magnitude from Summer to Spring (-0.03 to 0.04 Sv in spring); the mid-shelf showed seasonality with offshore transport in summer, autumn and spring, and strong onshore transport during winter. Finally, the transport across the 2000 m isobath indicated large fluctuations with strongest offshore transport during winter and almost zero transport during spring.

In Sydney, the seasonal transport was variable across the 100 m isobath. Winter was dominated with an onshore transport across the shelf (100-2000m isobaths), whereas during the summer period offshore transport across the entire shelf was found. Thus, the Sydney region experienced persistent onshore transport during winter, supported by flow reversals in the along-shelf direction on the outer shelf.

3.4.4.6 Variability over the Shelf

Correlations in cross-shelf transport at the three shelf transects exposed a close relationship between the inner and middle shelf circulation (Table 3.4). Significant correlations between these shelf sections (CCs) of 0.6 and 0.7 were found at Seal Rocks and Sydney. In the Newcastle region the correlation between the inner and middle shelf decreased to 0.3.

The mid and outer shelf sections were well correlated at all three transects with CCs of 0.47 off Seal Rocks, 0.63 off Newcastle and 0.6 off Sydney. Lastly, correlations of cross-shelf transports across the inner and outer shelf showed the independence of the two regimes with no significant correlation off Seal Rocks and Newcastle. In Sydney, on the other hand, the transport varied concurrently across the shelf with a correlation of 0.47 between the inner and outer shelf.

Isobath (m)	**S1**	**S2**	**S3**
100 / 200 lag (hrs)	0.60	0.35	0.70
200 / 2000 lag (hrs)	0.47	0.63	0.60
100 / 2000 lag (hrs)	-0.02	-0.04	0.47

Table 3.4. Correlation coefficients of cross-shelf transport between the 100 and 200 m, 200 and 2000 m, 100 and 2000 m isobath. Correlations are shown for sections of the isobaths at Seal Rocks (S1x), Newcastle (S2x) and Sydney (S3x). Correlation coefficients shown are significant with a 99% confidence interval.

Patterns of periodicities and energy distribution were shown for the along (Fig. 3.15, a-c) and cross-shelf time series (Fig. 3.15, d-f). For the along-shelf transport time series, a periodicity of 90 - 140 days dominated the transport across the mid and outer shelves, with highest energies in the offshore region, whereas the inner shelf had no prominent periodicities. Highest energies on the inner shelf corresponded to weather band periodicities (between 9 - 10 days in Seal Rocks and Newcastle, and Sydney). However, energy was also observed in the 30 - 45 day range.

The periodicities of the cross-shelf transport at the three transects had strong peaks in the mescoscale band (90-120 days), particularly at offshore at the 2000 m isobath. From the 200 m isobath inwards, peaks have a shorter periodicity between 30-90 days.

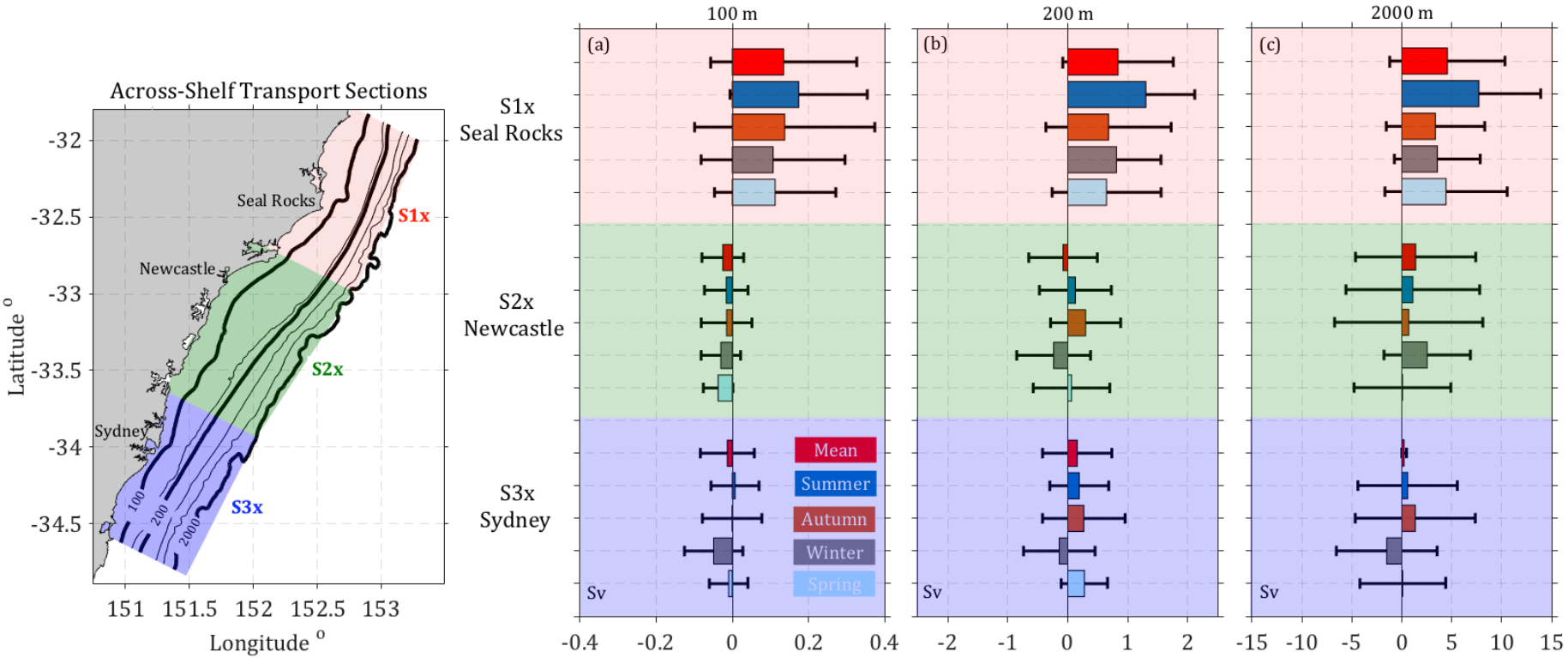

Fig. 3.14. Seasonal mean cross-shelf transport on the Hawkesbury Shelf. (a) across the 100 m isobath, (b) across the 200 m isobath and (c) across 2000 m isobath for sections encompassing Sydney (S1x), Newcastle (S2x) and Sydney (S3x), respectively. Errorbars show the associated standard deviations.

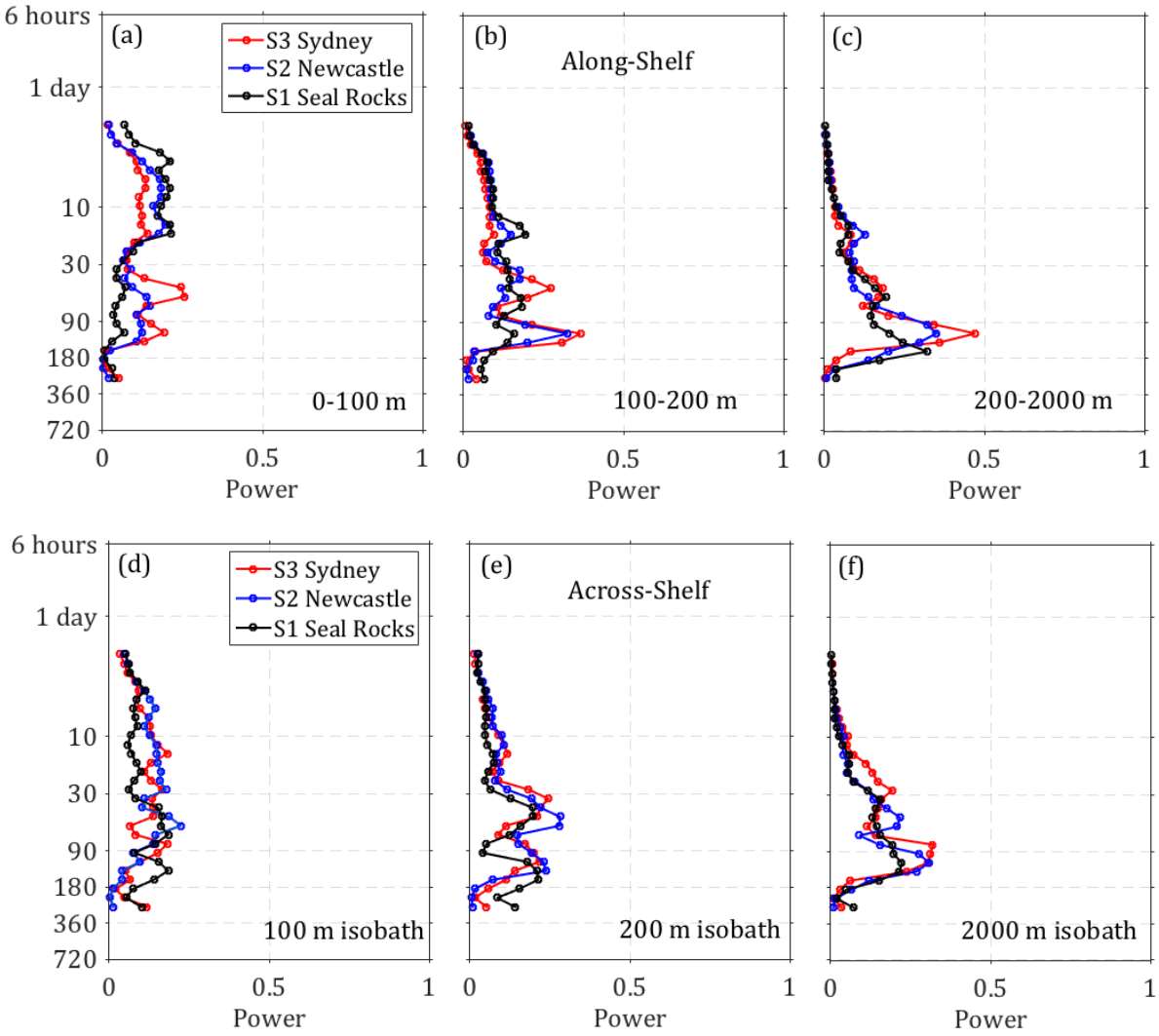

Fig. 3.15. Global Morlet wavelet power spectrum for Along and Cross-shelf transport daily time series. (a-c) Along shelf transport for shelf sections ranging from 0-100, 100-200 and 200-2000 m. For the along-shelf transport, different colors present sections at Seal Rocks (S1), Newcastle (S2) and Sydney (S3). (d-e) Cross-shelf transport across the 100, 200 and 2000 m isobath. The different colors indicate location of the cross-shelf transects at S1x, S2x and S3x.

3.4.5 Transport Budget

Two main aspects of the mean transport were evident in Box A (Fig. 3.16, middle panel) First, the mean transport into the box was predominantly through its northern boundary and was poleward in direction (-16.1 Sv). Secondly, out of the box, through its southward boundary, the poleward transport decreased by about 50% to -6.59 Sv. Cross-shelf transport through the eastern boundary of the box was dominated by an intense offshore transport of 9.56 Sv, which balanced the budget in box A with a residual of 0.011 Sv.

Box B encloses the Newcastle region with the eastern boundary of the box extending to a depth of 4321 m. Poleward transport into the box through the northern boundary was 6.59 Sv, as mentioned above. The poleward outflow of box B through the southern boundary increased to 8.8 Sv. This was balanced by a mean onshore cross-shelf transport of 2.18 Sv. Box B had a residual of -0.01 Sv.

The Sydney box (box C), had a mean poleward inflow of 8.8 Sv through its northern boundary, and a poleward outflow of 14.1 Sv through its southern boundary. This was balanced by an onshore transport of 5.4 Sv. The budget of box C had a residual of -0.08 Sv (Fig. 3.16, middle panel).

On the shelf, poleward flow dominated with water being transported offshore by the EAC, particularly in the northern part of the domain at Seal Rocks. South of 33^{o}S, where the EAC is typically separated from the coast, transport was more variable with a strong onshore component. Although the spatial pattern and direction of the transport was not affected by seasons, the magnitudes did exhibit seasonality. During summer, the transport values were twice as large as those during autumn and winter, particularly at the northern part of the domain, where the EAC inflow was strongest (Fig. 3.16, middle panel).

To investigate if transport characteristics were influenced by mesoscale variability, the transport budget was determined separately for periods of circulation patterns similar to those revealed by each dominant EOF mode. Again, the budgets followed the two-year mean pattern with transport being dominated in the poleward direction throughout each mode with strongest magnitudes being present during the EAC and separation mode 1 with exception in the Newcastle area, were the strongest fluxes were observed during mode 2, the eddy mode as described in section 3.4.3. Onshore transport off Sydney was twice as large during mode 1 compared to mode 2 and mode 3.

Off Seal Rocks, where offshore transport was dominant, mode 3 revealed the largest magnitudes (Fig. 3.16, right panel).

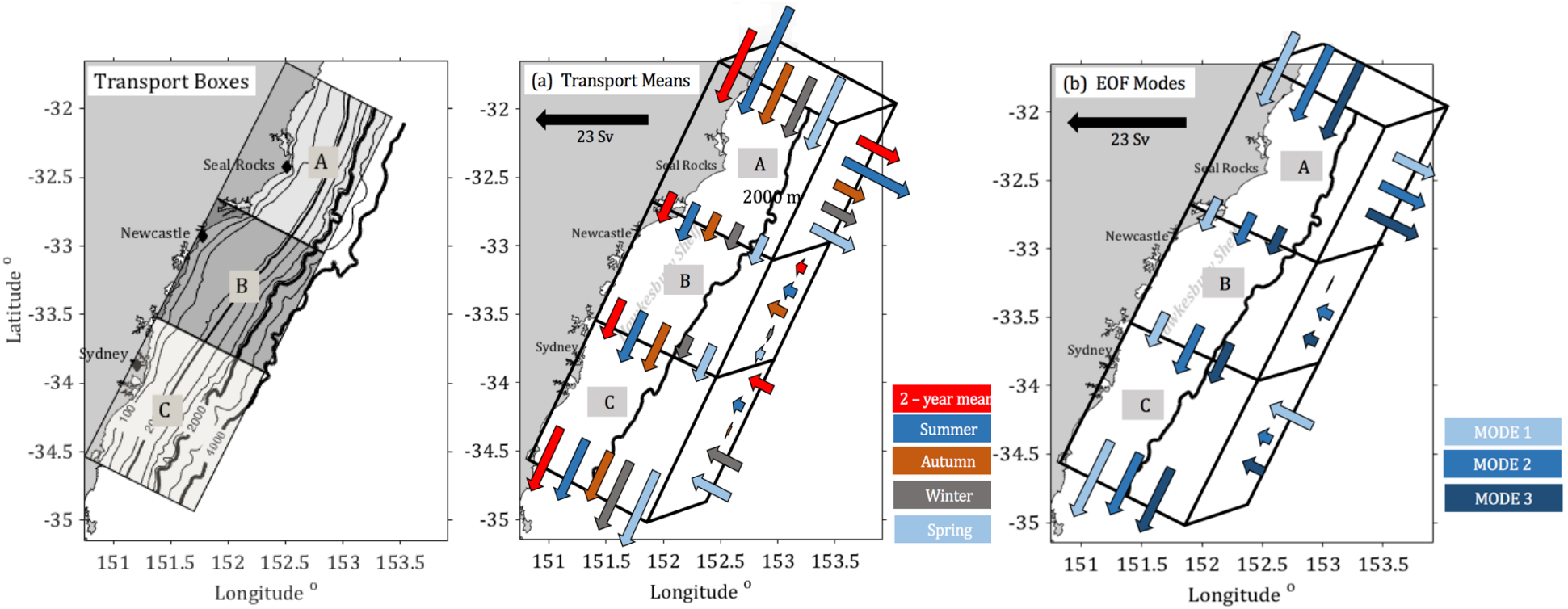

Fig. 3.16. Mean transport budgets for the Hawkesbury Shelf. Schematic of the budget area (Far left panel), (a) two-year and seasonal means. (b) for time periods of dominating EOF modes.

Lastly, the vertical structure of the cross-shelf component of the transport budget was investigated to discern the depths at which the shelf-exchanges occurs. Due to the orientation of the HSM grid, the cross-shelf transport was estimated across grid cells over the 2000 m isobath in the northern part of the domain (*i.e.* off Seal Rocks), and across grid cells over the ~ 4000 m isobath in the southern part of the domain (*i.e.* off Sydney, Fig. 3.17, bottom panel).

The two-year mean cross-shore transport off Seal Rocks showed a coherent offshore transport with depth (0-2000m). Throughout the summer months, the offshore transport strengthened with depth, confirming the intensified EAC during summer. Winter on the hand, revealed the weakest offshore transport with depth, indicating the EAC separating further north during winter months. Further south, towards Newcastle, weakened transports were observed with a prevailing onshore direction.

The upper water column (down to 200 m) demonstrated little to no cross-shelf transport. However, at depth, between 2000-3000 m, there was a stronger onshore flow. A small area located between 33.7 - 33.8ºS with depths of 3000 to 4000 m exhibited the offshore movement of water. Past Newcastle, the transport structure became more complex with offshore transport in the upper 200 m south and onshore transport with depth. This pattern strengthened in summer and autumn, with offshore transport extending down to ~ 1000 m (Fig. 3.17).

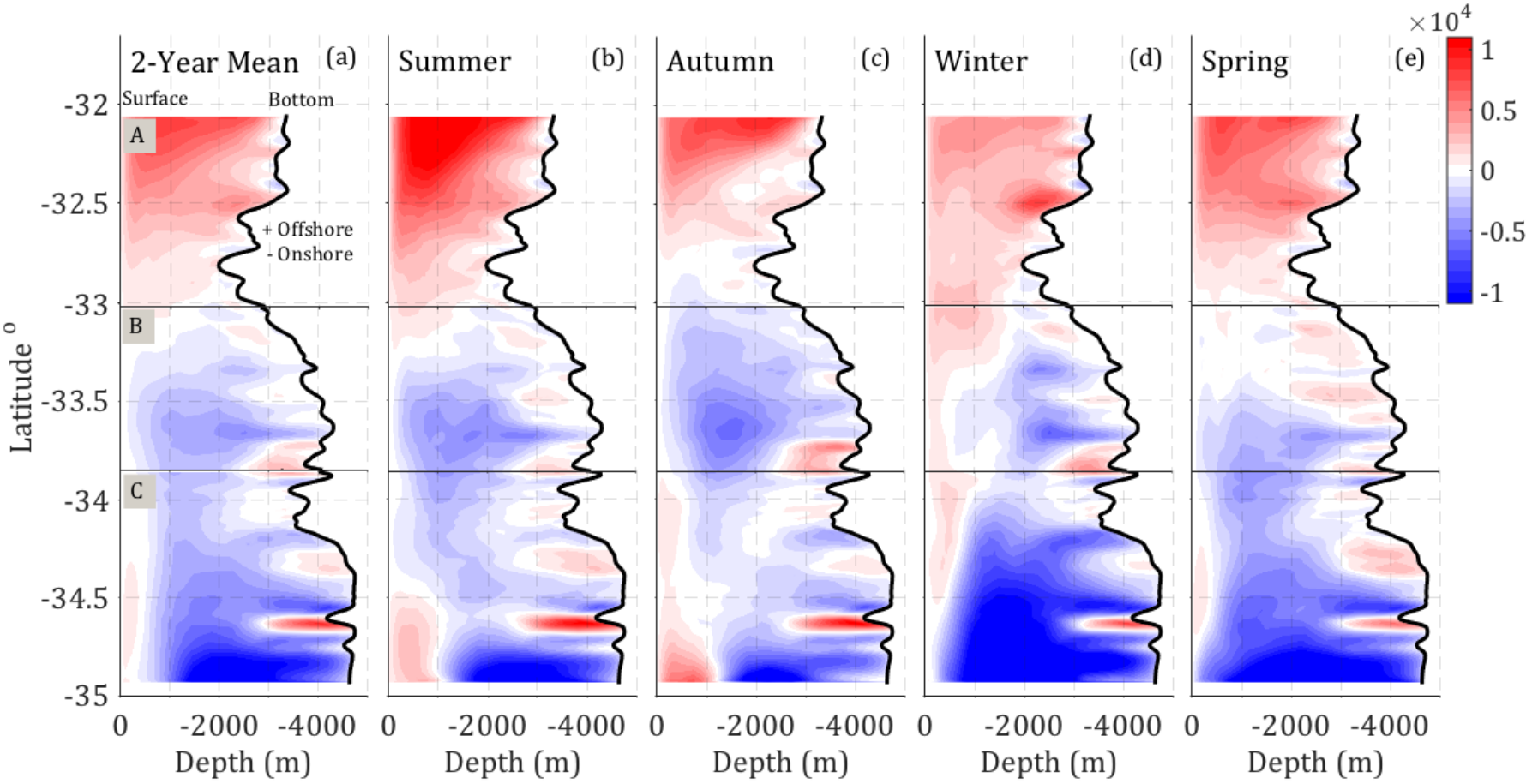

Fig. 3.17. Vertical structure of cross-shelf transport (m^2/s). (a) two-year mean, (b) Summer, (c) Autumn, (d), Winter, (e) Spring. The direction with latitude is from north (Box A) to south (Box C) as seen in Fig. 3.15. Blue (-) shows onshore transport, red (+) shows offshore transport. The black line highlights the bathymetry along the outer boundary of the boxes.

3.5 Discussion

This chapter diagnoses the mean state of the 3D circulation and its variability on the Hawkesbury Shelf using the 750 m high-resolution shelf model, configured in Chapter 2. The approach allows the identification of transport regimes and circulation variability on the shelf, the main goals of the Chapter 2. For the first time the local-scale transport variability within the continental shelf off southeast Australia (*i.e*. the Hawkesbury Shelf) is quantified. Additionally, dominant circulation regimes and the impact of the EAC on the inner, middle and outer shelf regions are elucidated.

The transport and correlation analyses point out that the transport variability in the cross and along-shelf direction is related to different regimes impacting the shelf-exchanges up and downstream of the EAC separation. In the north of the domain, the EAC is most coherent, whereas in the south, the EAC is already separated from the coast and eddies largely dominate the circulation; particularly within the middle and outer shelf. The inner shelf circulation on the other hand, is less affected by the EAC meandering and separation, allowing a coherent along-shelf flow within the inner shelf from Seal Rocks to Sydney.

3.5.1 Circulation Variability

The spatial pattern of the two-year mean surface flow field reveals the path of the EAC (Fig. 3.1). Upstream of Seal Rocks (32.5ºS), velocities between the coast and the 200 m isobath follow the direction of the isobaths closely. Nevertheless, the EAC interacts with the shelf and also influences the flow. Large velocities observed closer to the coast push water southeastwards, eventually separating from the coast and transporting water cross-isobaths and offshore. The large velocities in this section concur with a coherent and intensified EAC at 31.8ºS due to a narrowing of the shelf (Schaeffer et al., 2015), and with the patterns revealed by geostrophic velocities, which show the fastest flow within 32 to 33.5ºS (Chapter 1). In addition, downstream of the EAC separation from the coast, velocities have been shown to become weaker and more

variable in nature (Schaeffer et al., 2015; Wood et al., 2016). This is in agreement with the results of this chapter, which show a 30% decrease in magnitude of the flow offshore the 200 m isobath within the southern part of the domain, as well as an increase in the flow variability south of 33.5ºS, downstream of typical EAC separation latitudes (Fig.3.1).

Overall, the spatial and temporal patterns of the EOF modes on the shelf corroborate the influence of the EAC and its eddies on the shelf's variability. Results evidence that they divide the shelf circulation regimes up and downstream the EAC, with most of the impact on the middle and outer shelf and little impact on the inner shelf. The temporal evolution of the EOF mode 1 reveals the seasonal signal (Fig.3.10, e) with positive values during summer, confirming the strengthening of the poleward flowing EAC, and negative values during Autumn/Winter, when the EAC typically separates farther north and velocities are weakened (Godfrey et al., 1980; Hamon et al., 1975; Ridgway and Godfrey, 1997). Furthermore, peaks at the mesoscale frequency band for mode 1 and 2 (124 and 93 days) (Fig. 3.10, f) also confirms the regular spawning of eddies from the current as seen in modeled data by Gibbs et al. (2000); Mata et al. (2006) and Wilkin and Zhang (2007).

3.5.2 Transport Variability

3.5.2.1 Along-Shelf transport

Although along-shelf transport has previously been estimated on the east coast of Australia, using long-term mooring arrays (Sloyan et al. 2016) and coarser resolution models (Ridgway et al., 2007; Cetina-Heredia et al. 2014, Kerry et al., 2016), this study is the first attempt to investigate the along-shelf transport variability with outputs of a high-resolution model (750 m) across different sections on the shelf. Results demonstrated that the overall mean along-shelf transport on the shelf is poleward in accordance to the knowledge of the circulation in the study area. An interesting pattern emerged by investigating the along-shelf transport across the inner (0-100 m), middle (100-200 m) and outer shelf sections (200-2000 m) (Fig. 3.13). At Seal Rocks, the along-shelf transport increases from the coast offshore towards the core of the EAC (Fig. 3.13,

top row) whereas across Sydney the opposite pattern is observed with weakening magnitudes from the coast offshore (Fig. 3.13, bottom row). Standard deviations of along-shelf transport are of the same order of magnitude than the mean off Seal Rocks, but more than double at Newcastle and Sydney, implying that along-shelf flow reversals are more common at regions were the EAC has already separated from the coast. According to these results, the circulation off Sydney is dominated by a different regime compared to that dominating off Seal Rocks. Specifically, a meandering EAC and frequently spawned anti-cyclonic eddies lead to a much more variable flow pattern off Sydney.

Furthermore, the circulation differs latitudinally and longitudinally up and downstream of the EAC separation zone, highlighting the influence of the meandering EAC on the overall shelf dynamics. For example, periodicities extracted from along-shelf transport on the inner shelf are different to periodicities found on the middle and outer shelf; particularly for Seal Rocks and Newcastle. Peaks within the mesoscale band (93-124 days, Fig. 3.10, f) are present on the middle and outer shelf, emphasizing the impact of the EAC dynamics outside the 100 m isobaths. These periodicities correspond to the mesoscale eddy shedding by the EAC south of its separation, periodic encroachments onto the shelf, and the meandering of the EAC jet found by Bowen et al. (2005); Mata et al. (2000, 2006). The inner shelf however, has dominant periodicities of 9-45 days, elucidating influence of the weather band (Fig. 3.15, a-c).

From north (Seal Rocks) to south (Sydney), along-shelf transport on the inner shelf is significantly correlated. This suggests that the inner shelf is dominated by other mechanisms rather than the influence of the EACs large-scale meandering and separation. Since dominant periodicities of along-shelf transport on the inner-shelf are within the weather band, it is speculated that wind forcing is a key driver of the inner shelf circulation. This assumption is based on the fact that the surface boundary layer, which is affected by wind stress, constitutes a large proportion of the water column in these shallow regions (Lentz, 2001). This result agrees well with previous research done on inner shelf dynamics (Allen and Smith, 1981). A study by Archer et al. (2017), confirms the influence of the wind on the inner shelf variability upstream of the Hawkesbury shelf off Coffs Harbour (at a mooring located 70 m offshore), whereas further offshore, the EAC encroachment on the shelf is shown to play a more important role in the circulation variability. Tranter et al. (1986) showed that eddies and meanders can be located within 90 km of the shelf break off Sydney, supporting the findings that the EAC impacts the

outer shelf regions. Off Sydney, close to the shelf break boundary at the 140 m isobath, observed temperature and velocity data highlight that the EACs seasonal signal is responsible for only 6% of the overall variability (Wood et al., 2016).

3.5.2.2 Cross-Shelf Transport

Offshore transport on the Hawkesbury shelf is closely related with the path of the EAC and particularly with its separation, which carries water offshore from inside the 200 m isobath across the slope/open ocean boundary (2000 m isobath) and into deeper water between 32 - 33.2°S (the northern section of the domain S1x, Fig. 3.14). This section coincides with the latitudinal range where the EAC separates within the Hawkesbury Shelf (Fig. 3.18); specifically, the EAC separates within the northern section off Seal Rocks (S1x) ~40% of the time. The EAC separation also occurs ~40% of the time in the middle section of the domain (S2x); however, the offshore transport associated with these events occurs mostly further offshore (west of the 2000m isobath) in a region that is not encompassed by the model. Thus, within the shelf (from the coast to the 2000m isobath) most of the offshore transport is constrained to the northern section between 32.5 and 33.2°S. Due to strong offshore movement where the EAC separates, onshore movement of water through the bottom boundary layer and up the slope may be induced resulting in upwelling events on the shelf (Schaeffer et al., 2013). This can be seen especially during winter periods off Seal Rocks, where the HSM shows onshore movement across the shelf break (Fig. 3.9).

Although much less consistent, offshore transport also occurs through the 200 and 2000 m isobaths in the middle section encompassing Newcastle (S2x) and Sydney (S3x).

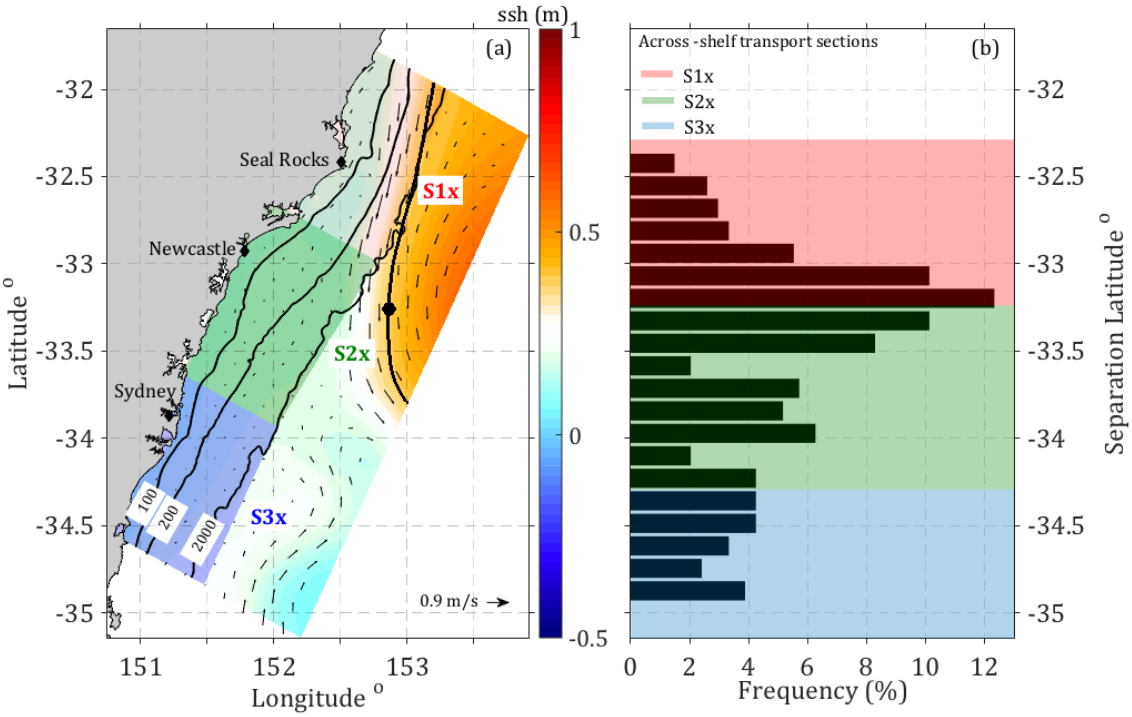

Fig. 3.18. (a) Snapshot of Sea Surface Height showing the corresponding SSH isoline used to identify the EAC separation (black line and black dot respectively). Arrows present the surface flow field and solid lines show the isobath (100, 200 and 2000 m). (b) Frequency histogram of the EAC separation latitude calculated within the study domain. The shaded regions in both panels (pink, green, and blue) correspond to the cross-shelf transport regions shown in Fig. 3.13.

In regions downstream of the EAC separation, onshore transport dominates the inner shelf region (Fig. 3.14). Further offshore, a much more variable pattern emerges with offshore transport across the mid and outer shelf (Fig. 3.14). Moreover, the onshore movement of water at depth off Newcastle and Sydney is coherent with depth and agrees with upwelling processes induced by the EAC separation and eddy encroachment, resulting in strong onshore transport (Fig. 3.14).

Periodicities of cross-shelf transport at all transects have strong peaks corresponding to the eddy frequency (93-124 days) across the 200 and 2000 m isobath, while no considerable peaks are visible across the 100 m isobath. Peaks in cross-shelf transport off Seal Rocks exhibit the weakest power at the eddy periodicity (93-124 days), particularly across the shelf//slope boundary at the 2000m isobath. In contrast, off Sydney, the power associated with the eddy frequency is at its strongest. On the inner

shelf however, the cross-shelf transport has no visible peak at the eddy frequency, suggesting that the inner shelf remains fairly unaffected by mesoscale eddies. This pattern is most likely the result of the EAC meandering on and off the shelf, its separation from the coast and resulting eddy field, creating different regimes on the shelf. For example, the circulation off Seal Rocks, in the northern part of the domain, is characterised by an intense along-shelf flow associated with a coherent EAC not being separated from the coast yet, leading to a weak eddy periodicity. Sydney on the other hand is positioned in the southern part of the domain, where the EAC is often already separated from the coast and eddies drive the cross-shelf transport.

3.5.2.2 Transport Budget

The transport budget reveals the major regions of shelf exchange. Most poleward transport occurs offshore close to the center of the EAC jet in the northern part of the domain (Seal Rocks). The northern domain encompasses a region where the EAC separates from the coast promoting transport of water offshore throughout the water column. Once the EAC has separated from the coast, poleward transport drops 1/3 in magnitude. Strongest onshore transport is found in the southern domain, within the Sydney box (Fig. 3.15). The onshore transport in the southern domain is likely to be driven by eddies, known to be consistently spawned by the EAC meandering (Gibbs et al., 2000; Mata et al., 2006; Cetina-Heredia et al., 2014).

3.6 Summary

In this chapter, the 3D mean circulation, current, and transport variability on the Hawkesbury shelf has been investigated. The overall mean circulation is dominated by the poleward flowing EAC with maximum velocities found offshore of the shelf break. Cross-shelf flows on the other hand are 50% weaker in magnitude than along-shelf flows. Results that are presented here reveal new features of the shelf circulation that have previously not been documented.

The chapter findings confirm that the EAC separation from the coast creates different dynamical regimes within the middle and offshore sections of the shelf. Downstream of the separation, a meandering EAC and the frequent encroachments of eddies lead to a much more variable flow pattern offshore of Sydney and Newcastle compared to upstream at Seal Rocks, where the circulation is dominated by coherent poleward flowing EAC. The inner shelf regions (between the coast and the 100m isobath) however, are less affected by the EACs meandering and are most likely wind driven.

The mean cross-shelf transport across the 2000 m isobath (*i.e.* the shelf/slope boundary) implies that the region between 32°S – 33°S (encompassing Seal Rocks) is the major site for shelf water export into the open ocean. Offshore transport occurs throughout the water column, coherent with the depth of the EAC (Ridgway and Dunn, 2003; Sloyan et al., 2016). Further south, off Newcastle and Sydney, the cross-shore transport is highly variable with standard deviations generally larger than the mean.

This work provides an ideal framework for the upcoming chapter, which uses transport pathways to diagnose the source regions of water for the Hawkesbury Shelf.

Chapter 4

Water Transport Pathways along the Hawkesbury shelf: Quantifying the Source of Water delivered to Sydney's offshore Artificial Reef

4.1 Introduction

4.1.1 Artificial Reefs

Demands of growing coastal populations and the rise in anthropogenic influence greatly degrades the health of adjacent coastal ecosystems. Their close proximity to urban centres makes them not only vulnerable to terrestrial runoff and pollution, but also impacted by commercial and recreational fishing opportunities (White et al., 1990). To relieve the pressure put on natural reef habitats and local fish stocks, artificial reefs are deployed worldwide to enhance recreational fishing opportunities for the adjacent urban centres. Their purpose is to promote the productivity of marine ecosystems and therefore attracting a larger fish assemblage. Forms of artificial reefs included materials of opportunity such as scuttled ships, tires, marine debris (Baine, 2001) and decommissioned oil rigs (Macreadie et al., 2011; Claisse et al., 2015). These reefs and also designed reefs or "purpose-built" artificial reefs have been extensively used in both Japan and Taiwan to substantially enhance coastal fish production (White et al., 1990). In fact, over 9% of the Japanese coastline contains artificial reefs placed at depths less

than 200 m (Thierry, 1988). Taiwan followed a similar trend and deployed 358 concrete blocks in the waters off Linbien in 1957 (Chen and Chen, 1957), and south Korea.

In Australia, artificial reefs were previously made from a variety of materials of opportunity including concrete pipes, decommissioned vessels and even 40,000 un-ballasted tires (Branden et al., 1994). As part of an integrated approach to fishery enhancement, there has been an emphasis on designing reefs as fish habitats (Becker et al., 2017). Designed artificial reefs are fundamentally different to scuttled ships or dumped materials of opportunity in resembling fish habitat. They are designed to increase the surface area of reef space and add spaces throughout the water column to provide shelter for the attachment of benthos and attracts a diversity of producers such as zooplankton and various fish species (Seaman and Jensen, 2000; Smith et al., 2016; Truong et al., 2017). Benthic invertebrates such as bivalves, crustaceans, tunicates and especially planktivorous fish, are known to use reefs as shelter and feed on plankton (Alldredge and King, 2009; Champion et al., 2015).

In 2007, the Department of Primary Fishers in New South Wales (NSW) proposed a plan to design a series of large offshore artificial reefs off 3 major metropolitan locations (Newcastle (32.9°S), Sydney (33.9°S) and Wollongong (34.4°S)). In 2011, Australia's first specifically designed offshore artificial reef (OAR) was deployed 1.2 km off the coast of Sydney, NSW, Australia (33.9°S). Since then, new clusters of designed reefs have been deployed off Port Macquarie (31.4°S), South Sydney (34.1°S) and Shoalhaven Heads (34.9°S), (Fig. 4.1, a).

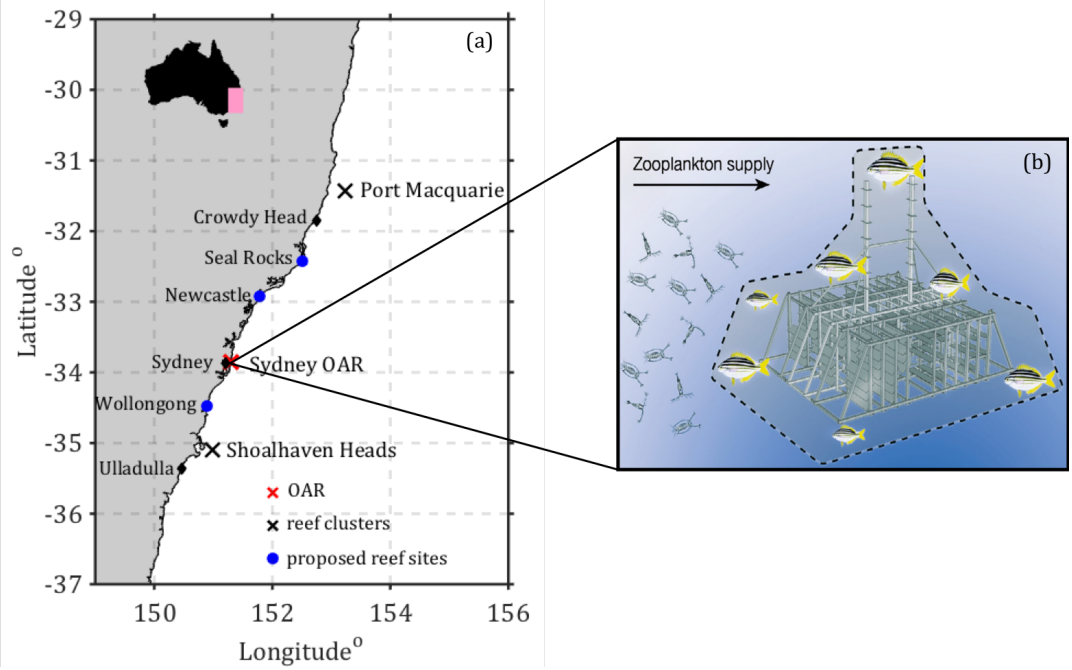

Fig. 4.1. Position of existing and future artificial reefs placements along the NSW coast. Reef structure of the Sydney OAR is shown in (b) (Figure of reef structure by Champion et al., 2015).

4.1.2 Biological Oceanography of Artificial Reefs

The ability of artificial reefs to provide productive fisheries reef habitats, relies on the delivery of plankton. In particular, the delivery of zooplankton, which constitutes the link between primary producers and higher trophic levels (Champion et al., 2015, Truong et al., 2017), is key for an increase of fish assemblages in reefs. Zooplankton abundance fluctuates greatly throughout the ocean, with high abundances in the shallow coastal ocean and low abundances in adjacent offshore waters. Although offshore waters are not always oligotrophic, high concentrations in nutrients often occur at depth below the euphotic zone; thus, phytoplankton and zooplankton growth is not triggered until the deep nutrient rich water is uplifted (Brink, 2016). The uplift of deep nutrient rich water often occurs in coastal regions through wind driven, or current driven upwelling. These events force the movement of offshore water upwards over the continental slope; by delivering nutrients into the euphotic zone they facilitate phytoplankton growth making the coastal waters abundant in zooplankton (Mongin et al., 2011).

The preferred placements for artificial reefs is near ports and in the vicinity of natural reefs. Because fish inhabiting reefs feed on plankton, water flowing across adjacent artificial reefs can be depleted of zooplankton minimizing the likelihood of downstream reefs to receive zooplankton and become habitats with increased fish assemblages. Champion et al. (2015) estimated the depletion of zooplankton using a series of numerical studies of an artificial reef off Sydney, located on the southeast coast of Australia, in response to mean currents. With the natural reef habitat being 600 m away, they found that only ~0.5% of the zooplankton is depleted from waters flowing over a 12 m wide reef with mean velocity of 0.091 m s^{-1}. This percentage however increases significantly the longer the zooplankton is exposed to the reef habitat (*e.g.* due to slower flow or a larger reef). Under conditions of slowest current velocity (0.042 ms^{-1}), zooplankton depletion occurs after only 40 m of reef exposure with mesoscale depletion starting after more than 200 m of exposure (Champion et al., 2015).

Given that local currents control transport pathways of water carrying zooplankton, as well as their exposure to reefs and consequent degree of zooplankton depletion, the physical oceanographic setting is an important component for the productivity and sustainability of artificial reefs. Therefore, identifying the source regions of water reaching continental shelves could greatly benefit the selection of locations for efficient artificial reefs. Specifically, elucidating if water comes from: 1) offshore deep waters with the potential to deliver nutrients into the euphotic zone and trigger productivity (*e.g.* phytoplankton and subsequent zooplankton growth), and 2) from coastal regions where reef's biota can potentially deplete zooplankton, would aid identifying specific locations within the shelf likely to receive waters that can enhance fish assemblages.

A useful tool to investigate the transport pathways of particles to artificial reefs in space and time, is Lagrangian particle tracking (Roughan et al., 2003; Roughan et al., 2011). Passive particles can be used to represent plankton (*e.g.* zookplankton), water or other tracers) in order to identify likely dispersal pathways throughout different circulation patterns to highlight the impact of oceanographic variability in driving the dispersal from source regions (Werner et al., 2007).

Along southeast Australia, the overall zooplankton production has been shown to be most influenced by the mesoscale western boundary current system (the EAC and its eddy field) along with its seasonal variability (Armbrecht et al., 2013, 2015.). The

circulation along the shelf off southeast Australia is strongly poleward dominated. with a seasonal signal indicating more intense velocities in austral summer (September through January) than in winter (Ridgway and Godfrey, 1997; Wood et al., 2016). The latitudes at which the EAC separates most frequently from the coast fluctuates between 33 - 33.5ºS within the Hawkesbury Shelf model (HSM). Separation dynamics of the EAC and eddy field control ~70% of the mesoscale variability in the region as shown through empirical orthogonal function analysis (EOF) of surface velocity fields (Chapter 3). The separation dynamics dominate more the outer shelf regions (offshore of the 100 m isobath), whereas the inner shelf regions remain largely unaffected by the meandering nature of the EAC. It follows that source waters vary with variable oceanographic conditions, making it important to elucidate how variability (*e.g*. seasonality) will affect water pathways.

4.2 Aims and Objectives

The overarching aim of this chapter is to provide the detailed physical oceanographic setting of the OAR, as well as the oceanographic context for other artificial reefs along southeast Australia (Fig. 4.1). More specifically, this chapter identifies regions of possible zooplankton sources of artificial reefs along the Hawkesbury Shelf to understand whether upstream consumption (depletion) of zooplankton is likely. This study begins by exploring the circulation variability (seasonal) on the shelf and its impact on particle trajectory pathways released at the OAR according to timeframes relevant to the zooplankton generation cycle (7-21 days). The source and pathways of particles released across the shelf are investigated through Lagrangian particle experiments. Velocity outputs from the high-resolution hydrodynamic model (HSM), configured and validated in Chapter 2, are used to run the Lagrangian particle backtracking.

The specific aims are:

1. Determine how major circulation patterns and seasonality affect water parcel trajectories on the shelf.

2. Determine the origin of water (depth and region) that flows over the shelf and the Sydney OAR.

3. Understand the implications of the identified water sources on the potential productivity of artificial reefs placed within the Hawkesbury Bioregion.

4.3. Methods

4.3.1 Offshore Artificial Reef Location and Study Site

The offshore artificial reef (OAR) is placed 1.2 km off the coast of Sydney, NSW, Australia (33° 50.797' S, 151° 17.988' E; Fig. 4.1, 4.2). The OAR is a 15 by 12 m steel structure placed on the bottom of the ocean at a water depth of 38 m. The structure extends to a height of 12 m above the bottom and includes 8 m tall towers (Scott et al., 2015). The study region is located south of the typical EAC separation zone (30.7 to 32.4ºS, Cetina-Heredia et al., 2014) encompassing the productive Hawkesbury Shelf between 31.5-34.5ºS (Fig. 4.2).

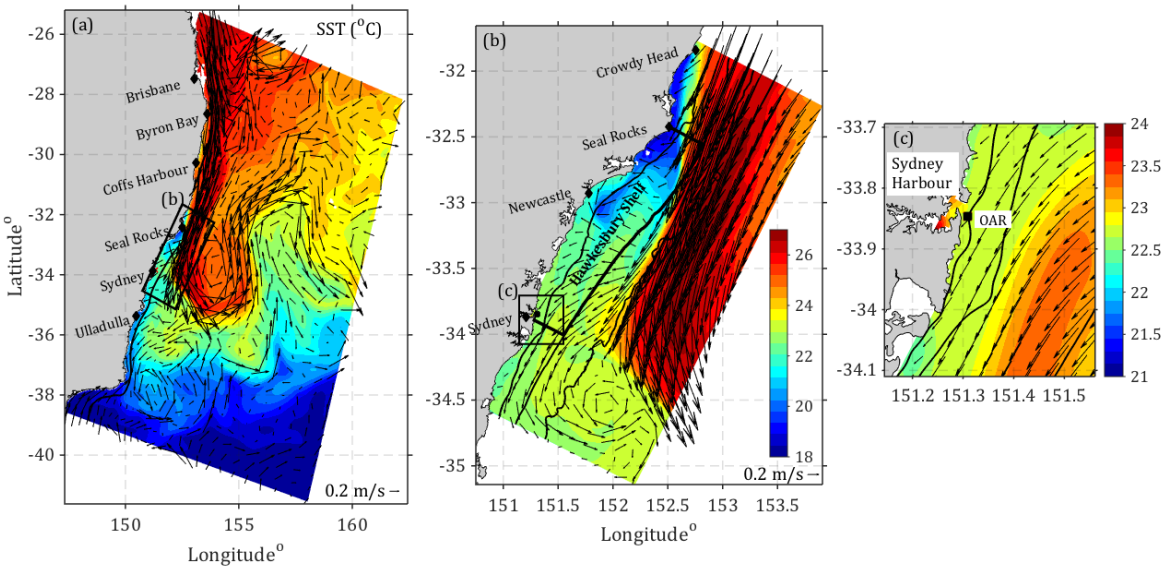

Fig. 4.2. Study area and reef location: (a) Map of the study area in eastern Australia as shown by the EAC model domain (b) and the high-resolution HSM model(c) location of the Sydney OAR shown by the black square. The Sea Surface Temperature (ºC) is shown in colour, arrows indicate surface velocities (9th Jan 2013). In (b) black solid lines indicate

the 100, 200 and 2000 m isobaths, in (c) they indicate the 4 0, 100 and 200 m isobath respectively.

4.3.2 Lagrangian Trajectory Model

Lagrangian trajectories (pathways) of particles delivered to the OAR were assessed through particle trajectory modelling. Particles were advected offline using the Connectivity Modelling System (CMS) (Paris et al., 2013) by employing a fourth order Runge-Kutta scheme to velocity outputs (3D) obtained from the high-resolution hydrodynamic model (HSM).

Temperature, salinity and velocity outputs were converted from the ROMS sigma co-ordinate grid to a regular z-level grid for compatibility with CMS using 62 vertical layers. A variable resolution for the conversion to z-level was used with 2 m in upper 40 m to 10 m between 40 and 400 m and then increased to 100 m from 400 until the bottom). This resolution was justified since the interest was mainly focused on shelf scales to depths of 200 m. In order to parameterize flow at scales finer than the HSM model (750 m) a horizontal diffusivity coefficient of 0.416 $m^2\ s^{-1}$ following Okubo (1971) was implemented. The method by Okubo has previously been used to successfully run a 10 km resolution CMS simulation with a diffusion coefficient of 8.8 $m^2\ s^{-1}$ by Cetina-Heredia et al. (2015). Two types of Lagrangian tracking experiments were conducted.

The first experiment revealed the origin and trajectories of particles delivered to the OAR over the preceding 21 days before reaching the OAR. Particles were seeded at the OAR and tracked backwards to determine the possible source location of zooplankton. Particles were continuously released at the OAR and throughout the water column, at 2 m depth intervals (Fig. 4.3), and at 2-hourly intervals.

For the second experiment, the origin of water reaching the continental shelf was identified to make possible implications which shelf regions receive offshore or inshore waters, hence making them upwelling favorable (and more productive).

In this scenario, particles were released from the coastline out to the 100 m isobath throughout the model domain (31.5°S to 34.5°S). They were released every 5th along-shelf (3.75 km) and every 3rd across-shelf (2.25 km) grid cell, with a depth interval of every 5 m through the water column from the surface to 50 m and then every 10 m (50 m and deeper) at 2-hourly intervals. The positions of all particles (*i.e.* latitude, longitude and depth) were recorded every 6 hours for the two-year simulation period from 2012-

2013. All particles were then tracked backwards for 21 days each month between January 1, 2012 and December 30, 2013.

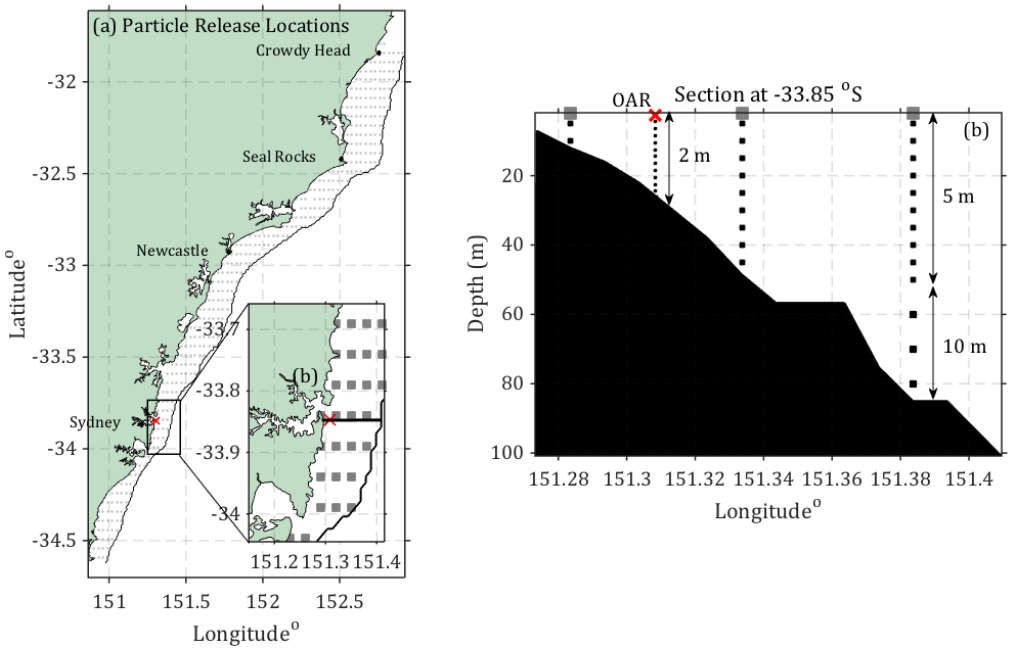

Fig. 4.3. Particle release locations: (a) Surface map of particle release locations. Grey squares show the release sites from the coast to the 100 m isobath. The red cross indicates the OAR release site (b) OAR release locations across the shelf with depth. Particles are released in 2 m intervals from the surface to the bottom at the OAR. For shelf regions, every 5 m from the surface to 50 m, and 10 m from 50 down to 400 m and deeper than 400 m every 100 m.

4.3.3 Water Source Diagnosis on the Shelf

To investigate the origin of particles delivered to the OAR over each of the relevant timescales (7,14, 21 days), probability density maps were constructed using the backward trajectories from the Lagrangian simulations. These maps represented the probability that a particle will pass a location over the 21-day time period expressed as a percentage of the total number of particles released. It followed that a high value indicates a greater percentage of particles crossing the grid box over the specified timeframe (Mitarai et al., 2009). The main rationale underlying these maps is to account for differences in particle densities along the coast that might arose throughout the 21-day timeframe. The same analyses were repeated for each location across the shelf.

To explore the impact of seasonal variability on the origin of particles delivered to the OAR, probability density maps were constructed for each season and over each of the relevant timescales. To further understand the impact of the circulation variability, particle trajectories for periods of dominating EOF modes 1-3 were used for the density maps. Periods were chosen based on the principal component analysis (PC) for Modes 1-3 obtained from the EOF analysis of daily averaged surface velocity fields from Dec 2011 to Dec 2013 (details of the analysis are found in Chapter 1). Composites of trajectories longer than 7 days were used during periods when the absolute amplitude of each mode is dominant.

Simulation trajectory outputs for the 4 seasons as follows:

1) Summer:
- 1 Jan 2012 to 29 Feb 2012;
- 1 Dec 2012 to 29 Feb 2013 and
- 1 Dec 2013 to 31 Dec 2013

2) Autumn:
- 1 Mar 2012 to 31 May 2012 and
- 1 Mar 2013 to 31 May 2013

3) Winter:
- 1 June 2012 to 31 Aug 2012 and
- 1 June 2013 to 31 Aug 2013

4) Spring:
- 1 Sep 2012 to 30 Nov 2012 and
- 1 Sep 2013 to 30 Nov 2013

To further understand the origin of particles reaching the OAR, their position (longitude and latitude) at 7, 14 and 21 days prior to arriving at the reef was recorded. The distance from the reef to the particle end point (or starting point since this is based on backtracking time steps) was calculated. The backtracked trajectories were assessed using the straight-line (linear) distance (L), as well as the distance travelled along the

trajectory path (T). Both distances were grouped in 30 km bins and results were shown in stacked histograms. In addition, the ratio between the linear distance of particles to the OAR and the distance along the trajectory path gave a useful indication if particles were transported directly or indirectly to the reef (*i.e.* in a straight line or along a meandering path). A ratio L/T~1 indicated linear advection, where particles travel approximately along a straight path. This could possibly hint to wind driven shelf flow or the poleward flowing EAC. A ration L/T << 1 indicate particles were advected along a non-linear pathway and suggesting the possible entrainment in a cyclonic or anti-cyclonic eddy.

The location of particles throughout the water column at time of its origin, aided in understanding if particles might have been upwelled or downwelled. Therefore, depth readings of all particles released throughout the water column at the OAR were logged at exactly 7, 14 and 21 days prior to the release date. This implied that changes in depth along the trajectory path were not taken into account. Results were binned into depth ranges (10 m bins) and illustrated by using histograms. The same analyses was repeated for each location adjacent to the coast.

To broaden the study and include shelf regions up and downstream of the current deployed OAR, locations across the entire shelf that were most likely to receive water from inner (coast-50 m), middle (50-100 m) or offshore (100-deeper) regions were identified. For this purpose, particles were released across the shelf (out to the 100 m isobath) along the coast ranging from 31.5-34.5°S. The percentage of particles found in each of the shelf regions was then determined at 7, 14 and 21 days prior to reaching the shelf. This analysis was also conducted for the OAR individually. Moreover, to highlight the amount of time particles spent in each of the shelf sections, the number of time steps a particle spends within a shelf section were counted. Results for both the across-shelf distribution of source waters and the time spent in each region, were explained using histograms.

4.4 Results

4.4.1 Source Regions of Particles reaching the OAR

Particles released and backtracked at the OAR over the relevant time periods of 7-21 days, illustrated most particle trajectories reaching the OAR itself were sourced from regions in close proximity to the OAR. Although they could also originate up to hundreds of kilometers away (Fig. 4.4), both upstream and downstream. While poleward advection dominated, the across-shelf dispersion of source regions was mostly confined by the 100 m isobath. More specifically, 21 days prior to reaching the reef, the along-shelf dispersion of source regions was maximum with water originating from up to 112 km upstream of the OAR. This distance became smaller with shorter timescales. 14 days prior to reaching the reef, the along-shelf dispersion of source regions decreases southward by 29 km to 85 km. Along shelf dispersion was minimum after 7 days prior to the release date, decreasing 30 km southwards, with the cloud of highest particle density expanding 55 km to north and 27 km to the south of the OAR. The dispersion of source regions also revealed variations in the across-shelf direction. 21 days prior to reaching the OAR, the origin of particles was extended offshore of the 200 m isobath, while 14 days prior, the origin of particles was spread just outside the 100 m isobath. 7 days before reaching the reef, the 100 m isobath confined the cloud of highest particle density.

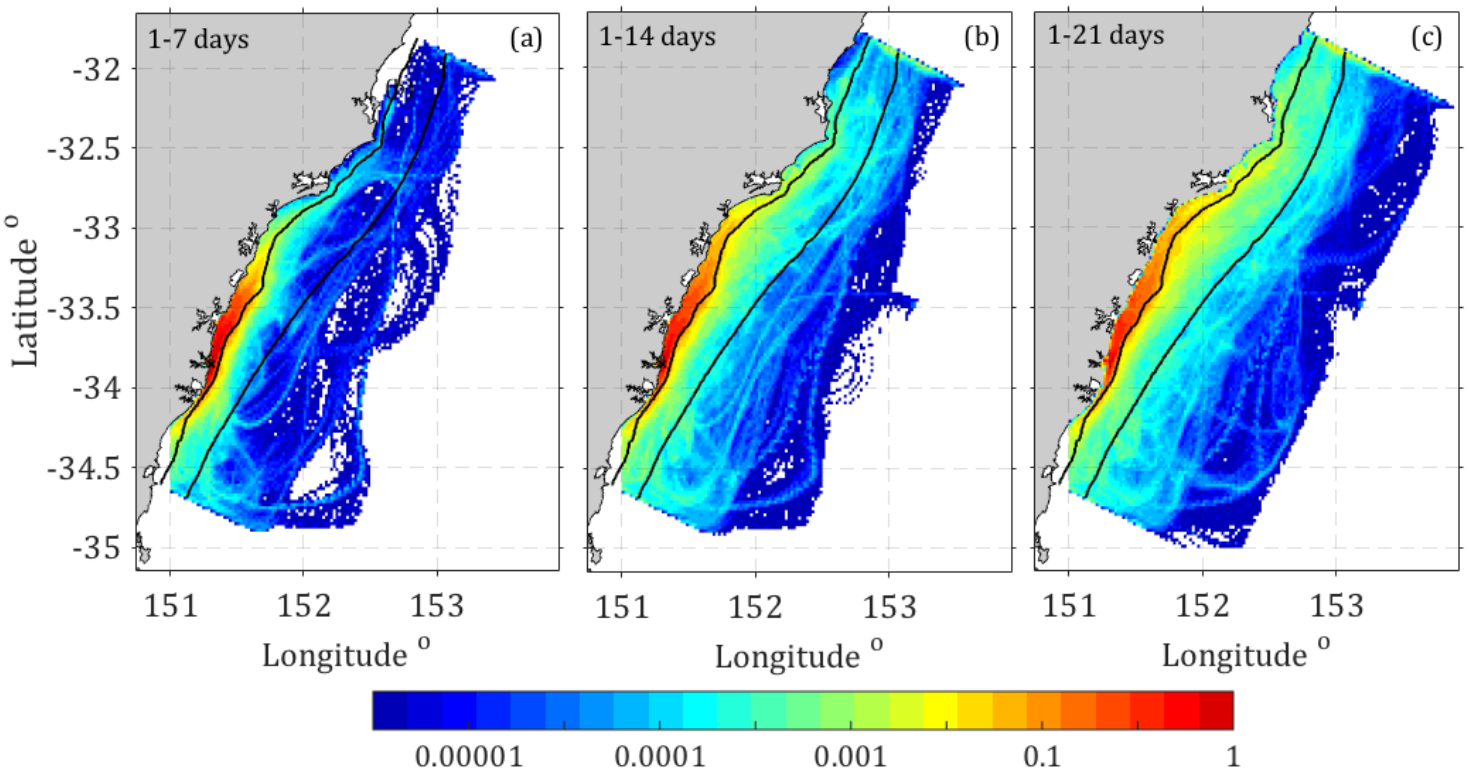

Fig. 4.4. Particle dispersion within the 21-day frame illustrated through probability density maps (logarithmic scale, percentage of particles %). Particles are released and backtracked at the OAR (represented as the black cross). Trajectories over a period of (a) 1-7 days, (b) 1-14 days, (c) 1-21 days. The black solid lines indicate the 100 and 200 m continental shelf isobath respectively.

4.4.2 Effects of Variability on Particle Trajectories (water transport pathways)

The seasonal circulation variability had little impact on the high-density cloud along the inner shelf region, where most of the particles reaching the OAR originated from (Fig. 4.5). Nevertheless, the along-shelf dispersion of the density cloud showed a greater spread (almost twice as fast) during the summer period compared to autumn, winter and spring. Within the 21-day frame, the dispersion cloud of highest particle density (dark orange colour in Fig. 4.5) covered a region of 109 km in summer, compared to 30 km in autumn, 29 km in winter and 50 km in spring. It also has to be added that the southward coverage of the highest density cloud was the least pronounced during the spring period.

As opposed to the along-shelf dominance seen throughout the inner shelf region, offshore or peripheral regions of the particle dispersion, reflected the EAC's seasonal variability with dispersion in the lateral (offshore) direction in autumn and winter.

Since no grid cells contained more than 1% of the of the particles, isolines along a region that covered grid cells with a probability of 1% for each season, highlighted the along-shelf spread inside the inner shelf with little lateral extension (Fig. 4.6). The peripheral isolines confirmed the dispersion in the lateral (offshore) direction in autumn and winter as seen in the associated probability density maps.

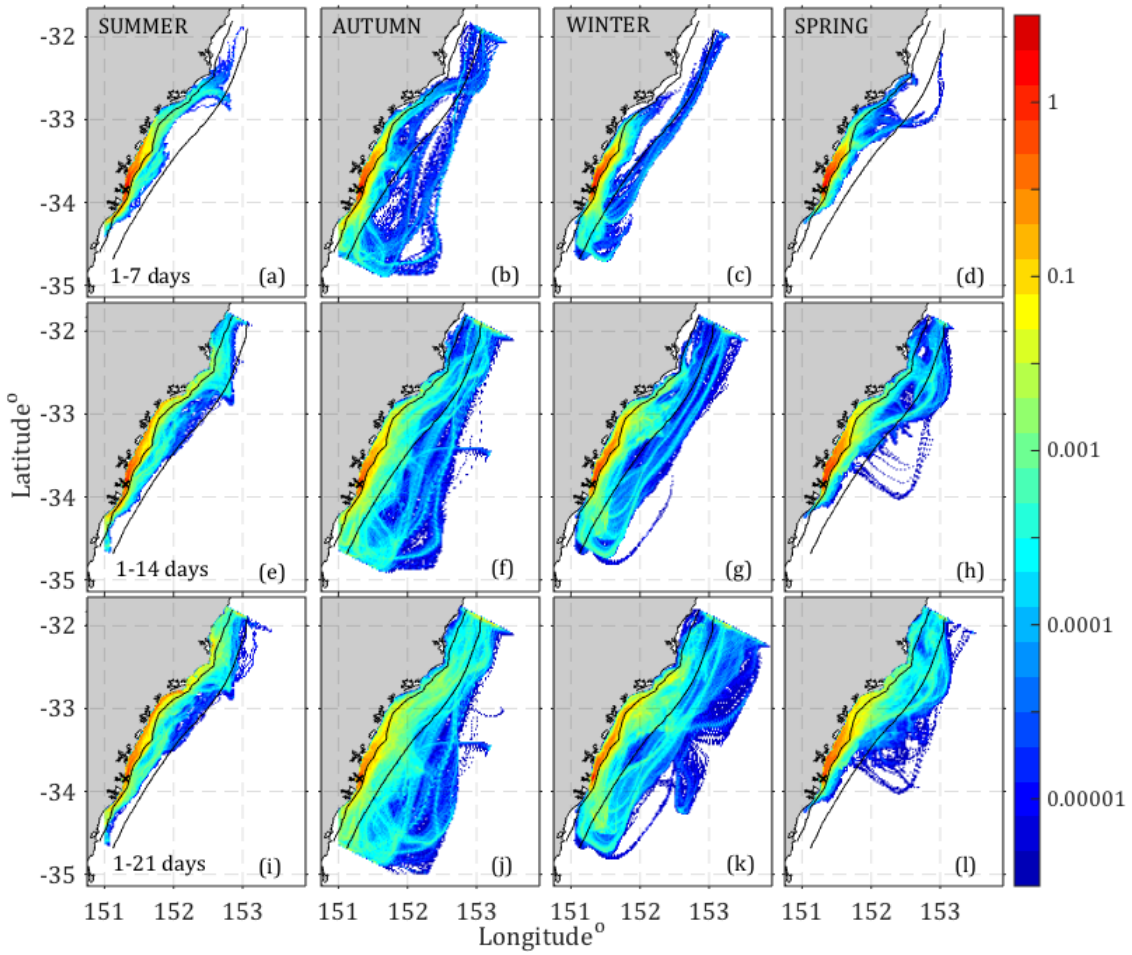

Fig. 4.5. Particle dispersion within the 21-day frame illustrated through probability density maps (logarithmic scale, percentage of particles %). Particles are released and backtracked at the OAR (represented as the black cross). Each column presents a different season. Trajectories over a period of (a-d) 1-7 days, (e-h) 1-14 days, (i-l) 1-21 days. The black solid lines indicate the 100 and 200 m continental shelf isobath respectively.

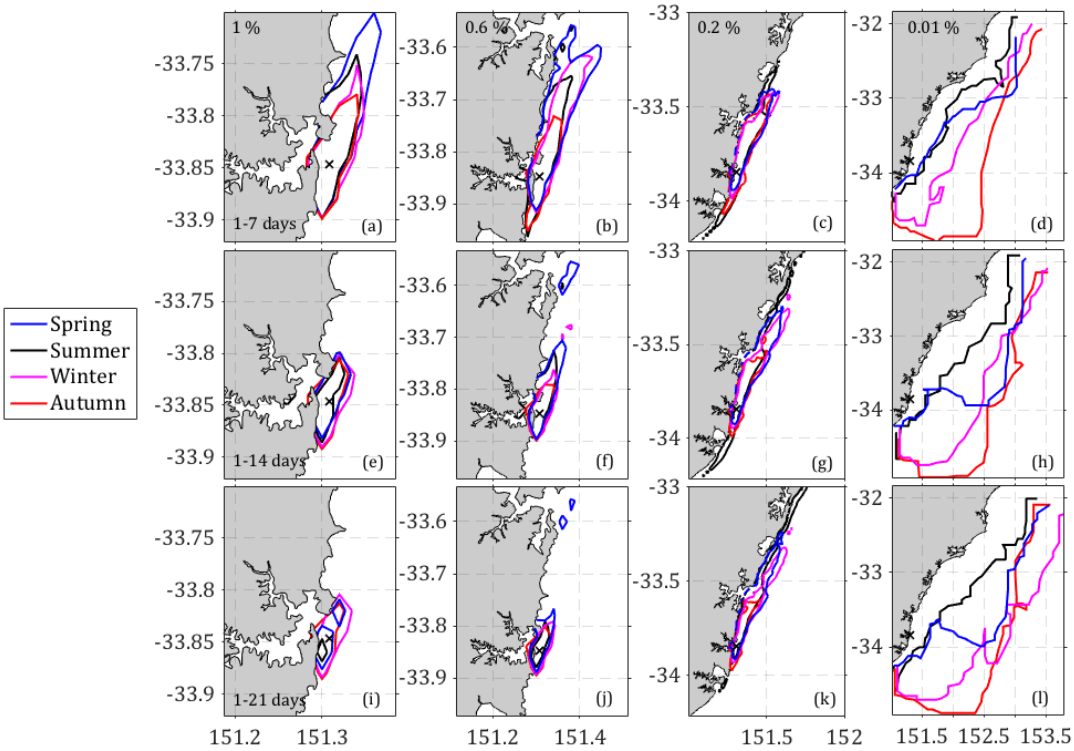

Fig. 4.6. Probability density contours (%). Particles are released and backtracked at the OAR (represented as the black cross). Shown are the isolines characterizing the grid cells with 1%, 0.6 %, 0.2 and 0.01% probability. Trajectories over a period of (a-d) 1-7 days, (e-h) 1-14 days, (i-l) 1-21 days. The black solid lines indicate the 100 and 200 m continental shelf isobath respectively. Each colour represents a different season.

The dominant modes of variability as identified in Chapter 2, confirmed the dominance of along-shelf dispersal along the inner shelf region. As described in the methods section, trajectories were based on composites consisting of periods longer than 7 days when EOF modes 1-3 were dominant. Mean velocity fields for mode 1 showed a small variability inside the 100 m isobath with largest variations following the shelf break at the 200 m isobath and eventually turning east into deeper regions between 33 and 33.5°S. Within the 21-day time frame, the particles dispersed 30 km in the along-shelf direction and extended from the inner shelf out to the shelf break at the 200 m isobath (Fig. 4.7)

Mode 2 was characterized by a less variable flow outside the shelf break and an even weaker variability was found along the inner shelf. The particle dispersion along the inner revealed a coverage of 52 km within the 21-day timeframe and a greater offshore spread in the peripheral particles. The mean velocity field representing Mode 3 on the other hand, exhibited the highest variability of inner shelf flow extending out to the 200

m isobath. Particle dispersions displayed a high variability in the offshore direction exposing the northward evolution of an eddy present observed outside the 200 m isobath. Thus, the main difference between dispersal patterns throughout the EOF modes 1-3 was the offshore extent of particles and the clear presence of eddy variability seen in mode 3.

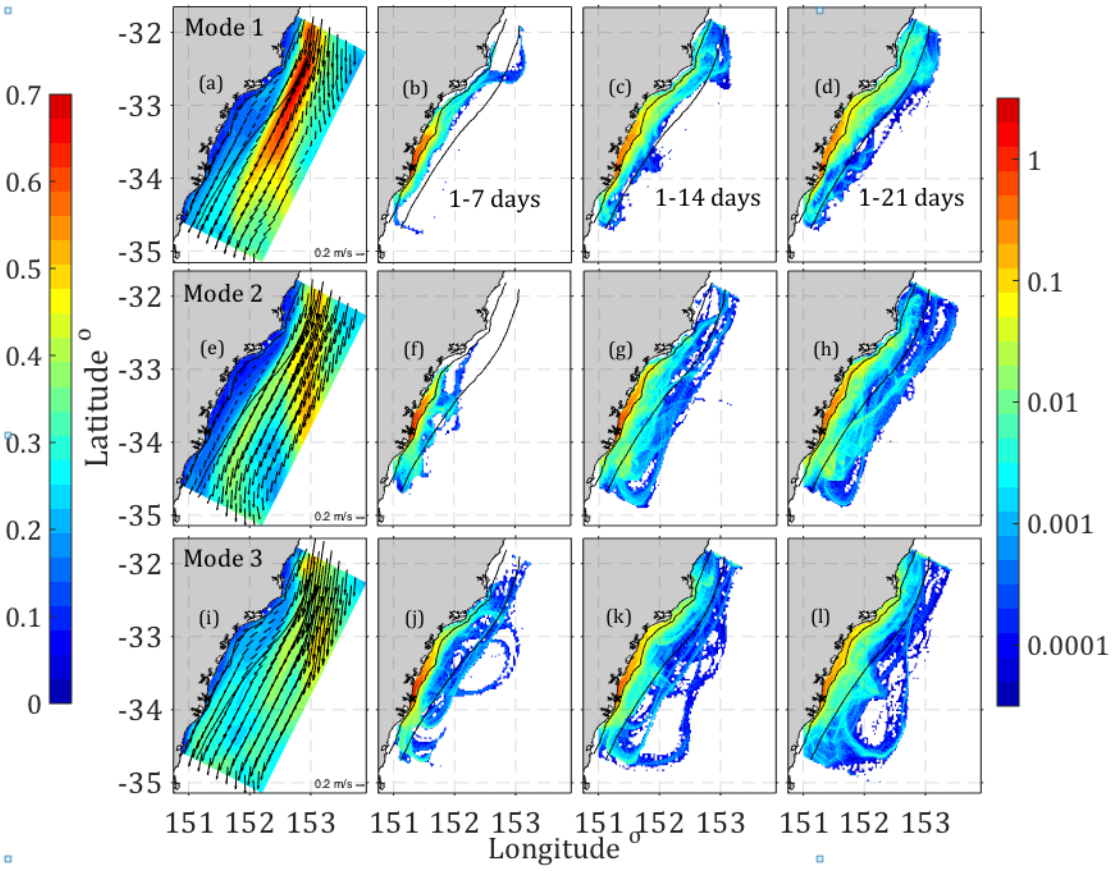

Fig 4.7. Mean velocity fields for time periods of dominating EOF modes 1-3 (a,e,i). Colour contours represent standard deviations of speed (m s^{-1}). Probability density maps are shown for a single release site (OAR, represented as the black cross, as shown in Fig. 2.1), based on the backtracking trajectories over a period of 1-7 days (b,f,j), 1-14 days (c,g,k) and 1-21 days (d,h,l). Shown is the spatial distribution of particles using the backward simulations of the particle tracking model (CMS). The black solid lines indicate the 100 m and 200 m continental shelf isobath respectively.

4.4.3 Distance travelled

The linear distance particles travelled after being released 21 days prior to reaching the OAR, ranges between 90-120 km (Fig. 4.8). That distance was considerably less for particles being backtracked for 7 days only, reaching a maximum distance between 30-60 km to the OAR. By following the particle along its trajectory path, distances travelled increased by more than 50% with the majority of particles covering a distance between 200-250 km, 21 days prior to reaching the OAR. The shortest distance particles covered prior to arriving at the OAR was after being backtracked for 7 days with a total distance of 50-100 km. The overall maximum distance of all particles released has been recorded to exceed 450 km.

In this 21-day time frame, only 11% of the particles had a L/T ratio between 0.75 and 1 after being backtracked for 21 days. The percentage increased to 23% after being backtracked for14 days and to 40% after being backtracked for only 7 days (Fig. 4.8 c). This ratio indicated that the linear distance was close to the total distance travelled along the trajectories, suggesting the particles went along a relatively straight path. Particles started to deviate from a presumed straight path the longer it was backtracked after the initial release date.

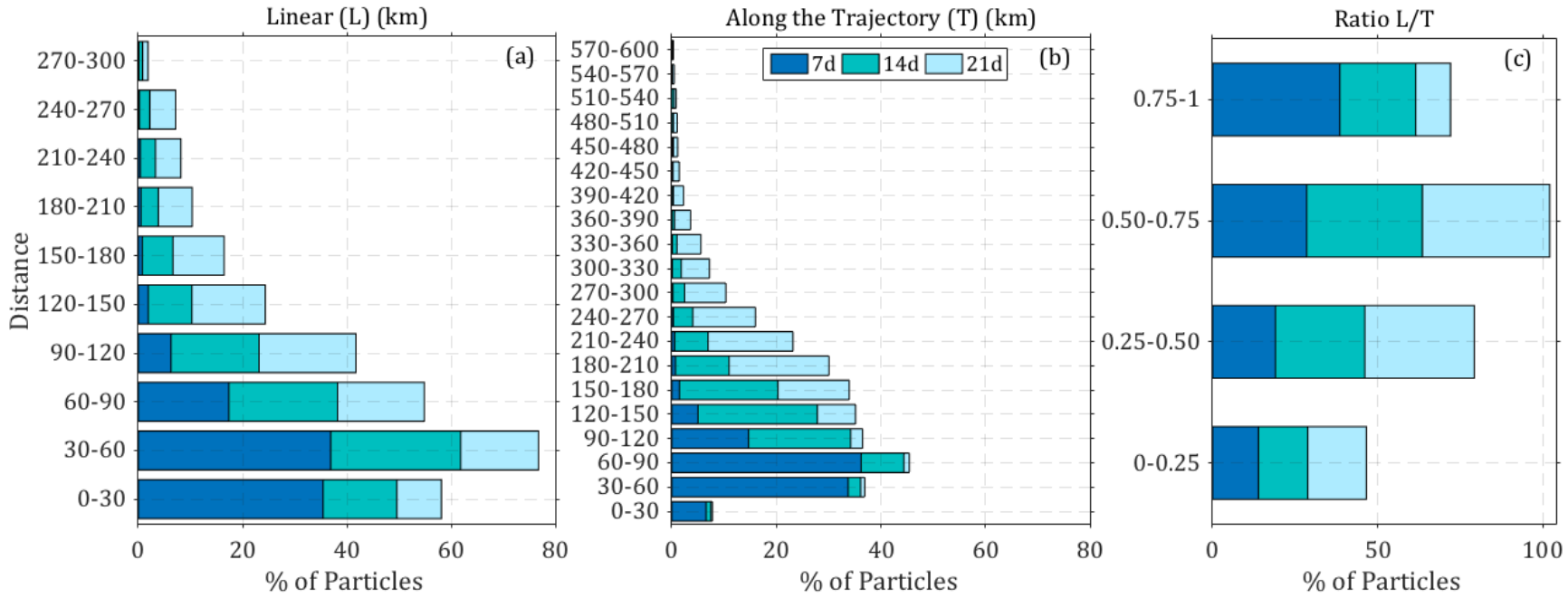

Fig. 4.8. Distance of particles to the OAR 7, 14 and 21 days prior to release date. Histograms are stacked. (a) Linear, (b) along the trajectory, (c) Ratio between Linear and Trajectory distance.

4.4.3 Water Source Diagnosis on the Shelf

4.4.3.1 Source Location (Vertical)

Vertical distributions of particles depths 7, 14 and 21 days prior to arriving at the OAR. Changes in depth along the trajectory were neglected in this analysis. 21, 14 and 7 days before release date at the reef, the majority (~ 50%) of the particles arrived from a depth shallower than 10 m (Fig. 4.9). Even though most particles originated at shallow depths, a fraction of ~2% came from depths as deep as 100 m (even for short 7-day backward trajectories, Fig. 4.9).

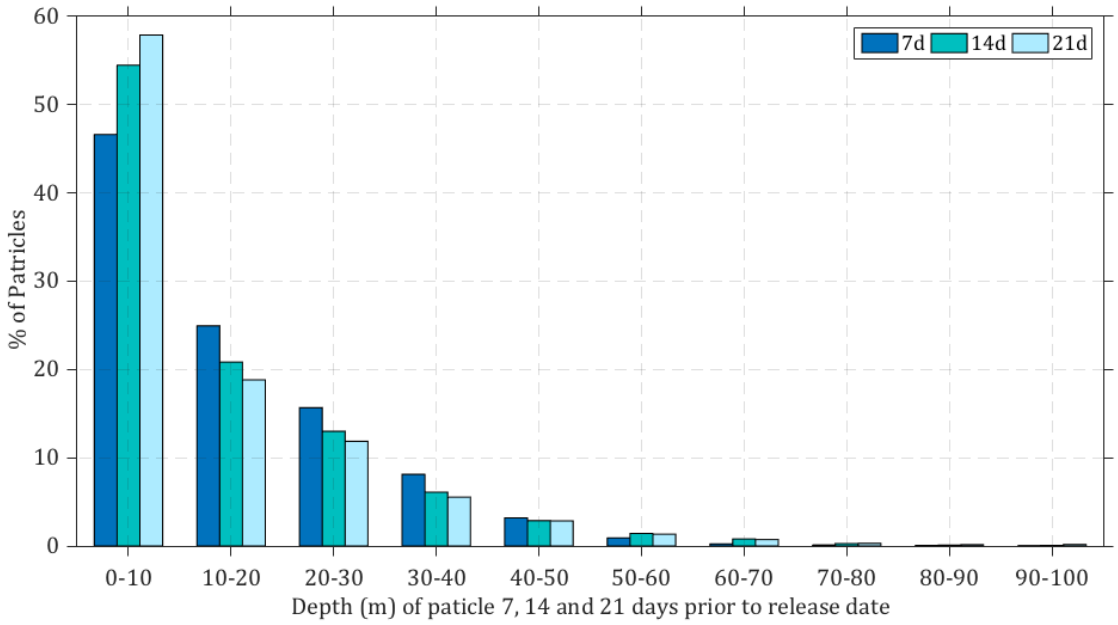

Fig. 4.9. Depth range of particles 7,14 and 21 days prior to release date.

Particles were released in 2 m intervals throughout the upper 40 m of the water column, and their tendency to be upwelled or downwelled depending on their release depth was illustrated in Fig. 4.10. Particles released at depths between 28.5 m (close to the bottom) and 16.5 m below the surface, were upwelled within the 21-day frame. Particularly, particles released at 28.5 m and backtracked for 21 days, showed a mean upward displacement of 12 m, and a 7 m upward displacement after being backtracked for 7 days. Particles released at between the surface down to 16.5 m highlighted their tendency to be downwelled along the trajectory. At a 6.5 m release depth, particles have

a mean downward displacement of 4 m after being backtracked for 21 days, decreasing to 2 m after 7 days.

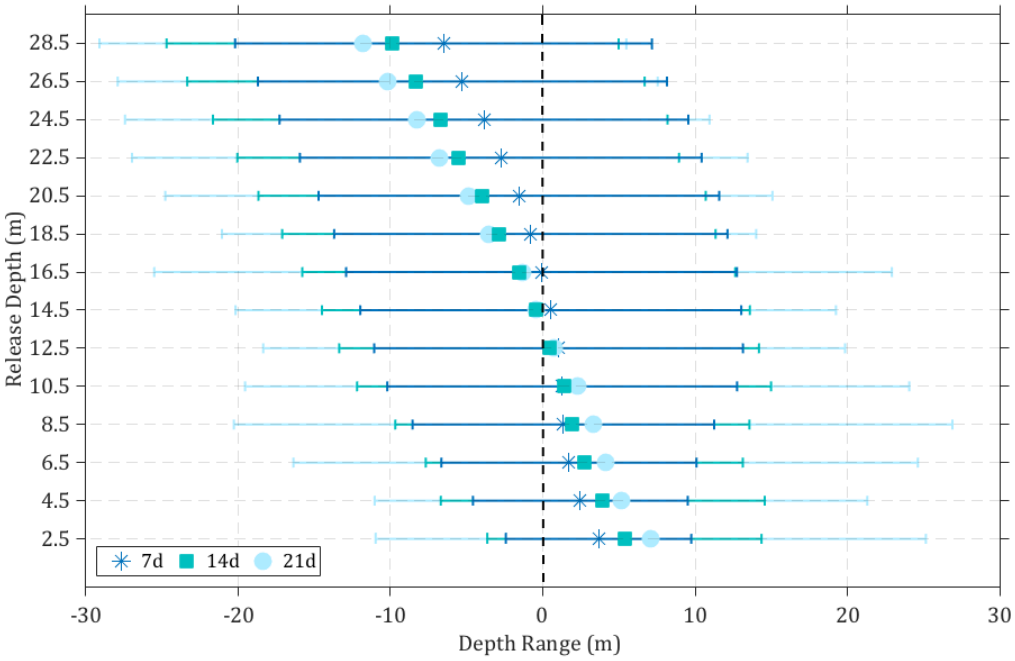

Fig. 4.10. Mean depth ranges of particles at each release depth through the water column.

To investigate regions along the entire coast, which receive waters from shallow or deeper regions throughout the water column, depths of particles at 7, 14 and 21 days prior to arriving at the coast were explored in Fig. 4.11. In a small region between 31.7 and 31.8°S particles arriving at the coast were mainly from deeper depths with 50% originated at depths up to 60 m. Further south (32 and 32.25°S), coastal locations received mainly water from shallow depths where 70% originated at depths of up to 10 m. Further south, between 33 and 33.5°S, the distribution became more variable with 70% of particles emerging from depths less than 10 m. Downstream, between 33.8 and 34.5°S, 50% of particles were sourced from depths ranging between 20-70 m.

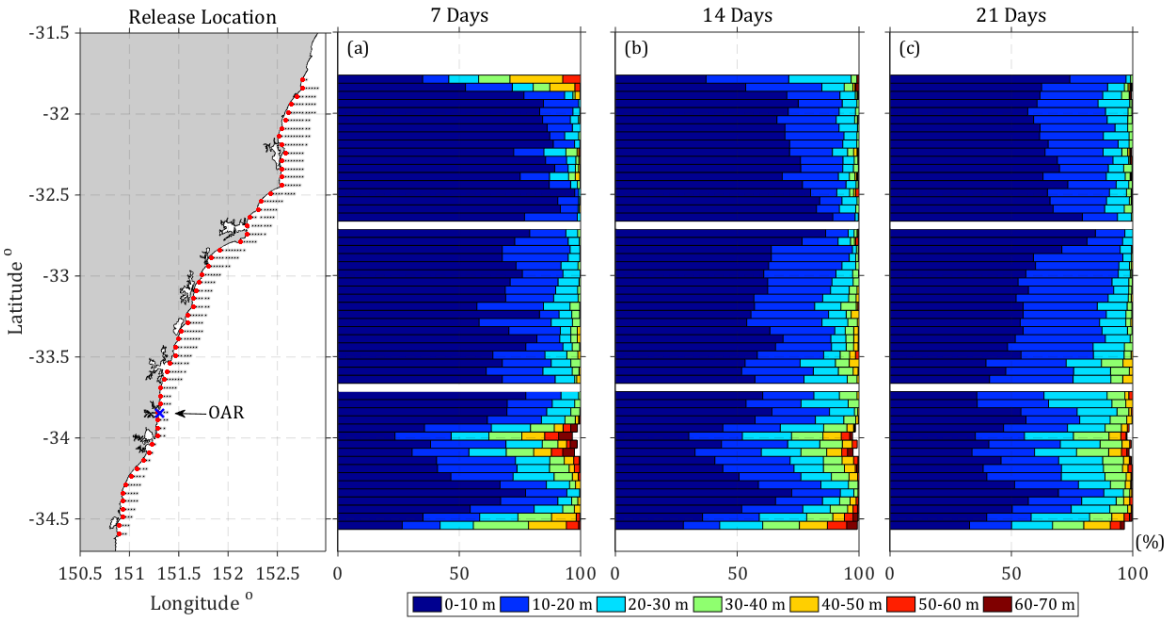

Fig. 4.11. Different colors indicate the water column depth ranges from which the particle came from 7,14 and 21 days prior to the release date.

4.4.3.2 Source Location (Horizontal)

4.4.3.2.1 OAR releases

Particles that reached the OAR over the 21-day time frame revealed the shelf region in which particles were located. Additionally, they revealed the amount of time they spent in each region prior to arriving at the reef (Fig. 4.12). 21 days prior to arrival at the reef, particles were distributed fairly evenly across the shelf with 37% originating from offshore regions (offshore of the 100 m isobath), 25% from the middle shelf (50-100 m isobath) and 33% from the most inner region (from the coast out to the 50 m isobath). By exploring the distribution of particles released 14 days prior to arrival at the reef, the offshore percentage started to decline by 10% to 27%, with an increase of 7% in particles found in the inner shelf to a total of 40%. 7 days prior to arrival at the reef, only 13% of particles originated in offshore regions, whereas 54 % originated from inshore regions.

Although roughly ~ 37% of the particles originated from offshore regions over the 21-day time frame, they spent the majority of their time (56%) within the inshore region. This increases to 71% for particles backtracked for only 7 days (Fig. 4.12 d,f). The standard deviations were based on data for 2012 and 2013, revealing a variability of less than 20% within these two years.

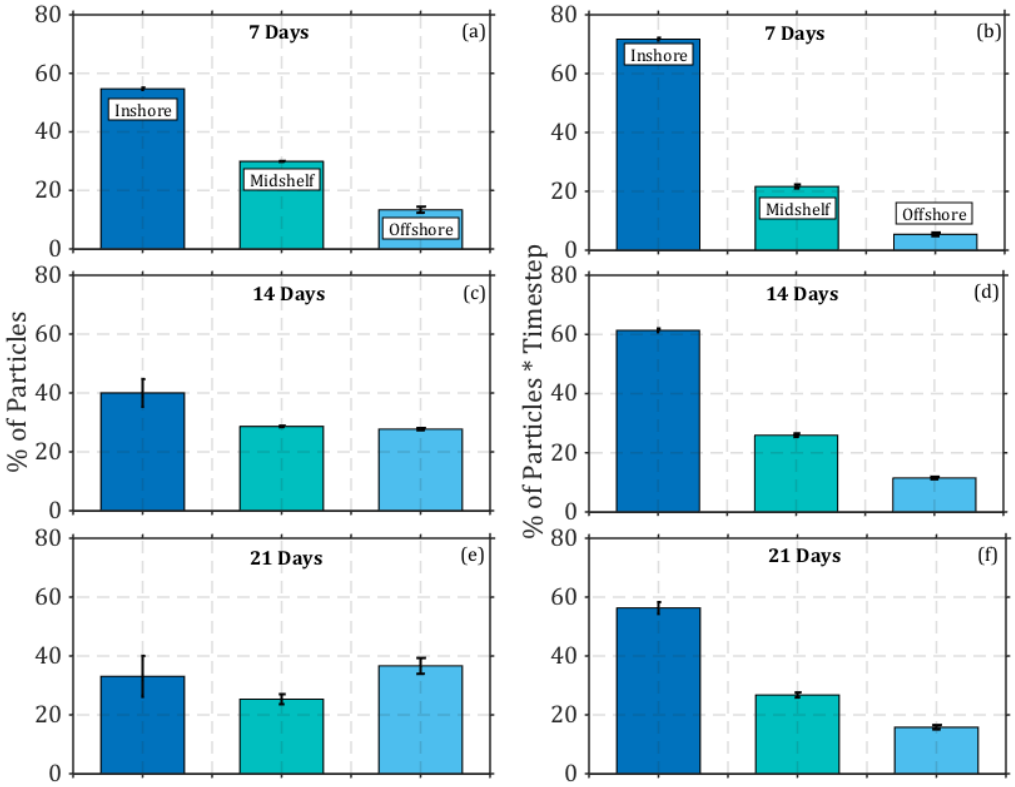

Fig. 4.12. The relative contribution from 3 possible source regions (Inshore (0-50 m), Midshelf (50-100 m) and Offshore (>100 m) for particles backtracked (a) 7 days, (c) 14 days and 21 days (e). The right column illustrates the time spent in each region before arriving at the OAR.

4.4.3.2.2 Inner and Middle Shelf Releases

Particle back-trajectories from release locations throughout the shelf, revealed that the inner shelf is the main source of water for inner shelf locations between 31.8 and 33.8°S (Fig.4.13, a). After 14-21 days, it did however start to act a source of water for the middle shelf, particularly between 31.8 and 33°S (Fig. 4.13, b, c). South of 34°S, inner shelf locations were sourced primarily by mid-shelf and offshore water (Fig. 4.14, 4.15). Mid and outer shelf regions (between 33 and 33.5°S) were predominantly sourced by offshore water (Fig. 4.15).

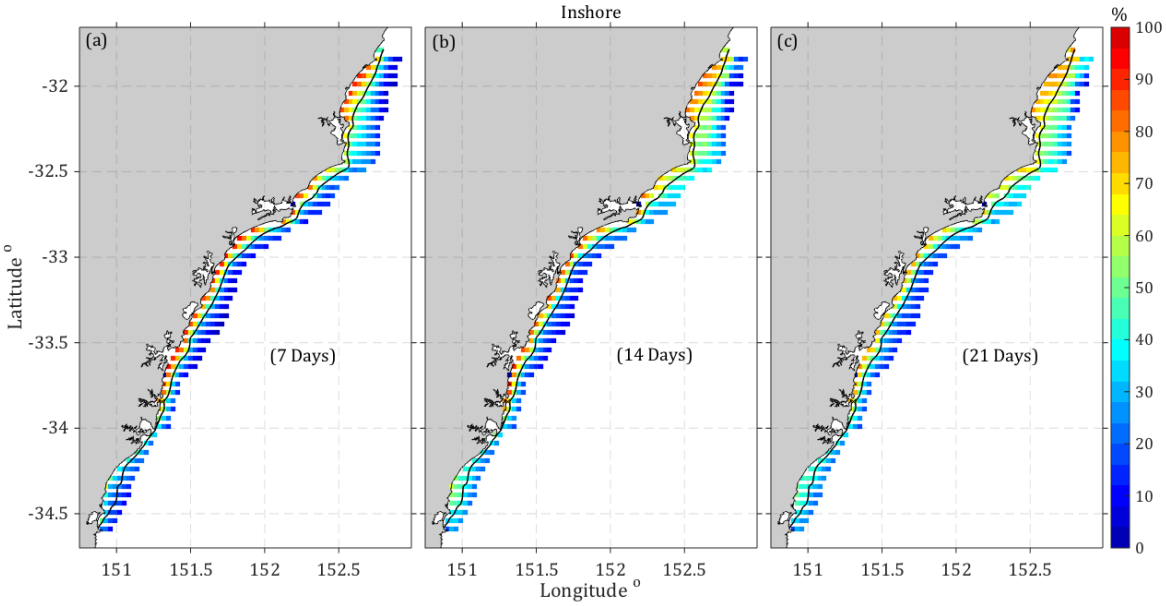

Fig. 4.13. Percentage of simulated particles released from the coast to the 100 m isobath that come from the inshore region (0-50 m). The black solid line shows the 50 m isobath.

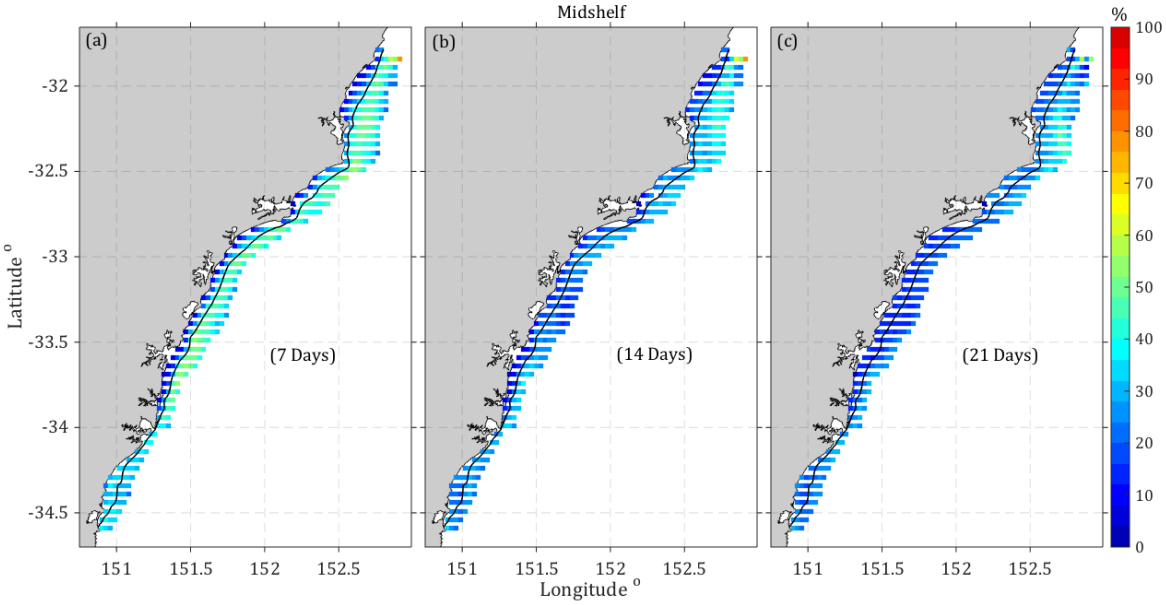

Fig. 4.14. Percentage of simulated particles released from the coast to the 100 m isobath that come from the mid-shelf region (50-100 m). The black solid line shows the 50 m isobath.

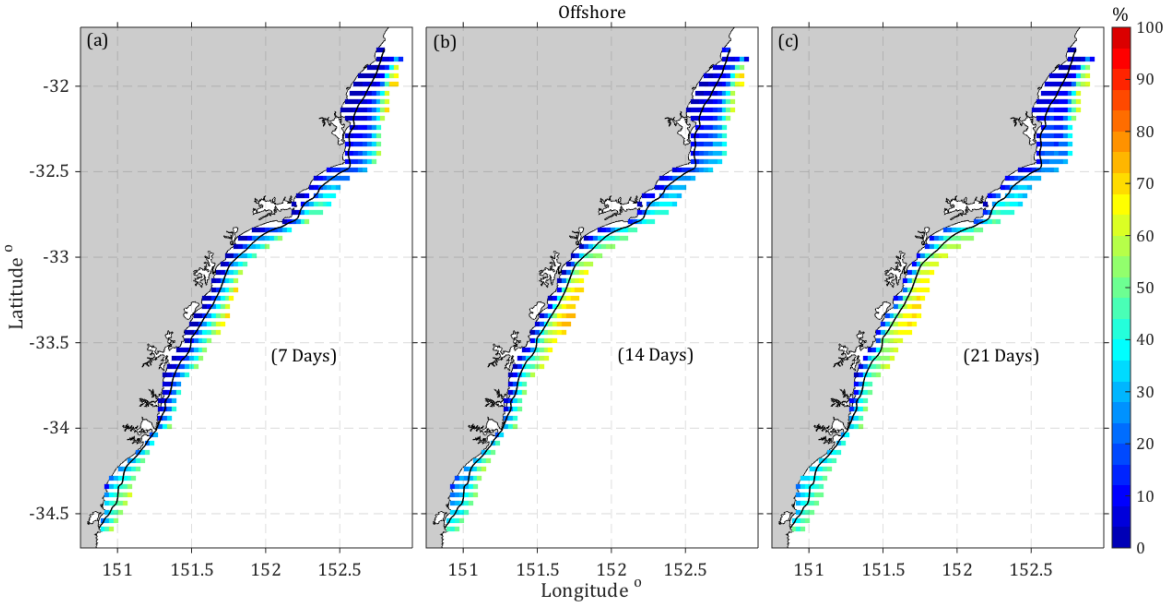

Fig. 4.15. Percentage of simulated particles released from the coast to the 100 m isobath that come from the offshore region (>100 m). The black solid line shows the 50 m isobath.

4.5 Discussion

Artificial reefs are often placed within a close proximity to the coast based on their accessibility (both for construction logistics and recreational fishing opportunities). Despite the fact that the potential for water to contain zooplankton and nutrients can vary depending on its source region, less attention has been paid to identify transport pathways connecting different oceanic regions to the shelf/coast with the artificial reefs.

This chapter provides the first study to describe the physical oceanographic setting of Sydney's offshore artificial reef (OAR) and other potential locations along the coast of southeast Australia. Lagrangian backtracking simulations are used to understand the impact of mesoscale circulation patterns on trajectories and dispersal patterns of water parcels reaching the shelf and reef.

4.5.1 Variability of the EAC driving particle trajectories

The spread of particles after being released on the inner shelf close to the 40 m isobath (the OAR, 33.9^{o}S) and backtracked over a 21-day time frame, exhibits a maximum north-south extension between Sydney and Newcastle. This infers that 21 days prior to arrival at the OAR, the majority of particles originated from the Newcastle region. The lateral spread of the highest density cloud is confined by the 100 m isobath, while peripheral regions start to spread offshore upstream of Sydney and throughout the latitudinal range where the EAC separates most frequently within the HSM (Chapter 3). This ties well with previous Lagrangian studies conducted along southeast Australia, wherein forward tracked particles released close to the 25 and 50 m isobath off Sydney experienced maximum along-shelf spreading (Roughan et al., 2011). The distribution of particles also concurs with findings highlighted in Chapter 3 which revealed the poleward dominated along-shelf transport on the inner shelf less affected by mesoscale processes of the EAC such as the meandering of the jet and encroachment of spawned eddies on the shelf and is most likely wind dominated.

As the along-shelf dispersion is strongly elongated towards the north, the southward extension (past the release site at the OAR) is minimal and is characterized by a larger offshore spread passed the 200 m isobath. The OAR is therefore less likely to be influenced by inner shelf waters from the south than from the north. The offshore spread observed south of Sydney is indicative that there is a small probability the OAR receives waters from offshore regions. The circulation off Sydney is characterized by an overall weaker but more variable poleward flow. The frequent occurrence of cold core (anticyclonic) eddies south of the separation has been shown to drive intermittent flow reversals (equatorward flow) on the shelf (Schaeffer et al., 2013; Oke and Griffin, 2011), suggesting that particles delivered to the OAR can originate from inner shelf regions northward or southward of 34^{o}S or from offshore regions. A similar conclusion was drawn by Roughan et al. (2011), showing trajectories of particles released on the inner shelf south of 34^{o}S can be advected poleward or equatorward along the shelf or pushed offshore. Even though trajectories of particles released at the OAR tend to be advected southward more quickly during summer, seasonal variability has no major impact on the source of the water reaching the OAR originates. This correlates with findings further

offshore (Wood et al., 2016), at Coffs Harbour (Latitude 31°S) and Sydney (34°S), where the EAC's variability (particularly seasonality), contributes only 6% to the overall variability. Moreover, periodicity in the shelf circulation has been attributed to encroachment of EAC eddies (with a 90 to 124-day period at 34ºS, Chapter 3) and synoptic weather patterns at the 7 to14 day period (Schaeffer et al., 2014).

Overall, the particle spread offshore is less prominent in summer than in winter and spring, where particles spread quickly offshore which is in agreement with the finding of Wood et al. (2013, 2016) who showed more variability in the flow structure during the winter months. The along-shelf spread south of Sydney is less during winter than in summer, showing the EAC separates further north during winter and spring, leading to a more variable flow downstream of the separation. The OAR has therefore a lower probability to receive waters originating south of 34ºC and particles are more likely to come from offshore regions. Overall, the pattern of the particle spread is consistent with the seasonal signal of the EAC with stronger flow intensities in summer than winter (Godfrey et al., 1980). High Frequency (HF) radar observations of surface currents at 30ºS (upstream of the EAC separation point) also supports the finding of a strengthening EAC during summer (Archer et al., 2017). Source regions on the inner shelf however, where most of the water reaching the OAR originates, is less affected by the offshore / seasonal variability.

4.5.2 Distribution of water parcels over depth and across the shelf

Throughout the simulation period, coastal regions south of the OAR received large portions of offshore waters (>100 m isobath) from depths deeper than 30 m, implying that upwelling is a persistent mechanism south of the OAR. This is directly in line with the mean onshore transport found south of the typical EAC separation zone (within the HSM domain), illustrated in Chapter 3. While coastal locations in the northern section of the domain, where the EAC has not separated yet, mainly receive water that originated upstream along the inner shelf. The EAC separation and encroachment of eddies are mechanisms responsible for bringing cooler, more nutrient water into shallow coastal areas through bottom stress induced upwelling off Sydney (Roughan and Middleton, 2002). It is therefore assumed the OAR is located within an upwelling

favorable region with high biological value, further supported by the presence of high concentration-nitrate waters off Sydney (Rossi et al.,2014; Schaeffer et al., 2015).

4.5.3 Implications for future reef placements on the shelf

By conducting Lagrangian particle release experiments it is evident that most particles (plankton) is delivered from about 90 km north of the OAR. Moreover, the placement of artificial reefs is dependent on the targeted source waters regions, delivering the plankton. Upstream of the complex and dynamic EAC separation zone, between 32°S and 33.5°S, the EAC is coherent and cross shelf exchange at is at a minimum. Reef deployment on the north coast should be south of the separation zone off Cape Byron. Reefs should avoid strong currents which may overwhelm the foraging by small fish, such as at the Port Macquarie Reef (Suthers, pers. comm). South of the separation zone (34°S), where the EAC is already detached and consistent shelf water renewal is most likely, shallow reef placements (between 30 and 50 m isobath) are sufficient to receive offshore waters (*e.g.* Shoalhaven Reefs, Fig. 4.1).

4.5.4 Modelling limitations and conclusions

The high-resolution Hawkesbury Shelf model (HSM) is well suited for this study because it has a high spatial and temporal resolution and is nested inside a lower resolution model that assimilates observations. The use of data assimilation in the parent model ensures a realistic depiction of the mesoscale flow, and thus this model provides the best possible boundary conditions. By downscaling into the coast, dynamics that are necessary in shelf areas such as tides are resolved. Further, the increased resolution ensures better representation of shelf topography and thus we can capture topographically steered velocities. Finally, the use of a high-resolution (750 m) model allows the resolution of scales that are appropriate for studying shelf processes. It was demonstrated that nesting allows mesoscale generated signals, such as the EAC and its eddy field, to be well represented in the higher-resolution model (Chapter 2).

While this work is a first step towards understanding Lagrangian pathways, further model development may provide additional insight. For example, the

development of a coupled biochemical model underpinned by this high resolution three-dimensional circulation model would allow the simulation of inner shelf biochemical processes such as nutrient phyto-zooplankton dynamics. Thus, efforts could be made towards understanding the spatial and temporal patterns of primary and secondary productivity (phytoplankton and smaller zooplankton) as well as the quantification of the flux of zooplankton in shelf waters. It follows that addressing the question of how depth of the source waters, upwelling of nutrients, or the depletion by predation during the along shore advection impacts the reefs productivity. These questions are well suited for a BGC model.

The question of reef design itself should also be taken into consideration prior to reef placements. For example, understanding the dynamics around the reef, (including purpose built versus scuttled ships) and how local circulation dynamics may impact on vertical and horizontal fluxes within the reef structure itself. Future research should examine how the nutrient content of dominant water types found on the shelf, up and downstream of the EAC separation zone, impact the biomass production and fish abundance in the vicinity of artificial reefs.

Given the parameters included, settings and assumptions used in the hydrodynamic and Lagrangian particle model, it is recommended to not only to consider economic motivations, such as proximity to a local harbour but also to regions of predominant cross-shelf exchange and upwelling, when placing artificial reefs. Moreover, attention must be given to the source of the waters within the previous 21 days which is sufficient for zooplankton production times. Ultimately, a better understanding of zooplankton abundance and delivery to artificial reefs, beneficial to estimate the sustainability of the fishing harvest.

4.6 Summary

In summary, Lagrangian particle tracking and outputs from a high-resolution circulation model (configured and validated in Chapter 2), are used to identify source waters flowing across the OAR. Results highlight the tendency of the particle dispersion to be bounded by the 100 m isobath with a dominant along-shelf orientation. The spatial

extent increases to the north throughout the zooplankton production cycle (7-21 days) and exhibits a faster spread in the along-shelf direction during the austral summer than during the rest of the seasons. The proportion of particles originating from offshore regions is highest south of the EAC separation zone, a region where periodic encroachment of eddies drives onshore transport and delivers particles from depths between 20-70 m. Regions where the EAC is coherent, onshore transport is minimal and particles arriving along the coast are mainly delivered from inshore regions. The findings showcase the impact of the EAC circulation features on particle trajectories on the mid and outer shelf, and its lessened effect on the inner shelf circulation.

Chapter 5

5.1 Summary

This final chapter summarizes the original findings and contributions of this research. A summary of the results in this thesis is presented by explicitly addressing each of the aims raised in chapters 2-4. Finally, this chapter outlines potential for future work. The results of this study revealed features of the dynamics of the Hawkesbury Shelf. The EAC is the main driver of the shelf circulation. Its meandering path impacts upon the shelf, its transport and variability. In the past, modelling studies of the region have been of insufficient resolution, too idealized and process oriented. This is the first modelling study in this region to be able to address the cross-shelf exchange on the shelf. Thus, this study makes an important contribution towards understanding the circulation of the Hawkesbury Shelf, its variability, transport dynamics and impact on an offshore, artificial reef off Sydney.

Chapter 2: Configuration and validation of the high-resolution model for the Hawkesbury Shelf (31.5-34.5^{o}S)

The configuration of the first high-resolution shelf model (HSM) of the Hawkesbury Shelf was presented. A 750 m horizontal resolution version of the Regional Ocean Modelling System (ROMS) has been configured consisting of a one – way nested domain inside a coarser (2.5-6 km resolution), eddy resolving, data assimilating ROMS model (*i.e*. EAC model). Model initial conditions and boundary forcing supplied by the EAC model and surface forcing was obtained from the ACCESS (Australian Community Climate and Earth-System Simulation) to ensure the best possible boundary conditions. The model was then used to hindcast the circulation from 2012 to 2013 to determine its mean state, variability and the major regions for water import and export on the shelf.

The specific outcomes of this chapter are summarized as follows:

1. Evaluate the model skill by comparison with observations from multiple sources (*i.e.* satellite derived and moored observations).

Comparisons against in situ velocity measurements of both the HSM and EAC reanalysis allowed us to establish that the nested model (HSM) is capable of resolving the nearshore circulation variability. This is further shown by the spatial distribution of surface temperature which corresponds well with satellite observations. These results again emphasize that the nesting was successful and offers benefits compared to the EAC reanalysis; particularly, it allows the study of processes close to the coast (within 0.75 km) such as the estimation of the flow exchange between regions throughout the continental shelf. Further comparisons of modelled and observed velocities off Sydney (34°S) reveal that the mid and outer shelf mean vertical structures are well resolved in the HSM, highlighting a consistent mean poleward flow along the isobaths.

An increase in model skill has been achieved in the nearshore region of the HSM. This can be attributed to improved representation of the bathymetric gradients across the shelf, and the inclusion of tidal forcing, making the HSM an appropriate tool to further investigate shelf dynamics.

2. Characterize the energy transfer from the meso to the submesoscale in both models through wavenumber spectra of the upper ocean.

The slopes of the energy spectra characterizing the upper ocean in the high-resolution HSM and EAC model indicate that the kinetic energy spectra for the EAC model and HSM have almost identical spectra for regions larger than $\lambda < 25$. This outcome was partially expected because both models are driven by a similar mesoscale variability induced by the EAC and are both forced with the same atmospheric forcing. However, the EAC model has weaker energy for $\lambda > 100$ km and $\lambda < 25$ km. This confirms that the higher grid resolution of the HSM contributes to more energy in the smaller scales than the EAC model.

In both grid resolutions, energy is mostly contained in the mesoscale wavenumber band, converging to a $k^{-5/3}$ shape between $50 < \lambda < 100$ km, which concurs with the

interior quasi-geostrophic theory. However, the slope rapidly steepens to follow a k^{-4} shape between $15 < \lambda < 50$ km, indicating that more energy is contained in the larger-scales. The slope of k^{-4} is associated with linear dissipation acting on all scales, instead of only at larger scales, as argued for in the two-dimensional theory. This in turn indicates that on smaller wavenumber, friction could be dominating (LaCasce et al., 2010).
Therefore, for simulations from both the EAC model and HSM, slopes are generally steeper than in other high eddy energy regions, such as the Kuroshio and Gulfstream, where KE slopes normally follow the K^{-3} (Classical interior quasi-geostrophic (QG)) to the K^{-2} law (frontogenesis) (Sasaki and Kein, 2012; Richman et al., 2012; Capet et al., 2008).

3. Investigate the mesoscale variability on the shelf in both the fine-grid inner and coarse-grid outer model by determining the dominant type of dynamic instabilities of the mean surface flow.

On the EAC dominated Hawkesbury shelf, the spatial distribution of barotropic energy transfer is captured by both the EAC and HSM model in a similar way, revealing patches of higher energies along the path of the EAC separation, where strong along-shelf velocities induce large horizontal shears. Nevertheless, the resolution downscaling from regional to coastal scales increased the magnitude of the energy transfer from mean to eddy kinetic energy suggesting stronger flow instabilities and more meanders due to a stronger mean circulation. The energy increase is most obvious along the EAC separation path characterised by patches of elevated energies. In nearshore regions, findings of higher EKE compared to MKE suggests that upwelling, vertical mixing, tides and coastline topographic effects dominate in this complex region and the impact of wind stress. Overall, the results illustrate that the high-mesoscale eddy variability detected throughout the Hawkesbury Shelf is caused by barotropic instabilities of the sheared EAC. Thus, the Hawkesbury Shelf is an area of significant barotropic instabilities.

Chapter 3: The mean circulation, variability and transport regimes of the Hawkesbury Shelf (31.5-34.5^{o}S)

The mean circulation for 2012 and 2013 on the Hawkesbury shelf was investigated along with its variability and transport regimes.

The specific outcomes of this chapter are summarized as follows:

1. Characterize the 3D circulation on the Hawkesbury Shelf for 2012-2013, its mean state and variability.

The modelled mean circulation on the Hawkesbury Shelf shows a dominant poleward flow that is strongest offshore, outside the 200 m isobath. Off Seal Rocks, the EAC is most coherent and the flow is at its maximum. Downstream of the EAC separation from the coast, velocities become weaker and more variable in nature, with a 30% decrease in magnitude outside the 200 m isobath.

The chapter findings reveal that the EAC separation greatly influences the circulation on the Hawkesbury Shelf. Downstream of the separation, a meandering EAC and the frequent encroachments of eddies onto the shelf lead to a much more variable flow pattern off Sydney and Newcastle. Upstream of the separation at Seal Rocks, the circulation is dominated by a strong coherent poleward flowing EAC. The inner shelf regions (between the coast and the 100m isobath) however, are less affected by the EAC's induced variability and are most likely wind driven.

2. Assess the transport variability on the shelf in the along and cross-shelf direction, specifically to determine the major regions for water import and export on the shelf.

The pattern of the overall two-year mean transport calculated from the coast out to the 2000 m concurs with the findings of outcome #1. Maximum along-shelf transport occurs off Seal Rocks and decreases after the separation of the EAC from the coast. Overall, the along-shelf transport is largest across Seal Rocks in the north with magnitudes of - 4.4 Sv (STD 4 Sv), coinciding with a strong and coherent EAC. Off Newcastle, the along-shelf transport shows a 30% decrease compared to Seal Rocks with a mean magnitude of - 3.1 (STD 5.7 Sv). Off Sydney, velocities exhibit a 48% decrease in magnitude with a mean of -1.6 (STD 5.6 Sv) compared to Seal Rocks. Interesting is the transport pattern across the transect off Seal Rocks, where transport magnitudes

increase from the coast towards the core of the EAC. In contrast, a reversed pattern emerges off Sydney with less transport towards the EAC core. Findings imply that the EAC separation leads to different flow regimes on the shelf.

The mean cross-shelf transport across the 2000 m isobath (*i.e.* the shelf/slope boundary) shows that the major site for shelf water export into the open ocean is between 32 - 33°S (encompassing Seal Rocks).

3. Determine the two-year mean and seasonal shelf transport budget.

The transport budget reveals a mean poleward transport on the shelf ranging from -16.1 Sv in the north (Off Seal Rocks) to -8.8 in the south (off Sydney). Cross-shelf transport is dominated by an intense offshore transport of 9.56 Sv off Seal Rocks, where the separating EAC pushes water offshore, decreasing to 5.4 Sv off Sydney.

Overall, the seasonal transport budgets are similar to the annual transport budget. A consistent poleward flow dominates across the shelf. Additionally, there is offshore flow in the northern part of the domain, where the EAC is most coherent, and a more variable onshore transport south of 33°S. Although the spatial pattern and direction of the transport is not affected by seasons, the magnitudes do exhibit seasonality; during summer, the transport values are twice as large as those during autumn and winter, particularly at the northern part of the domain, where the EAC inflow is strongest.

Chapter 4: Water transport pathways along the Hawkesbury shelf: Quantifying the source of water delivered to Sydney's offshore artificial reef

The impact of circulation variability on source waters reaching the coast and an artificial reef located off Sydney (NSW, Australia) from a mesoscale perspective was explored. It was found that the spatial extent of particle dispersal increases to the north with increasing zooplanktonic production times (7-21 days) and exhibits a faster spread in the along-shelf direction during the austral summer than during the rest of the seasons. The proportion of particles originating from offshore regions is highest south of the EAC separation zone, a region where periodic encroachment of eddies drives onshore transport and delivers particles from depths between 20-70 m. Regions where the EAC is coherent,

onshore transport is minimal and particles arriving along the coast are mainly delivered from inshore regions. Our findings elucidate the impact of the EAC circulation features on particle trajectories. The presence or absence of the EAC and its eddy encroachment dictates circulation and across-shelf transport in the Hawkesbury shelf region.

The specific outcomes of this chapter are summarized as follows:

1. Determine how the major circulation patterns and seasonality affect water parcel trajectories on the shelf and the Sydney OAR

The distribution of particles shows that most particle trajectories reaching the OAR are sourced from regions within a ~100 km distance upstream, confined by the 100 m. As the along-shelf dispersion is strongly elongated towards the north, the southward extension (past the release site at the OAR) is minimal and is characterized by a larger offshore spread passed the 200 m isobath. This reveals that poleward dominated along-shelf trajectories on the inner shelf are less affected by mesoscale processes of the EAC such as the meandering of the jet and encroachment of spawned eddies on the shelf and is most likely wind dominated, leading to a strong north-south alignment. The OAR is therefore less likely to be sourced by inner shelf waters from the south than from the north. The offshore spread observed south of Sydney is indicative that there is a small probability the OAR receives waters from offshore regions. The circulation off Sydney is characterized by an overall weaker but more variable poleward flow. The frequent occurrence of cold core (anticyclonic) eddies south of the separation has been shown to drive intermittent flow reversals, suggesting that particles delivered to the OAR can originate from inner shelf regions northward or southward of 34^{o}S or from offshore regions.

The seasonal circulation variability has little impact on the high density could along the inner shelf region, where most of the particles reaching the OAR originate from. Nevertheless, the along-shelf dispersion of the density cloud shows a greater spread (almost twice as fast) during the summer period compared to autumn, winter and spring. The southward extent of the highest density cloud is the least pronounced during the spring period. As opposed to the along-shelf dominance seen throughout the inner shelf

region, offshore or peripheral regions of the particle dispersion, do reflect the EAC's seasonal variability with dispersion in the lateral (offshore) direction in autumn and winter. The findings showcase the impact of the EAC circulation features on particle trajectories on the mid and outer shelf, and its lessened effect on the inner shelf circulation.

2. Determine the origin of water that flows over the shelf and the Sydney OAR.

Particles reaching the OAR are originate from different regions depending on the back-tracked time frame. After 21 days, particles are distributed fairly evenly across the shelf with 37% originating from offshore regions (offshore of the 100 m isobath), 25% from the middle shelf (50-100 m isobath) and 33% from the most inner region (from the coast out to the 50 m isobath). This distribution however declines after only 7 days of backtracking to only 13% of particles originating from offshore regions, while 54 % come from inshore regions.

Coastal regions south of the OAR received large portions of offshore waters (>100 m isobath) from depths deeper than 30 m. This is in line with the mean onshore transport found south of the typical EAC separation zone (within the HSM domain), illustrated in Chapter 3. While coastal locations in the northern section of the domain, where the EAC has not separated yet, mainly receive water that originated upstream along the inner shelf.

3. Discuss the implications of the identified water sources on the potential productivity of new artificial reefs to be deployed within the Hawkesbury Bioregion.

By conducting Lagrangian particle release experiments it can be seen that most water is delivered from about 90 km north of the OAR. Thus, possible implications can be made on how far to place future reefs apart. Upstream of the complex and dynamic EAC separation zone, between 32^{o}S and 33.5^{o}S, where the EAC is most coherent and cross-shelf exchange at is at a minimum, placements are recommended further offshore (between the 50-60 m isobath) to increase the likelihood to receive offshore waters and potentially avoid upstream depletion.

South of the separation zone (34^{o}S), where the EAC is already detached and consistent upwelling of offshore water is most likely, shallow reef placements (between

30 and 50 m isobath) are sufficient to receive offshore waters. The EAC separation and encroachment of eddies are mechanisms responsible for bringing cooler, more nutrient water into shallow coastal areas through bottom stress induced upwelling off Sydney (Roughan and Middleton, 2002). It is therefore assumed the OAR is located within an upwelling favorable region with high biological value, further supported by the presence of high concentration-nitrate waters off Sydney (Rossi et al., 2014; Schaeffer et al., 2015).

Up to date, much consideration has been given to proximity to a safe harbour, cost of deployment and the performance of other reefs nearby, however our results show that consideration should be given to oceanographic conditions in order to maximize productivity potential of the reef.

5.2 Suggestions for Future Work

This study on physical processes along the southeast continental shelf and slope provided a significant contribution to the understanding of current systems and transport processes in the area. The findings show the importance of field data and numerical analysis in providing a good physical base for understanding the particle dispersal distribution and transport along the shelf, which could be instrumental in studying the surface pollutant distribution in the coastal ocean.

Further research is needed to understand the physical mechanisms driving the previously described circulation patterns and also to evaluate their contribution to the total variance of the regional circulation.

In addition, the comparison between the model results and observations shows that they are consistent. However, due to the complicated nature of observed eddy-shelf interactions, it would be beneficial to make comparisons using different events to highlight the particular features contained in the observation.

It was not possible within the scope of this study to investigate the nutrient content of source waters reaching the reef and to distinguish the biological characteristics of source waters such as EAC, Tasman or coastal waters. There is a great deal of work that could be carried out on the correlation between reef productivity and nutrient content of oceanic waters reaching the reef. Meaning which source waters are most favorable for

reef productivity. Finally, useful work could also be carried out in diagnosing the impact of reef hydrodynamics and its impact in both the physical and biological aspect.

References

Alexander, M., Scott, J., Deser, C., 2000. Processes that influence sea surface Temperature and ocean mixed layer depth variability in a coupled model. Journal of Geophysical Research, 105 (16), 823–16 842.

Alldredge, A., King, J., 2009. Near-surface enrichment of zooplankton over a shallow back reef: Implications for coral reef food webs. Coral Reefs, 28, 895-908.

Allen, J., Smith, R., 1981. On the dynamics of wind-driven shelf currents, Philosophical Transactions of the Royal Society of London, Series A, 302, 617-634.

Archer, M., 2016. The Florida Current: Mean Jet Structure, Meandering, and Velocity Fluctuations Observed with HF Radar. Open Access Dissertations, 1648.

Archer, M., Keating, S., Roughan, M., Johns, W., Lumpkin, R., Beron-Vera, F., Shay, L., 2018. The kinematic similarity of two western boundary currents revealed by sustained high-resolution observations. Geophysical Research Letters, 45, 6176-6185. http://doi.org/10.1029/2018GL078429.

Archer, M., Roughan, M., Keating, S., Schaeffer, A., 2017. On the Variability of the East Australian Current: Jet Structure, Meandering, and Influence on Shelf Circulation. Journal of Geophysical Research: Oceans 122, 10.1002/2017JC013097.

Armbrecht, L., Roughan, M., Rossi, V., Schaeffer, A., Davies, P., Waite, A., Armand, L. K., 2014. Phytoplankton composition under contrasting oceanographic conditions: Upwelling and downwelling (Eastern Australia). Continental Shelf Research, 75, 54-67.

Armbrecht, L., Schaeffer, A., Roughan, M., Armand, L., 2015. Interactions between seasonality and oceanic forcing drive the phytoplankton variability in the tropical-temperate transition zone (~ 30 S) of Eastern Australia. Journal of Marine Systems, 144, 92-106.

Auclair, F., Casitas, S., Marsaleix, P., 2000. Application of an inverse method to coastal modelling. Journal of Atmospheric and Oceanic Technology, 17, 1368-1391.

Auclair, F., Estournel, C., Marsaleix, P., Pairaud, I., 2006. On coastal ocean embedded modeling. Geophysical Research Letters, 33, L14602.

Austin, 1999. The role of the alongshore wind stress in the heat budget of the North Carolina inner shelf. Journal of Geophysical Research, 104 (18), 187– 18 203.

Baine, M., 2001. Artificial reefs: a review of their design, application, management and performance. Ocean and Coastal Management, 44, 241-259.

Baldwin, M., Stephenson, D., Jolliffe, I., 2009. Spatial Weighting and Iterative Projection Methods for EOFs. Journal of Climate, 22 (2), 234-243.

Barnier, B., 1988. A numerical study on the influence of the Mid-Atlantic Ridge on nonlinear first-mode baroclinic Rossby waves generated by seasonal winds. Journal of Physical Oceanography, 18, 417– 433.

Barth, A., Alvera-Azca´rate, A., Weisberg, R., 2008. A nested model study of the Loop Current generated variability and its impact on the West Florida Shelf, Journal of Geophysical Research, 113, C05009

Becker A., Lowry, M., Taylor, M., Folpp, H., 2017. Assessment of the Sydney offshore artificial reef, NSW DPI – Fisheries Final Report Series No. 155.

Beckmann, A., Haidvogel, D., 1993. Numerical simulation of flow around a tall isolated seamount. Part I: Problem formulation and model accuracy. Journal of Physical Oceanography, 23, 1736 – 1753.

Bianchi F, Acri, F., Bernardi, A., Berton, A., Boldrin, A., Camatti, E., 2003. Can plankton communities be considered as bioindicators of water quality in the lagoon of Venice. Marine Pollution Bulletin, 46, 964-971.

Björnsson, H., Venegas, S., 1997. A Manual for EOF and SVD Analyses of Climatic Data, Feb. 1997, 52 pages. CCGCR Report No. 97-1.

Blumen, W., 1978. Uniform potential vorticity flow: part I. theory of wave interactions and two- dimensional turbulence. Journal of the Atmospheric Sciences, 35(5):774–783.

Bowen, M., Wilkin, J., Emery, W., 2005. Variability and forcing of the East Australian Current. Journal of Geophysical Research: Oceans, 110 (C3), C03019.

Brachet, S., Le Traon, P., Le Provost, C., 2004. Mesoscale variability from a high-resolution model and from altimeter data in the North Atlantic Ocean. Journal of Geophysical Research, 109, C12025.

Branden, K., Pollard, D., Reimers, H., 1994. A review of recent artificial reef developments in Australia. Bulletin of Marine Science, 55 (2-3), 982-994.

Branden, K., Pollard, D., Reimers, H., 1994. A review of recent artificial reef developments in Australia. Bulletin of Marine Science. 55 (2-3), 982-994.

Brassington, G., Summons, N., Lumpkin, R., 2011. Observed and simulated Lagrangian and eddy characteristics of the East Australian Current and the

Tasman Sea. Deep-Sea Research Part II: Topical Studies in Oceanography, 58, 559–573

Bricheno, L., Soret, A., Wolf, J., Jorba, O., Baldasano, J., 2013. Effect of high resolution meteorological forcing on nearshore wave and current model performance. Journal of Atmospheric and Oceanic Technology, 30, 1021–1037.

Brink, K., 2016. Cross-Shelf Exchange. Annual Review of Marine Science, 8, 5978.

Cailleau, S., Fedorenko, V., Barnier, B., Blayo, E., Debreu, L., 2008. Comparison of different numerical methods used to handle the open boundary of a regional ocean circulation model of the Bay of Biscay. Ocean Modelling, 25 (1-2), 1-16.

Capet, X., McWilliams, J., Molemaker, M., Shchepetkin, A., 2008a. Mesoscale to submesoscale transition in the California Current system. Part I: Flow structure, eddy flux, and observational tests. Journal of Physical Oceanography, 38(1), 29–43.

Carter, R., D'Aubrey, J., 1988. Inorganic nutrients in Natal continental shelf waters. In Coastal Ocean Studies off Natal, South Africa. Schumann, E. H. (Ed.). Berlin; Springer: 131-151 (Lecture Notes on Coastal and Estuarine Studies 26).

Cetina-Heredia, P., Roughan, M., Van Sebille, E., Coleman, M., 2014. Long-term trends in the East Australian Current separation latitude and eddy driven transport. Journal of Geophysical Research: Oceans, 119 (7), 4351-4366.

Champion, C., Suthers, I., Smith, J., 2015. Zooplanktivory is a key process for fish production on a coastal artificial reef. Marine Ecology Progress Series, 541, 1-14.

Chapman, D., 1983. On the influence of stratification and continental shelf and slope topography on the dispersion of subinertial coastally trapped waves. Journal of Physical Oceanography, 13, 1641-1652.

Charney, J., 1971. Geostrophic turbulence. Journal of the Atmospheric Sciences, 28(6),1087-1095.

Chassignet, E., Hurlburt, H., Smedstad, O., Halliwell, G., Hogan, P., Wallcraft, A., Baraille, R., Bleck, R., 2007. The HYCOM (Hybrid Coordinate Ocean Model) data assimilative system. Journal of Marine Systems, 65, 60–83.

Chen, K., He, R., 2015. Mean circulation in the coastal ocean off northeastern North America from a regional-scale ocean model. Ocean Science, 11(4), 503-517.

Chen, K., He, R., Powell, B., Gawarkiewicz, G., Moore, A., Arango, H., 2014. Data assimilative modeling investigation of Gulf Stream Warm Core Ring interaction with continental shelf and slope circulation. Journal of Geophysical Research: Oceans 119 (9), 5968–5991.

Chen, S., Chen, S., 1957. Preliminary report of artificial reefs at Linbien, Pington, China, Fishing Monthly, 51, 7-8.

Churchill, J. H., Manning, J. P., Beardsley, R. C., 2003. Slope water intrusions onto Georges Bank. J. Geophys. Res. 108 (C11), 8012.

Claisse, J., Pondella, D., Love, M., Zahn, L., Williams, C., Bull, A., 2015. Impacts from partial removal of decommissioned oil and gas platforms on fish biomass and production on the remaining platform structure and surrounding shell mounds. PLOS ONE10:e0135812.

Cresswell, G., 1994. Nutrient enrichment of the Sydney continental shelf. Marine and Freshwater Research 45 (4), 677-691.

Csanady, G., 1997. On the theories that underlie our understanding of continental shelf circulation. Journal of Physical Oceanography, 53, 207-229.

Cummins, P., Oey, L.,1983. Simulation of barotropic and baroclinic tides off northern British Columbia. Journal of Physical Oceanography, 27, 762–781.

Davis, R., deSzoeke, R., Niiler, P., 1981. Variability in the upper ocean during MILE. Part II: Modeling the mixed layer response. Deep-Sea Research, 28A, 1453–1475.

Deng, X., Grin, D., Ridgway, K., Featherstone, J., White, N., Cahill, M., 2010. Satellite altimetry for geodetic, oceanographic and climate studies in the Australian region. In: Vignudelli, S., Kostianoy, A. G., Benveniste, J. (Eds.), Coastal Altimetry, 473-508.

Djath, B., Verron, J., Melet, A., Gourdeau, L., Barnier, L., Molines J-M., 2014, Multiscale dynamical analysis of a high-resolution numerical model simulation of the Solomon Sea circulation, Journal of Geophysical Research, Oceans, 119, 6286-6304.

Egbert, G., Erofeeva, S., 2002. Efficient Inverse Modeling of Barotropic Ocean Tides, Journal of Atmospheric Oceanic Technology, 19, 183–204.

Emery, W. and Thomson, R., 1998. Data analysis methods in physical oceanography, 1st Edition. Gray Publishing, Kent.

Everett, J., Baird, M., Buchanan, P., Bulman, P., Davies, C., Downie, R., Griffiths, C., Heneghan, R., Kloser, R., Laiolo, L., Lara-Lopez, A., Lozano-Montes, H., Matear, R., McEnnulty, F., Robson, B., Rochester, W., Skerratt, H., Smith, J., Strzelecki, J., Suthers, I., Swadling, K., Ruth, P., Richardson, A., 2017. Modeling What We Sample and Sampling What We Model: Challenges for Zooplankton Model Assessment Frontiers in Marine Science, https://doi.org/10.3389/fmars.2017.00077.

Fairall, C., Bradley, E., Rogers, D., Edson, J., Young, G., 1996. Bulk parameterization of air-sea fluxes for tropical ocean-global atmosphere coupled ocean atmosphere response experiment. Journal of Geophysical Research, 101 (C2), 3747–3764.

Fairall, C., Bradley, E., Rogers, D., Edson, J., Young, G., 1996. Bulk parameterization of air-sea fluxes for tropical ocean-global atmosphere coupled ocean atmosphere response experiment. Journal of Geophysical Research, 101 (C2), 3747–3764.

Fairall, C., Hare, J., Grachev, A., Edson, J., 2003. Bulk parameterization of air–sea fluxes: Updates and verification for the COARE algorithm. Journal of Climate, 16**,** 571–59.

Falkowski, P., Flagg, C., Rowe, G., Smith, S., Whitledge, T., Wirick, C., 1988. The fate of a spring diatom bloom: Export or oxidation? Continental Shelf Research, 8, 457–484, 1988.

Fennel, K., 2010. The role of continental shelves in nitrogen and carbon cycling: Northwestern North Atlantic case study. Ocean Science, 6, 539–548.

Ferrari, R., Wunsch, C., 2009. Ocean Circulation Kinetic Energy: Reservoirs, Sources, and Sinks. Annual Review of Fluid Mechanics, 41 (1), 253-282.

Folpp H, Lowry M, Gregson M, Suthers IM (2013) Fish Assemblages on Estuarine Artificial Reefs: Natural Rocky-Reef Mimics or Discrete Assemblages? PLoS ONE 8(6): e63505.

Fringer, O., Gerritsen, M., Street, R., 2006. An unstructured-grid, finite-volume, nonhydrostatic, parallel coastal ocean simulator. Ocean Modelling, 14, 139-278.

Gan, J., Allen, J., Samelson, M., 2005. On open boundary conditions for a limited area coastal model off Oregon. Part 2: Response to wind forcing from a regional mesoscale atmospheric model, Ocean Modelling, 8, 155–173.

Ganju, N., Lentz, S., Kirincich, A., Farrar, J., 2011. Complex mean circulation over the inner shelf south of Martha's Vineyard revealed by observations and a high-resolution model. Journal of Geophysical Research, 116, C10036.

Gibbs, M. T., Middleton, J. H., Marchesiello, P., 1998. Baroclinic response of Sydney shelf waters to local wind and deep ocean forcing. Journal of Physical Oceanography 28 (2), 178-190.

Gibbs, M., Marchesiello, P., Middleton, J., 2000. Observations and simulations of a transient shelf break front over the narrow shelf at Sydney, southeastern Australia. Continental Shelf Research, 20 (7), 763-784.

Gillooly, J., 2000. Effect of body size and temperature on generation time in zooplankton. Journal of Plankton Research, 22, 241-251.

Glynn, P., 1973. Ecology of a Caribbean Reef. The Porites reef-flat biotope. II. Plankton community with evidence for depletion. Marine Biology, 22, 1-21.

Godfrey, J., 1973. On the dynamics of the western boundary current in Bryan and Cox's (1968) numerical model ocean. Deep-Sea Research, 20, 1043–1048.

Godfrey, J., Cresswell, G., Golding, T., Pearce, A., 1980. The separation of the East Australian Current. Journal of Physical Oceanography, 10, 430-440.

Gonella, J., 1972. A rotary component method for analyzing meteorological and oceanographic vector time series. Deep-Sea Research 19, 833-846.

Greenspan, H. P., 1968. The Theory of Rotating Fluids. 1st ed. Cambridge University Press, 327 pp.

Guarnieri, A., Pinardi, N., Oddo, P., Bortoluzzi, G., Ravaioli, M., 2013. Impact of tides in a baroclinic circulation model of the Adriatic Sea. Journal of Geophysical Research, 118(1), 166-183.

Haidvogel, D., Arango, H., Budgell, W., Cornuelle, B., Curchitser, E., Di Lorenzo, E., Fennel, K., Geyer, W., Hernamm, A., Lanerolle, L., Levin, J., McWilliams, J., Miller, A., Moore, A., Powell, T., Shchepetkin, A., Sherwood, C., Signell, R., Warner, J., Wilkin, J. 2008. Ocean forecasting in terrain-following cordinates: Formulation and skill assessment of the Regional Ocean Modeling System. Journal of Computational Physics, vol.227, pp/3595-3624.

Haidvogel, D., Arango, H., Hedström, K., Beckmann, A., Malanotte-Rizzoli, P., Shchepetkin, A., 2000. Model evaluation experiments in the North Atlantic Basin: Simulations in nonlinear terrain-following coordinates, Dynamics of Atmospheres and Oceans, 32, 239–281.

Haidvogel, D., Beckman, A., Hedstrom, K., 1991. Dynamical simulations of filament formation and evolution in the coastal transition zone. Journal of Geophysical Research, 96,15017–15040.

Hamon, B., Godfrey, J., Greig, M., 1975. Relation between mean sea level, current and wind stress on the east coast of Australia. Marine and Freshwater Research, 26(3), 389-403.

Haney, R., 1991, On the pressure gradient force over steep topography in sigma coordinate ocean model. Journal of Physical Oceanography, 21(4), 610-619.

Huyer, A., 1990. Shelf Circulation. The Sea, 9A, 423–466, ed. by B. Le Méhauté and D. M. Hanes.

Hwang, J., Souissi, S., Tseng, L., Seuront, L., Schmitt, F., Fang, L., 2006. A 5-year study of the influence of the northeast and southwest monsoons on copepod assemblages in the boundary coastal waters between the East China Sea and the Taiwan Strait. Journal of Plankton Research, 28, 943-958.

Johnson, J., Chapman, P., 2011. Deep ocean exchange with the shelf (DOES). Ocean Science, 7, 101–109.

Kang, D., Curchitser, E., 2015. Energetics of eddy–mean flow interactions in the Gulf Stream region. Journal of Physical Oceanography, 45, 1103–1120.

Kantha, L., Clayson, C., 2000. Numerical Models of Oceans and Oceanic Processes, International Journal of Geophysics, 66, (750).

Kantha, L., Clayson, C., 2000. Numerical Models of Oceans and Oceanic Processes, International Journal of Geophysics, 66, 750.

Kerry, C., Powell, B., Roughan, M., Oke, P., 2016. Development and evaluation of a high-resolution reanalysis of the East Australian Current region using the Regional Ocean Modelling System (ROMS3.4) and Incremental Strong Constraint 4 Dimensional Variational data assimilation (IS4D-Var). Geoscientific Model Development, 10, 5194.

Large, W., Crawford, G., 1995. Observations and simulations of upper ocean response to wind events during the Ocean Storms Experiment. Journal of Physical Oceanography, 25, 2831–2852.

Lee, S., Birch, G., Lemckert, C., 2011. Field and modelling investigations of fresh-water plume behavior in response to infrequent high-precipitation events, Sydney Estuary, Australia. Estuarine, Coastal and Shelf Science, 92(3), 389-402.

Lentz, S., 2001. The influence of stratification on the wind-driven cross-shelf circulation over the North Carolina Shelf. Journal of Physical Oceanography, 31, 2749–2760.

Lentz, S., 2008. Seasonal variations in the circulation over the Middle Atlantic Bight continental shelf. Journal of Physical Oceanography, 38 (7), 1486-1500.

Lerczak, J., Hendershott, M., Winant, C., 2001. Observations and modeling of coastal internal waves driven by a diurnal sea breeze. Journal of Geophysical Research, 106, 19, 715–19, 729.

Lilly, J., Olheded, S., 2010. On the analytic wavelet transform. IEEE Transactions on Information Theory, 56 (8), 4135-4156.

Liu, Y., Liang., X, Weisberg, R., 2007. Rectification of the bias in the wavelet power spectrum. Journal of Atmospheric and Oceanic Technology, 24(12), 2093-2102.

Lorenz, E., 1956. Empirical orthogonal functions and statistical weather prediction. Scientific Report No. 1, Air Force Cambridge Research Center, Air Research and Development Command. Cambridge Mass.

Macdonald, H., Roughan, M., Baird, M., Wilkin, J., 2013. A numerical modelling study of the East Australian Current encircling and overwashing a warm-core eddy. Journal of Geophysical Research: Oceans 118, 301-315.

Macreadie, P., Fowler, A., Booth, D., 2011. Rigs-to-reefs: will the deep-sea benefit from artificial habitat? Frontiers in Ecology and the Environment, 9, 455–461.

Marchesiello, P., McWilliams, J., Shchepetkin, A., 2001. Open boundary conditions for long-term integration of regional oceanic models. Ocean Modelling, 3 (1-2), 1-20.

Marchesiello, P., Middleton, J., 2000. Modeling the East Australian Current in the western Tasman Sea. Journal of Physical Oceanography, 30, 2956–2971.

Marta-Almeida, M., Hetland, R., Zhang, X., 2013. Evaluation of model nesting performance on the Texas-Lousiana continental shelf. Journal of Geophysical Research, 118.

Mason, E., Molemaker, M., Shchepetkin, A., Colas, F., McWilliams, J., Sangrà, P., 2010. Procedures for offline grid nesting in regional ocean models. Ocean Modelling, 35 (1-2), 1–15.

Mata, M, Tomczak, M., Wijels, S., Church, J., 2000. East Australian Current volume transports at 30S: Estimates from the World Ocean Circulation Experiment hydrographic sections PR11/P6 and the PCM3 current meter array. Journal of Geophysical Research, 105 (C12), 28509-28526.

Mata, M., Wijffels, Church, J., Tomczak, M., 2006. Eddy shedding and energy conversions in the East Australian Current. Journal of Geophysical Research 111, C09034.

Mellor, G., Ezer, T., Oey, L., 1994. The pressure gradient conundrum of sigma coordinate ocean models. Journal of Atmospheric and Oceanic Technology, 11(4), 1126-1134.

Mellor, G., Wang, X., 1996. Pressure compensation and the bottom boundary Layer. Journal of Physical Oceanography, 26(10), 2214-2222.

Mellor, G., Yamada, T., 1982. Development of a turbulence closure model for geophysical fluid problems. Reviews of geophysics and space physics 20 (4), 851–875.

Mitarai S, Siegel, D., Winters, K., 2008. A numerical study of stochastic larval settlement in the California Current system. Journal of Marine Systems, 69, 295–309.

Mongin M., Matear R., Chamberlain M., 2011. Seasonal and spatial variability of remotely sensed chlorophyll and physical fields in the SAZ-Sense region. Deep Sea Research Part II: Topical Studies in Oceanography, 58, 2082-2093.

Moore, M.,Wilkin, J., 1998. Variability in the South Pacific Deep Western Boundary Current from current meter observations and a high-resolution global model. Journal of Geophysical Research, 103, 5439– 5457.

Motro, R., Ayalon, I., Genin, A., 2005. Near-bottom depletion of zooplankton over coral reefs: III: vertical gradient of predation pressure. Coral Reefs, 24, 95.

Oke, P., Allen, J., Miller, R., Egbert, G., Kosro, P., 2002. Assimilation of surface velocity data into a primitive equation coastal ocean model. Journal of Geophysical Research,107, 3122.

Oke, P., Brassington, G., Griffin, D., Schiller, A., 2009. Data assimilation in the Australian Bluelink system. Mercator Newsletter, 34, 35-44.

Oke, P., Griffin, D., 2011. The cold-core eddy and strong upwelling off the coast of New South Wales in early 2007. Deep-Sea Research Part II: Topical Studies in Oceanography, 58,574-591.

Oke, P., Middleton, J., 2000. Topographically induced upwelling off eastern Australia. Journal of Physical Oceanography, 30 (3), 512-531.

Oke, P., Middleton, J., 2001.Nutrient Enrichment off Port Stephens: The Role of the East Australian Current. Continental Shelf Research, 21, 587–606.

Okubo, A., 1971. Oceanic diffusion diagrams. Deep Sea Research and Oceanographic Abstracts, 18(8), 789-802.

Oliveira, L., Piola, A., Mata, M., Soares, I., 2009. Brazil Current surface circulation and energetics observed from drifting buoys. Journal of Geophysical Research, 114, C10006.

Olson, D., 1991. Rings in the ocean, Annual Review of Earth and Planetary Sciences, 19, 283–311.

Orvik, K., Niiler, P., 2002. Major pathways of Atlantic water in the northern North Atlantic and Nordic Seas toward Arctic. Geophysical Research Letters, 29,

1896.

Otero, P., Ruiz-Villarreal, M., 2008. Wind forcing of the coastal circulation off north and northwest Iberia: comparison of atmospheric models. Journal of Geophysical Research: Oceans, 113 (C10).

Paris, C., Helgers J., van Sebille, E., Srinivasan A., 2013. Connectivity Modeling System: A probabilistic modeling tool for the multi-scale tracking of biotic and abiotic variability in the ocean. Environmental Modelling and Software (Supplement C), 47-54.

Parsons, D., Suthers, I., Cruz, D., Smith, J., 2016. Effects of habitat on fish abundance and species composition on temperate rocky reefs. Marine Ecology Progress Series, 561.

Pawlowicz, R., Beardsley, B., Lentz, S., 2002. Classical tidal harmonic analysis including error estimates in MATLAB using T_TIDE Computers and Geosciences, 28, 929-937.

Penven, P., Debreu, L., Marchesiello, P., McWilliams, J., 2006. Evaluation and application of the ROMS 1-way embedding procedure to the central California upwelling system. Ocean Modelling, 12 (1-2), 157-187.

Puri, K., Dietachmayer, G., Steinle, P., Dix, M., Rikus, L., Logan, L., Naughton, M., Tingwell, C., Xiao, Y., Barras, V., Bermous, I., Bowen, R., Deschamps, L., Franklin, C., Fraser, J., Glowacki, T., Harris, B., Lee, J., Le, T., Roff, G., Sulaiman, A., Sims, H., Sun, X., Sun, Z., Zhu, H., Chattopadhyay, M., and Engel, C., 2013. Operational implementation of the ACCESS Numerical Weather Prediction system, Australian Meteorological and Oceanographic Journal, 63, 265-284.

Ridgway, K., Dunn, J., 2003. Mesoscale structure of the mean East Australian Current System and its relationship with topography. Progress in Oceanography, 56,189 - 222.

Ridgway, K., Godfrey, J., 1997. Seasonal cycle of the East Australian Current. Journal of Geophysical Research: Oceans 102 (C10), 22921-22936.

Robinson, A., Brink, K., 2005. The Global Coastal Ocean: Multiscale Interdisciplinary Processes, The Sea, 13.

Rosenfeld, L., 1983. CODE-1: Moored Array and Large-scale Data Report, Technical Report, 83-23, Woods Hole Oceanographic Institution, Woods Hole, MA.

Rossi, V., Schaeffer, A., Wood, J., Galibert, G., Morris, B., Sudre, J., Roughan, M., Waite, A. M., 2014. Seasonality of sporadic physical processes driving temperature and nutrient high-frequency variability in the coastal ocean off southeast Australia. Journal of Geophysical Research: Oceans 119, 445–460.

Roughan, M., MacDonald, H., Baird, M., Glasby, T., 2011. Modelling coastal connectivity in a western boundary current: seasonal and inter-annual variability. Deep Sea Research Part II: Topical Studies in Oceanography, 58 (5), 628-644.

Roughan, M., Middleton, J., 2002. A comparison of observed upwelling mechanisms off the east coast of Australia. Continental Shelf Research 22 (17), 2551–2572.

Roughan, M., Middleton, J., 2004. On the East Australian Current: Variability, encroachment, and upwelling. Journal of Geophysical Research: Oceans 109, 1–16.

Roughan, M., Morris, B., 2011. Using high-resolution ocean timeseries data to give context to long term hydrographic sampling off Port Hacking, NSW, Australia,

OCEANS'11-MTS/IEEE.IEEE, Piscataway, NJ, United States., Kona, Hawaii, 1–4.

Roughan, M., Morris, B., Suthers, I., 2010, NSW-IMOS: An Integrated Marine Observing System for Southeastern Australia. IOP Conference Series: Earth and Environmental Science 11, 1-6.

Roughan, M., Oke, P., Middleton, J., 2003. A modeling study of the climatological current field and the trajectories of upwelled particles in the East Australian Current. Journal of Physical Oceanography, 33(12), 2551-2564.

Roughan, M., Schaeffer, A., Suthers, I., 2015. Sustained Ocean observing along the coast of southeastern Australia: NSW-IMOS 2007-2014, Coastal Ocean Observing Systems. Elsevier (Academic Press), San Diego CA, 76–98.

Roughgarden, J., Gaines, S., Possingham, H., 1988. Recruitment dynamics in complex life-cycles, Science, 241 (4872), 1460–1466.

Sasaki, H., Nonaka, M., Masumoto, Y., Sasai, Y., Uehara, H., Sakuma, H., 2008. An eddy-resolving hindcast simulation of the quasiglobal ocean from 1950 to 2003 on the Earth Simulator. In: Hamilton K, Ohfuchi W (eds) High-resolution numerical modeling of the atmosphere and ocean, 157-185.

Schaeffer, A., Garreau, P., Molcard, A., Fraunié, P., Seity, Y., 2011. Influence of high-resolution wind forcing on hydrodynamic modeling of the Gulf of Lions. Ocean Dynamics, 61, 1823-1844.

Schaeffer, A., Roughan, M., 2015. Influence of a western boundary current on shelf dynamics and upwelling from repeat glider deployments. Geophysical Research Letters, 42 (1), 121-128.

Schaeffer, A., Roughan, M., Jones, M., White, D., 2016. Physical and biogeochemical spatial scales of variability in the East Australian Current separation from shelf glider measurements. Biogeosciences, 13, 1967-1975.

Schaeffer, A., Roughan, M., Morris, B., 2013. Cross-Shelf Dynamics in a Western Boundary Current Regime: Implications for upwelling. Journal for Physical Oceanography, 43, 1042-1059.

Schaeffer, A., Roughan, M., Morris, B., 2014a. CORRIGENDUM. Journal for Physical Oceanography, 44, 2812-2813.

Schaeffer, A., Roughan, M., Wood, J., 2014b. Observed bottom boundary layer transport and uplift on the continental shelf adjacent to a western boundary current, Journal of Geophysical Research: Oceans 119, 4922–4939.

Scott., M, Smith, J., Lowry, M., Taylor, M., Suthers, I., 2015. The influence of an offshore artificial reef on the abundance of fish in the surrounding pelagic environment. Marine and Freshwater Research, 66, 429-437.

Seaman, W., Jensen, A., 2000. Purposes and Practices of Artificial reef Evaluation. In Artificial reef evaluation: with application to natural marine habitats CRC Press, LLC, Boca Raton, Florida, USA, 1-19.

Shchepetkin, A., McWilliams, J., 2003. A method for computing horizontal pressure-gradient force in an oceanic model with a non-aligned vertical coordinate. Journal of Geophysical Research: Oceans, 108 (C3), 3090.

Shchepetkin, A., McWilliams, J., 2005. The regional oceanic modeling system (ROMS): a split-explicit, free-surface, topography-following-coordinate oceanic model. Ocean Modelling, 9 (4), 347–404.

Shchepetkin, A., McWilliams, J., 2009. Correction and commentary for ‘‘Ocean forecasting in terrain-following coordinates: formulation and skill assessment of the regional ocean modeling system”, Journal of Computational Physics, 227, 3595-3624. Journal of Computational Physics, 228, 8985–9000.

Sheng, J., Greatbatch, R., Zhai, X., Tang, L., 2005b. A new two-way nesting technique based on the smoothed semi-prognostic method. Ocean Dynamics, 55, 162-177.

Siegel, D., Kinlan, B., Gaylord, B., Gaines, S., 2003. Lagrangian descriptions of marine larval dispersion, Marine Ecology Progress Series, 260, 83– 96.

Sikiric, M., Janekovic, I., Kuzmic, M., 2009. A new approach to bathymetry smoothing in sigma-coordinate ocean models. Ocean Modell., (29) 128–136.

Sloyan, B., Ridgway, K., Cowley, R., 2016. The East Australian Current and Property Transport at 27° S from 2012 to 2013. Journal of Physical Oceanography, 46 (3), 993 - 1008.

Smith, J., Lowry, M., Champion, C., Suthers, I., 2016. A designed artificial reef is among the most productive marine fish habitats: new metrics to address production versus attraction. Marine Biology, 163, 188.

Song, Y., Haidvogel, D., 1994. A semi-implicit ocean circulation model using a generalized topography-following coordinate system, Journal of Computational Physics, 115 (1), 228–244.

Song, Y., Hou, T., 2006. Parametric vertical coordinate formulation for multiscale, Boussinesq, and non-Boussinesq ocean modeling. Ocean Modelling, 11, 298-332.

Souza, J., Powell, B., Castillo-Trujillo, A., Flament, P., 2014. The Vorticity Balance of the Ocean Surface in Hawaii from a Regional Reanalysis, Journal of Physical Oceanography, 45, 424–440.

Suthers, I., Young, J., Baird, M., Roughan, M., Everett, J., Brassington, B., Byrne, M., Condie, S., Hartog, J., Hassler, C., Hobday, A., Holbrook, N., Malcom, H., Oke, P, Thompson, P., Ridgway, K., 2011. The strengthening East Australian

Current, its eddies and biological effects-an introduction and overview. Deep Sea Research Part II: Topical Studies in Oceanography, 58 (5), 538-546.

Talley, L., 2002. Ocean Circulation. The Earth system: physical and chemical dimensions of global environmental change. Encyclopedia of Global Environmental Change, 557-579.

Taylor, K., 2001. Summarizing multiple aspects of model performance in a single diagram. Journal of Geophysical Research, 106, 7183–7192.

Thierry, J., 1988. Artificial reefs in Japan - a general outline. Aquacultural Engineering, 7, 321-348.

Tomczak, M., Godfrey, J., 1994. Regional oceanography: an introduction. Pergamon Press, Oxford, p 422.

Torrence, C., Compo, G., 1998. A practical guide to wavelet analysis. Bulletin of the American Meteorological Society, 79 (1), 61-78.

Tranter, D. J., Carpenter, D. J., Leech, G. S., 1986. The coastal enrichment effect of the East Australian Current eddy field. Deep Sea Research Part A. Oceanographic Research Papers 33 (1112), 1705-1728.

Truong, L., Suthers, I., Cruz, D., 2017. Plankton supports the majority of fish biomass on temperate rocky reefs. Marine Biology, 164, 73.

Tseng, L., Kumar, R., Dahms, H., Chen, Q., Hwang, J., 2008. Monsoon driven seasonal succession of copepod assemblages in the coastal waters of the northeastern Taiwan Strait. Zoological Studies, 47, 46-60.

Vandenbulcke, L., Barth, A., Rixen, M., Alvera-Azcárate, A., Ben Bouallegue, Z., Beckers, J., 2006. Study of the combined effects of data assimilation and grid nesting in ocean models- application to the Gulf of Lions. Ocean Science Discussions, European Geosciences Union, 2006, 3 (3), 291-318.

Weisburd, S., 1986. Artificial reefs. Science News, 30, 59.

Werner, E., Yurewicz, K., Skelly, D., Relyea, R., 2007. Turnover in an amphibian metacommunity: the role of local and regional factors. Oikos, 116, 1713 1725.

Whiteway, T., 2009. Australian Bathymetry and Topography Grid. Scale 1:5000000, Geoscience Australia Record, 21, 46.

White, A., Chou, L., De Silva, M., Guarin, F., 1990. Artificial Reefs for Marine Habitat Enhancement in Southeast Asia. ICLARM Education Series 11. ICLARM: Philippines.

Wilkin, J., Zhang, W., 2007. Modes of mesoscale sea surface height and temperature variability in the East Australian Current. Journal of Geophysical Research, 112, C01013.

Wood, J., Roughan, M., Tate, P, 2012. Finding a proxy for wind stress over the coastal ocean. Marine Freshwater Research 63, 528–544.

Wood, J., Schaeffer, A., Roughan, M., Tate, P., 2016. Seasonal variability in the continental shelf waters off southeastern Australia: Fact or fiction? Continental Shelf Research, 112, 92-103.

Zhan, P., Subramanian, A., Yao, F., Kartadikaria, A., Guo, D., Hoteit, I., 2016. The eddy kinetic energy budget in the Red Sea, Journal of Geophysical Research: Oceans 121, 4732–4747.

Zhang, W., Gawarkiewicz, G., McGillicuddy Jr, D., 2011. Climatological Mean Circulation at the New England Shelf Break. Journal of Physical Oceanography, 41 (10), 1874-1893.

Zhong, L., Hua, L., Luo, D., 2016. The eddy-mean flow interaction and the intrusion of western boundary current into the South China Sea-type basin in an idealized model. Journal of Physical Oceanography, 46, 2493-2527.